AD_____

Award Number: W81XWH-05-1-0280

TITLE: Design, Implementation, and Characterization of a Dedicated Breast Computed Mammotomography System for Enhanced Lesion Imaging

PRINCIPAL INVESTIGATOR: Randolph L. McKinley

CONTRACTING ORGANIZATION: Duke University
Durham, NC 27710

REPORT DATE: March 2006

TYPE OF REPORT: Annual Summary

PREPARED FOR: U.S. Army Medical Research and Materiel Command
Fort Detrick, Maryland 21702-5012

REPORT DOCUMENTATION PAGE

Form Approved
OMB No. 0704-0188

1. REPORT DATE	2. REPORT TYPE	3. DATES COVERED
01-03-2006	Annual Summary	1 Mar 2005 – 28 Feb 2006

4. TITLE AND SUBTITLE

Design, Implementation, and Characterization of a Dedicated Breast Computed Mammotomography System for Enhanced Lesion Imaging

5a. CONTRACT NUMBER

5b. GRANT NUMBER
W81XWH-05-1-0280

5c. PROGRAM ELEMENT NUMBER

6. AUTHOR(S)

Randolph L. McKinley

5d. PROJECT NUMBER

5e. TASK NUMBER

5f. WORK UNIT NUMBER

7. PERFORMING ORGANIZATION NAME(S) AND ADDRESS(ES)

Duke University
Durham, NC 27710

8. PERFORMING ORGANIZATION REPORT NUMBER

9. SPONSORING / MONITORING AGENCY NAME(S) AND ADDRESS(ES)
U.S. Army Medical Research and Materiel Command
Fort Detrick, Maryland 21702-5012

10. SPONSOR/MONITOR'S ACRONYM(S)

11. SPONSOR/MONITOR'S REPORT NUMBER(S)

12. DISTRIBUTION / AVAILABILITY STATEMENT
Approved for Public Release; Distribution Unlimited

13. SUPPLEMENTARY NOTES
Original contains colored plates: ALL DTIC reproductions will be in black and white.

14. ABSTRACT

The overall goal of this work is to design, implement, and characterize a novel dedicated mammotomography system for enhanced lesion detection. This novel system will allow fully 3-D imaging of a pendant, uncompressed breast using novel 3-D complex orbit capabilities. The system has been successfully implemented on a mounting system providing azimuthal and polar tilt capability. System components have been automated to allow synchronized tomographic data acquisitions at the touch of a button. Image corrections have been implemented to maximize image quality and initial phantom measurements are promising. Half cone-beam orbits have been implemented and investigated and have indicated they are feasible for a wide range of breast sizes. Future studies will focus on characterizing the system in terms of dose efficiency, contrast sensitivity, and evaluation for a range of breast sizes and compositions. Patient bed optimization will also be investigated.

15. SUBJECT TERMS
Dedicated Tomographic Breast Imaging, X-Ray Imaging, Computed Tomography

16. SECURITY CLASSIFICATION OF:				18. NUMBER OF PAGES	19a. NAME OF RESPONSIBLE PERSON
					USAMRMC
a. REPORT	b. ABSTRACT	c. THIS PAGE			19b. TELEPHONE NUMBER *(include area code)*
U	U	U	UU	74	

Table of Contents

Introduction

In the USA, breast cancer in women is one of the leading causes of malignancy and the second leading cause of death due to cancer (after lung cancer); in addition, from 2000 – 2004, its incidence rose at about 4% per year.[1] Thus, early detection of a primary cancer is of paramount importance, because treatment of a small tumor allows for more limited surgery with breast conservation and significantly reduces morbidity and mortality. Limitations in mammography have led to the progressive emergence of complementary imaging techniques. The dedicated breast Computed mammoTomography (CmT) solution we are proposing[2-10] has several potential benefits, including: (1) improved detection and characterization of breast lesions, especially in radiographically dense breasts,[2,11-13] through the removal of contrast-reducing overlying tissue; (2) *uncompressed* breast imaging for greater patient comfort with an associated potential increase in participation rates; (3) breast dose equal to or less than that of current dual view mammography with anticipated increased image contrast; and (4) expectedly improved positive predictive value, especially for radiographically dense breasts. The main goal of this work is to design, develop, implement, and characterize a novel, dedicated computed mammotomography system using cone-beam imaging geometry, having novel degrees of freedom of movement with a unique offset geometry, and using iterative reconstruction techniques. It is hoped that this research and development will lead to *in vivo* tissue differentiation resulting in an improvement in the detection and diagnosis of breast cancer.

Body

Task 1 was comprised of 5 parts and was originally scheduled to fill year 1. This key task had the overall goal of implementing the prototype CmT system for unique acquisition capabilities. Specific sub-task details and progress are provided below.

Task 1(a). The first key sub-task was specifically to implement a mounting system for X-ray source and detector for flexible acquisitions involving azimuthal rotation and polar tilt. The initial iteration of our system came in the form of a flexible mounting system designed in-house and made of an industrial erector set (Figure.1). This mounting system was stationary and allowed for flexibility in adjusting source-to-image distance (SID), detector tilt, and X-ray tube tilt. Initial projection data for beam optimization as well as preliminary tomographic acquisitions (again done by rotating the object) were acquired using this prototype. Figure.1 (bottom) illustrates use of system tilt and flexibility on an inverted system for imaging a chest phantom with attached breast phantom. The next step (and current iteration) in design of the system was to provide a fully automated and synchronized tomograph with system rotation and tilt capabilities. Geometric limitations incurred by the system and patient geometry necessitate a flexible mounting system for a dedicated CmT system allowing for unique source/detector positioning and tilting for full volumetric sampling of the breast and anterior chest wall. The digital detector and X-ray tube are currently mounted on a computer controlled goniometer (model BGM200PE,

Newport Corp.) and rotation stage (model RV350, *Newport Corp.*, Irvine, CA) to allow polar and azimuthal movements, respectively (Figure 2).[14-16] The system initially operated with manual timing, movement, and exposure but is now fully automated after having implemented computer controlled synchronization between rotation stage motor, gantry motor, anode rotor, X-ray generator, and detector controller. A full report of the current system is provided in Appendix B. The band within which the gantry can swing is illustrated in Figure.3.

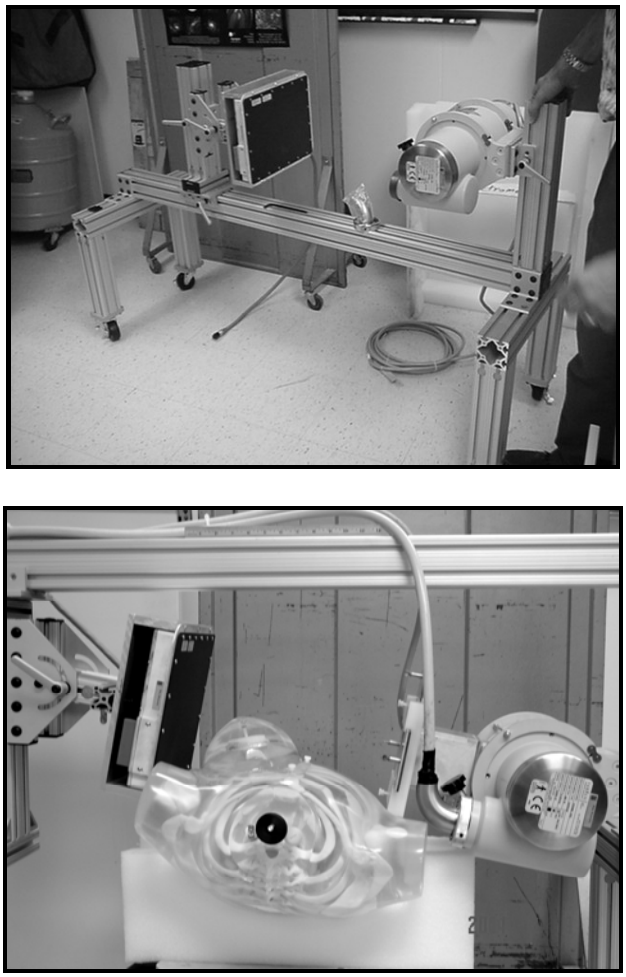

Figure.1 (top) Pre-prototype imaging apparatus with (from L to R) detector and X-ray tube, and (bottom) modified pre-prototype with torso phantom and attached breast phantom illustrating the pre-automation manual methods for acquisition. Note in bottom photo that stationary device has been inverted from the top photo. This was found to allow greater flexibility in object placement and rotation.

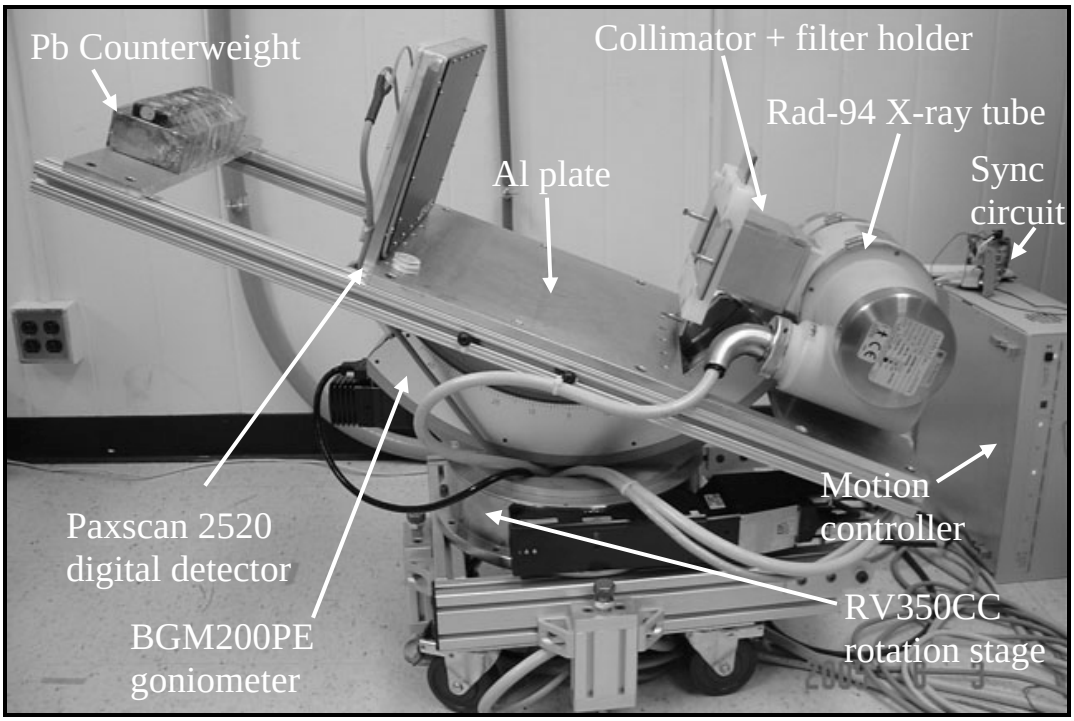

Figure.2 System setup denoting components that have been integrated in a functioning prototype. Components include the BGM200PE goniometer and RV350CC rotation stage, the Varian Rad-94 tungsten X-ray tube and Varian Paxscan 2520 digital X-ray detector, the Al mounting plate, and the synchronization circuit.

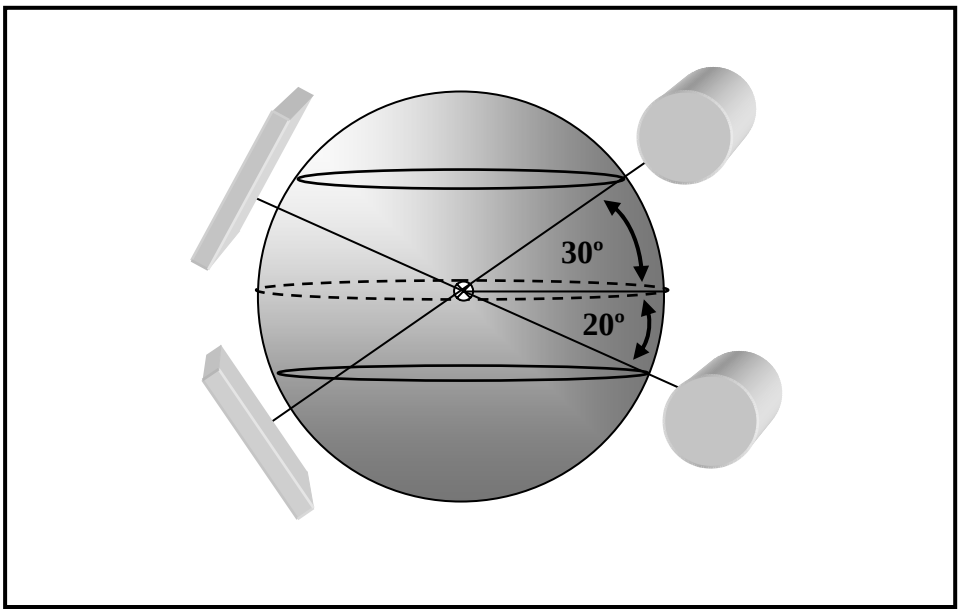

Figure.3 Schematic illustrating band within which arbitrary and complex orbits can be acquired with the gantry. The tube down limit is imposed when the tube cathode and anode plug ports (not seen here) impinge upon the goniometer cradle. The tube up limit is imposed when the top of the detector touches the inside of the goniometer cradle.

Task 1(b). The next sub-task was to automate data acquisition sequence, synchronizing detector readout in software with gantry control and generator exposure initiation. The CmT system currently is fully automated and synchronized using (custom written) C code such that full acquisitions with arbitrary complex orbits can now be obtained with simple command line inputs. Several components used in the design of the automation and synchronization will be described below, as well as general timing sequence of the acquisitions. A flowchart (Figure 4**Error! Reference source not found.**), circuit diagram (Figure 5), and timing diagram (Figure 6) are provided to illustrate the imaging sequence synchronization and control used in our automated system.

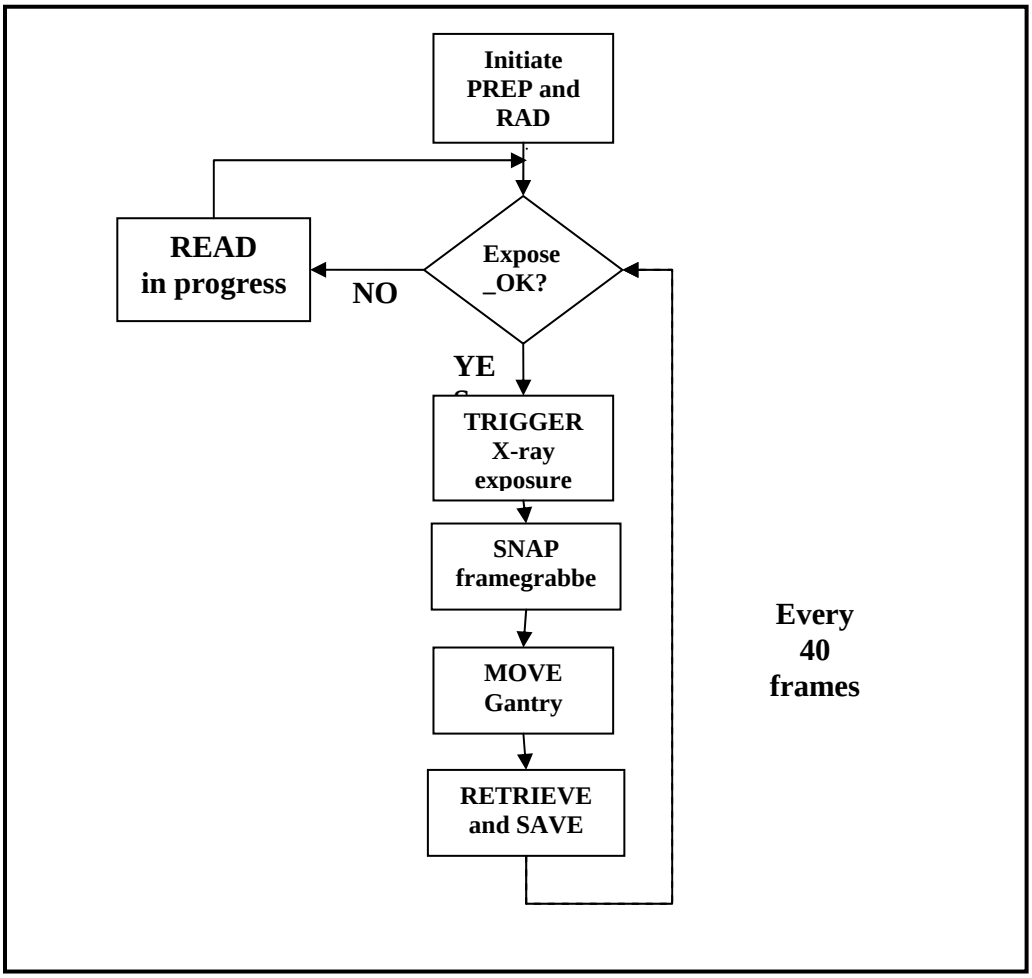

Figure 4 Flowchart illustrating sequence of commands in custom developed C application corresponding to timing diagram shown in Figure 4. Note dashed line indicates requirement to restart PREP and RAD every 40 frames to avoid inadvertant automatic stopping of rotor by the generator.

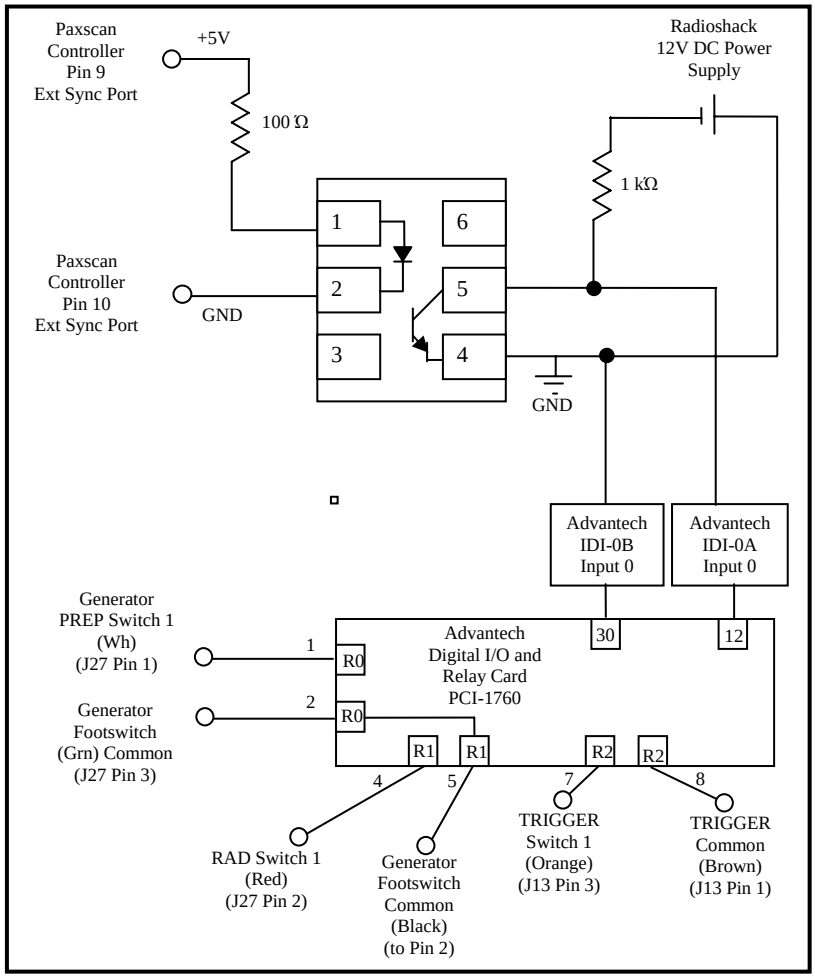

Figure 5 Circuit diagram showing interface between the Paxscan 2520 controller, the Advantech PCI1760 Digital I/O ports, the Advantech relay ports, and the Electromed CPX160 generator PREP, RAD, and TRIGGER interfaces.

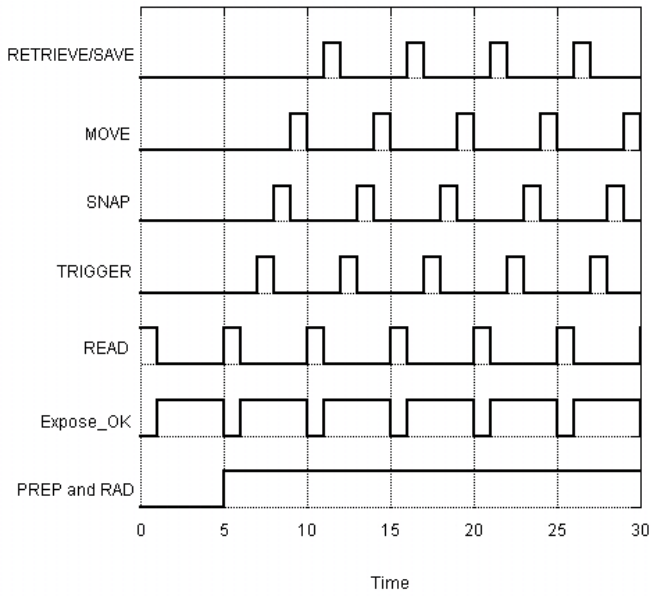

Figure 6 Synchronization diagram illustrating signal coordination between various components in the automated system including (from bottom to top) the tube rotor (PREP and RAD), the detector (Expose_OK), the *Varian* controller (READ), the X-ray generator (TRIGGER), the Epix PIXCI D2X framegrabber (SNAP), the *Newport* motion controller and gantry (MOVE), and the computer hard drive storage (RETRIEVE/SAVE). Note that widths are arbitrarily scaled simply to show the leading edge of the timing sequence and relative order of commands.

Several steps are carried out before each exposure is initiated: (1) a SNAP command is issued to a framegrabber card (model PIXCI D2X, *Epix Inc.*, Buffalo Grove, IL) connected to the video port of the controller (for extremely rapid acquisition of the raw image file from the controller); (2) a MOVE command is issued to the *Newport* motion controller to move the gantry to the next position; (3) after the exposed frame is READ out by the detector controller, a RETRIEVE and SAVE command is issued to write the image directly to the computer hard drive.

Task 1(c). The next sub-task was to perform initial phantom measurements using 3D geometric frequency/resolution phantoms to optimize cone-beam reconstruction, utilizing ordered subsets based iterative transmission reconstruction techniques for 3D cone-beam acquisition. We have investigated cone-beam acquisitions implemented on the CmT system with unique arbitrary orbit capability for pendant, uncompressed breast imaging. We determined the necessity of complex orbits for improved sampling (as compared to simple circular acquisitions) to satisfy Tuy's data sufficiency condition, thereby reducing distortion in the outer planes. Although an infinite number of orbits are possible with our system, we evaluate the usefulness of two specific orbits, made possible by utilizing the polar tilt capability of our system, for their ability to reduce cone-beam distortion and

sample closer to the chest wall. Full details of this study are provided in Appendix C. Results indicate that our complex orbit capability can be used successfully to image closer to the chest wall and to eliminate cone-beam distortion artifacts.

Task 1(d). The next sub-task involved using simple acquisition geometries to optimize image gain, offset, and line correction algorithms to maximize projection image quality and noise reduction. Experience during testing of the synchronization sequence has shown that image lag is readily apparent visually during a tomographic acquisition, observed while using the built-in detector normalization routines provided by *Varian* for gain, offset, and defective pixel correction. Gain correction is used to correct for differences between pixels in their gain when exposed to a uniform flat field. Offset correction is used to correct for dark current, which is the flow of electrons and holes in a semiconductor p-n junction even in the presence of an applied reverse bias voltage.

One way in which image lag can be reduced is through "frame flushing". That is, several dark frames are read in between X-ray exposures in order to remove residual signal from the detector pixels. The built-in gain correction algorithm provided by *Varian* does not allow specification of frame flushing during the collection of the gain correction images. The gain images are collected at every frame and, therefore, no frames can be skipped. Therefore, when implementing a tomographic acquisition using frame flushing, the built-in gain corrections will be incorrect and poorly gain-corrected images will result. Due to this inherent limitation, it became necessary to implement our own gain correction.

The following experiment was carried out to test the effectiveness of our frame flushing acquisition sequence (along with the required custom gain corrections) in reducing image lag. A sequence of 240 flat field images were acquired at 1 frame readout and one X-ray exposure per second using automated *Varian* correction schemes. Another sequence was acquired using a 5 fps readout rate but still with only one X-ray exposure per second. This allowed for 4 frames of flushing of residual signal between each exposure. Results show (Figure 7) an approximately 29% increase in mean pixel value during a 240 frame flat field acquisition for an automated correction scheme versus the flushing scheme. In addition, an initial steep rise in pixel value over the first few exposures is observed. This can be somewhat alleviated by using a pre-exposure scheme together with the automated acquisition.

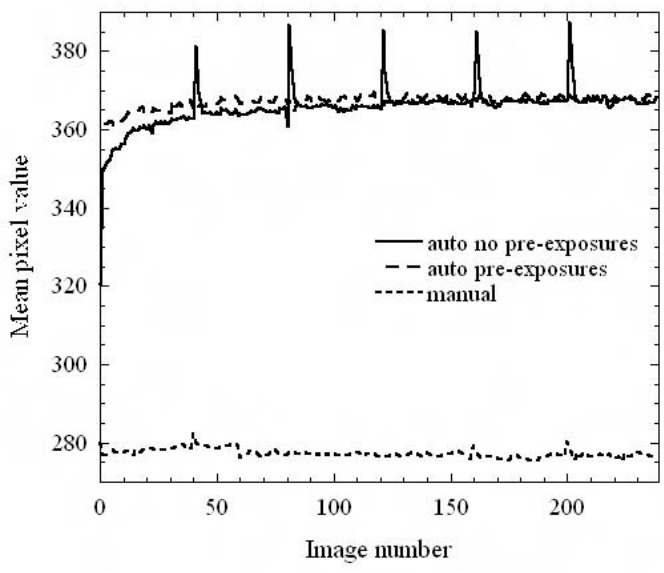

Figure 7 Mean pixel value for 240 projection flat field acquisition at 1 fps using (1) auto calibrations with no pre-exposures, (2) auto calibrations with pre-exposures, and (3) manually implemented calibrations. Note the spikes in the "auto no pre-exposure" curve. These are a result of the fact that the tube rotor has to be stopped and restarted every 40 frames (see text for explanation) because of inherent automatic rotor shutdowns. We are working with the manufacturer to solve this issue.

In order to use our custom developed gain correction routines, it is necessary to turn off the flag to the *Varian* controller that tells it to perform automatic gain correction (we have to have the raw uncorrected data). Another limitation of the *Varian* built-in corrections is that defective pixel correction is only provided while the gain correction flag is on (this is because the gain correction files are used to determine defects). Therefore, it became necessary to implement our own defective pixel correction as well. While the *Varian* controller carries out defective pixel correction by averaging the two nearest neighbors in a row, we have implemented a routine that averages four pixels: two nearest neighbors in a row and two nearest neighbors in a column.

While severe effects of lag have been observed in projection images, especially when non-uniform or degraded external filters are used, it remains to be seen whether these will result in observable effects in the reconstructed image. Nevertheless, at this point, it makes sense to use the frame flushing sequence together with custom corrections in order to get the best possible input projection images for the reconstruction routine.

Task 1(e). The next sub-task was to design and evaluate offset half cone-beam using 360 degree acquisition as well as horizontal versus vertical positioning of detector for maximizing range of uncompressed breasts accommodated. The requirement of our compact system design indicates potential limitations in imaging uncompressed breasts with diameters larger than ~15 cm.[8,14] In this study, we performed CmT acquisitions using relatively small (240mL volume) and large (935mL volume) breast phantoms to evaluate the requirement for an offset or half-cone beam geometry. This geometry could allow the cone beam to be offset such that it images just over half the pendant breast at each projection, with conjugate projections acquired through a full 360 degree rotation of

the gantry (Figure 8). The specific objectives of this study are to: (1) overcome the maximum uncompressed breast size limitation by implementing an offset central ray design for the cone beam geometry; (2) determine the impact on the elimination of truncation artifacts for very large breasts which are only partially in the field of view of a centered geometry; (3) determine the impact on the accuracy of reconstructed attenuation coefficients; and (4) measure the impact on beam hardening for different breast sizes while utilizing a nearly optimized quasi-monochromatic beam. The paper resulting from this investigation is given in Appendix D. Results indicate that this method can be successfully used with the current apparatus to image a much wider range of breast sizes, and therefore a much larger range of women.

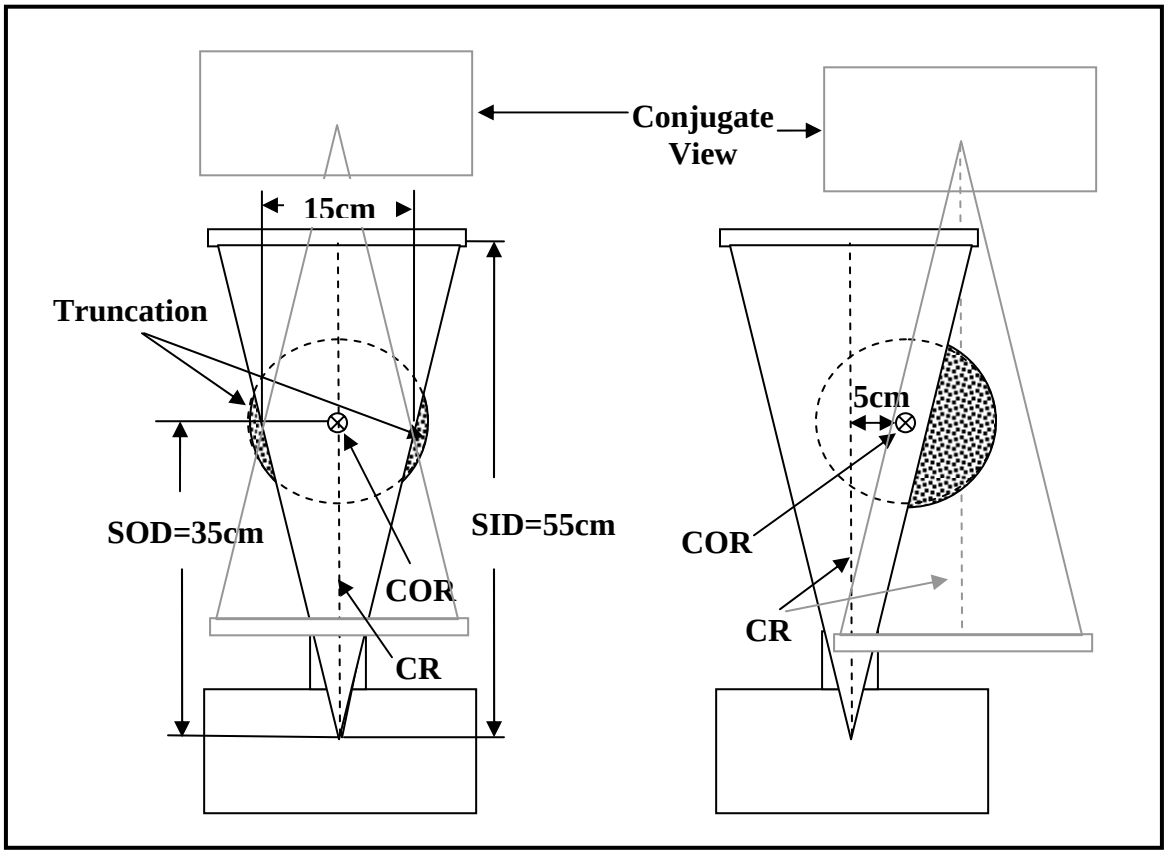

Figure 8 Schematic illustrating (left) centered geometry with central ray (CR) of the cone-beam intersecting the gantry center of rotation (COR), and (right) offset geometry with the CR offset 5cm from the COR to increase breast size range.

In addition to completing Task 1 entirely, we also completed Task 3(c) because the dose coefficients were necessary for completion of planned important studies. Details of this sub-task are provided below.

Task 3(c). This sub-task was to determine normalized glandular dose coefficients for CmT acquisitions for dose determination in preparation for clinical trials. An accurate

comparison between various techniques should only be considered for a fixed dose to the patient. Implementing test situations with different X–ray techniques, where each technique provides exactly the same dose to the patient is difficult. A more feasible way of carrying out such evaluations is to take advantage of the relationship between dose and SNR. In can generally be assumed, in quantum limited detection systems, that a doubling of the dose results in a $\sqrt{2}$ increase in SNR. Therefore, one can define a dose efficiency figure of merit as:

$$DoseEfficiency = SNR^2 / dose$$

which can be considered to be a flux independent measure. In other words, using the dose efficiency figure, it no longer becomes necessary to fix each technique at the same dose to the patient. Recently, we have obtained Monte Carlo based tables of dose coefficients for our specific geometry which can now be used to more accurately calculate dose to the uncompressed breast and allow us to use dose efficiency rather than a surrogate, such as exposure efficiency which we have used in the past. These Monte Carlo based dose conversion tables (denoted D_gN_{CT} coefficients, where D represents dose, sub-g represents glandular, and N represents normalized CT coefficients[15]) for our specific CmT geometry were obtained from Dr. John Boone (UC Davis). Tables were provided for 50/50 adipose/glandular breast composition for breast sizes ranging from 10cm to 18cm (in 1cm increments). The dose coefficients are provided in units of $\mu Gy/10^6$ photons/mm^2 and in 1 keV increments. They are therefore "normalized" to a fixed number of photons. They can then be easily used together with arbitrary spectral data (in units of photons/mm^2/keV) to calculate glandular dose. These are "glandular" coefficients in the sense that the model takes into account only the dose deposited to the glandular tissue. This is based on the assertion that dose to glandular tissue is the most important consideration in assessing ionizing radiation risk to the patient. The Monte Carlo model also accounts for spectral absorption by an incident 5mm thick skin layer. For future studies, these coefficients will be used to determine, relatively easily, an estimate of the glandular dose to an uncompressed 50/50 adipose/glandular composition breast, using our current CmT geometry for breasts ranging in size from 10cm to 18cm in diameter. When considering either breast sizes outside of this range, or breast compositions other than 50/50 adipose/glandular, we will continue to use alternative metrics. Dose minimization studies have been carried out facilitated by the above work. The full details of the study are provided in Appendix E. Results indicate we may be able to utilize the unique capabilities of our system to do 3D breast imaging at dose levels on the order of ½ and as low as 1/10 that of dual view mammography. Currently, the only limitation for testing at lower limits is the relatively hih lower limit of our X-ray tube's power supply.

Key Research Accomplishments

Summary:
Year 1 originally included Task 1 (a through e) from the Statement of Work (SOW) (included as Appendix A). Task 1 was completed in its entirety, including implementation and automation of the system to allow for complex orbit capability at the touch of a button. Software interfaces have been written in Microsoft C to interface to the several mechanical components of the system as well as to carry out synchronization of the acquisition. Phantom studies have been carried out as planned. Task 3(c) was moved to Year 1 from Year 3 because the information was required for subsequent studies. The remaining portions of Task 3 will be moved to Year 2 and Task 2 to Year 3. This is felt to be necessary for the following reason. Most of Task 2 relates to custom bed design. However, it is felt that the bed design will depend somewhat on the results of Task 3. Therefore, Task 3 will be performed first.

Accomplishments:

1. We have successfully implemented the world's first dedicated tomographic breast imaging device that is capable of 3-dimensionally complex orbits.
2. The complex orbit capability allows this device to be the only current cone-beam breast imaging device capable of satisfying Tuy's data sufficiency condition, thereby eliminating cone-beam distortion artifacts.
3. This complex orbit capability will also allow us to image closer to the chest wall than other, fixed rotation devices.
4. Initial dose studies indicate that we may do full breast scans at $1/10^{th}$ the dose (0.6mGy) of dual view mammography. As far as we are aware, this is the only such device with this capability.

Reportable Outcomes

Peer-reviewed:

RL McKinley, MP Tornai, E Samei, ML Bradshaw, "Initial study of quasi-monochromatic beam performance for X-ray computed mammotomography," *IEEE Trans. Nucl. Sci.* **52**(5): 1243-1250, 2005.

RL McKinley, MP Tornai, CN Brzymialkiewicz, E Samei, JE Bowsher, "Analysis of a novel offset cone-beam computed mammotomography imaging system for attenuation correction of SPECT in a proposed dual modality dedicated breast mammotomography system", *Physica Medica* (Volume XXI, Supplement 1, In Press), 2005.

Conference Proceedings:

RL McKinley, CN Brzymialkiewicz, P Madhav, MP Tornai, "Investigation of cone-beam acquisitions implemented using a novel dedicated mammotomography system with

unique arbitrary orbit capability," *Proc. SPIE: Physics of Medical Imaging.* **5745**(6): 609-617, 2005.

MP Tornai, **RL McKinley**, CN Brzymialkiewicz, P Madhav, S Cutler, D Crotty, JE Bowsher, E Samei, CE Floyd, "Design and development of a fully-3D dedicated X-ray computed mammotomography (CmT) system," *Proc. SPIE: Physics of Medical Imaging.* **5745**(6): 189-197, 2005.

MP Tornai, **RL McKinley**, S Cutler, D Crotty, CN Brzymialkiewicz, "Anthropomorphic breast phantoms for preclinical imaging evaluation with emission or transmission imaging," *Proc. SPIE: Physiology, Function, and Structure from Medical Images.* **5746** (6): 825-834, 2005.

MP Tornai, Y-C Tai, **RL McKinley**, M Janecek, H Wu. "Initial design considerations of a dedicated hybrid mammotomograph for fully 3D X-ray CT and high resolution PET using object magnification." Presented at the *52nd Society of Nuclear Medicine Meeting*, Toronto, Canada, 18-22 June, 2005, and published in *J. Nucl. Med.* **46**(5). 2005.

CN Brzymialkiewicz, **RL McKinley**, MP Tornai. "Towards patient imaging with dedicated emission mammotomography." Presented at the *2005 Nucl. Sci. Symp. & Med. Imag. Conf.*, San Juan, Puerto Rico, 23-29 Oct. 2005, and published in *IEEE Conference Record NSS/MIC*: 1519-1523, 2005.

DJ Crotty, CN Brzymialkiewicz, **RL McKinley**, MP Tornai. "Optimizing Orientation of SPECT and Cone Beam CT Detectors Through Quantification of Cross Contamination in a Dual Modality Mammotomography System." Presented at the *2005 Nucl. Sci. Symp. & Med. Imag. Conf.*, San Juan, Puerto Rico, 23-29 Oct. 2005, and published in *IEEE Conference Record NSS/MIC*: 1672-1676, 2005.

DJ Crotty, **RL McKinley**, MP Tornai, "Experimental Spectral Measurements of Heavy K-edge Filtered Beams for X-ray Computed Mammotomography," Presented at *SPIE 2006 Medical Imaging Conference*, San Diego, CA, 12-16 Feb. 2006, and submitted to *Proc. SPIE: Physics of Medical Imaging.*

DJ Crotty, CN Brzymialkiewicz, **RL McKinley**, MP Tornai, "Emission Contamination of the Transmission Image in a Dual Modality Computed Mammotomography System**,"** Presented at *SPIE 2006 Medical Imaging Conference*, San Diego, CA, 12-16 Feb. 2006, and submitted to *Proc. SPIE: Physics of Medical Imaging.*

P Madhav, **RL McKinley**, E Samei, JE Bowsher, MP Tornai, "A Novel Method to Characterize the MTF in 3D for Computed Mammotomography," Presented at *SPIE 2006 Medical Imaging Conference*, San Diego, CA, 12-16 Feb. 2006, and submitted to *Proc. SPIE: Physics of Medical Imaging.*

RL McKinley, MP Tornai, "Investigation of minimum dose requirements for a dedicated mammotomography system with unique arbitrary orbit capability and quasi-monochromatic beam," Presented at *SPIE 2006 Medical Imaging Conference*, San Diego, CA, 12-16 Feb. 2006, and submitted to *Proc. SPIE: Physics of Medical Imaging.*

Book Chapters:

RL McKinley, MP Tornai, "X-ray Equipment Design", Encyclopedia of Medical Devices and Instrumentation, *John Wiley & Sons, Inc.* Hoboken, NJ, (In Press) 2006.

Awards:

2005 *SPIE Medical Imaging Symposium* Poster Award Honorable Mention

Conclusions

Initial studies indicate that the computed mammotomography system we developed can perform fully synchronized and automated complex orbits that may allow enhanced 3D visualization of breast lesions. The system has been used to perform complex scans of phantoms, and the image results are promising. This system will likely be implemented as a diagnostic tool for women having suspicious mammograms, and in the far future may ultimately replace current standard mammography. Future work will include evaluation of performance for different breast sizes, compositions, lesion sizes based on several figures of merit. Bed design to maximize chest wall and axillary imaging will also need to be performed.

References

[1] American Cancer Society, "Cancer Facts and Figures," *www.cancer.org*, 4 (2005).
[2] M.L. Bradshaw, R.L. McKinley, E. Samei et al., "Initial x-ray design considerations for application specific emission and transmission tomography (ASETT) of the breast," *J. Nucl. Med.* **44** (**5**), 287P (2003).
[3] R.L. McKinley, M.P. Tornai, C.N. Brzymialkiewicz et al., "Analysis of a novel offset cone-beam computed mammotomography imaging system for attenuation correction of SPECT in a proposed dual modality dedicated breast mammotomography system," *Presented at the 2004 Workshop on the Nuclear Radiology of the Breast, Rome, Italy and submitted to Physics Medica* **(In Press)** (2004).
[4] R.L. McKinley, M.P. Tornai, E. Samei et al., "Development of an optimal x-ray beam for dual-mode emission and transmission mammotomography," *Nucl. Instr. Meth. Phys. Res. A* **527**, 102-109 (2003).
[5] R.L. McKinley, M.P. Tornai, E. Samei et al., "Initial study of quasi-monochromatic beam performance for x-ray computed mammotomography," *IEEE MIC* **4**, 2999-3003 (2003).
[6] R.L. McKinley, M.P. Tornai, E. Samei et al., "Initial study of quasi-monochromatic beam performance for x-ray computed mammotomography," *IEEE Trans. Nucl. Sci.* **(In Press)** (2005).
[7] M.P. Tornai, J.E. Bowsher, C.N. Archer et al., "Feasibility of Application Specific Emission and Transmission Tomography (ASETT) of the breast," *J. Nucl. Med.* **43** (5), 12 (2002).
[8] M.P. Tornai, J.E. Bowsher, C.N. Archer et al., "A Compact Dedicated Device for Dual Modality Radionuclide Imaging of the Breast with an Application Specific Emission and Transmission Tomograph (ASETT)," *Radiology* **221P**, 555 (2001).
[9] M.P. Tornai, C.N. Brzymialkiewicz, R.L. McKinley et al., "Development of Dedicated 3D Molecular Mammotomography with SPECT and Quasi-Monochromatic X-ray Computed Mammotomography," presented at the *Workshop on Alternatives to Mammography*, Winnepeg, Manitoba, 2004 (unpublished).
[10] M.P. Tornai, Y.C. Tai, and R.L. McKinley, "Initial design considerations of a dedicated hybrid mammotomograph for fully 3D x-ray CT and high resolution PET using object magnification," presented at the *Society of Nuclear Medicine Annual Meeting*, Toronto, ON, 2005 (unpublished).
[11] R.L. McKinley, E. Samei, C.N. Brzymialkiewicz et al., "Measurements of an Optimized Beam for X-ray Computed Mammotomography," *Proc. SPIE: Phys. of Med. Imag.* **5368**, 311-319 (2004).
[12] R.L. McKinley, M.P. Tornai, E. Samei et al., "Simulation Study of a Quasi-Monochromatic Beam for x-ray Computed Mammotomography," *Med. Phys.* **31** (4), 800-813 (2004).
[13] R.L. McKinley, M.P. Tornai, E. Samei et al., "Optimizing Beam Quality for x-ray Computed Mammotomography (CmT)," *Proc. SPIE* **5030**, 575-584 (2003).
[14] M.P. Tornai, C.N. Archer, J.E. Bowsher et al., "Transmission imaging with a compact gamma camera: initial results for mammotomography," *IEEE Nucl. Sci. Symp. and Med. Imag. Conf. Rec.* **3**, 1597-1601 (2002).

[15] NCRP Report, "Quality of Mammography Committee Recommendation," **SC-72** (2002).
[16] J.M. Boone, N. Shah, and T.R. Nelson, "A comprehensive analysis of DgNCT coefficients for pendant-geometry cone-beam breast computed tomography," *Med. Phys.* **31** (2), 226-235 (2002).
[17] J.M. Boone and J.A. Seibert, "A comparison of mono- and poly-energetic x-ray beam performance for radiographic and fluoroscopic imaging," *Med. Phys.* **21**, 1853-1863 (1994).
[18] J.T. Dobbins, E. Samei, H.G. Chotas et al., "Chest Radiography: Optimization of x-ray spectrum for cesium iodide-amorphous silicon flat-panel detector," *Radiology* **226** (1), 221-230 (2002).
[19] J.M. Boone, T.R. Nelson, K.K. Lindfors et al., "Dedicated Breast CT: Radiation Dose and Image Quality Evaluation," *Radiology* **221**, 657-667 (2001).
[20] B. Chen and R. Ning, "Cone-beam volume CT mammographic imaging: feasibility study," *Med. Phys.* **29**, 755-770 (2002).
[21] A.A. Vedula and S.J. Glick, "Computer simulations of CT mammography using a flat panel imager," *Proc. SPIE* **5030**, 349-360 (2003).
[22] M.P. Tornai, J.E. Bowsher, C.N. Archer et al., "A 3D Gantry Single Photon Emission Tomograph with Hemispherical Coverage for Dedicated Breast Imaging," *Nucl. Instr. Meth. Phys. Res. A* **497**, 157-167 (2003).
[23] R.L. McKinley, M.P. Tornai, C.N. Archer et al., "Quasi-monochromatic beam measurements for dedicated cone-beam mammotomography of an uncompressed breast," presented at the *7th International Workshop on Digital Mammography*, Durham, NC, 2004 (unpublished).
[24] M.P. Tornai, R.L. McKinley, M.L. Bradshaw et al., "Effects of uncompressed breast composition and thickness on image quality using a quasi-monochromatic beam for computed mammotomography," presented at the *7th Int. Workshop on Digital Mammography*, Durham, NC, 2004 (unpublished).
[25] R. Ning, B. Chen, D. Conover et al., "Flat panel detector-based cone beam volume CT mammography imaging: preliminary phantom study," *Proc. SPIE* **4320**, 601-610 (2001).
[26] J.M. Boone, A.L.C. Kwan, J.A. Seibert et al., "Technique factors and their relationship to radiation dose in pendant geometry breast CT," *Med. Phys.* **32** (12), 3767-3776 (2005).
[27] R.L. McKinley, C.N. Brzymialkiewicz, P. Madhav et al., "Investigation of cone-beam acquisitions implemented using a novel dedicated mammotomography system with unique arbitrary orbit capability," *Proc. SPIE: Phys. of Med. Imag.* **5745**, 609-617 (2005).

Appendices

Appendix A

STATEMENT OF WORK

Task 1 Implement prototype system for unique acquisition capabilities (Months 1-12)

a. Implement mounting system for X-ray source and detector for flexible acquisitions involving azimuthal rotation and polar tilt (Months 1-2)
b. Automate data acquisition sequence, synchronizing detector readout in software with gantry control and generator exposure initiation (Months 2-3)
c. Perform initial phantom measurements using Catphan and other 3D geometric frequency/resolution phantoms to optimize cone-beam reconstruction, utilizing ordered subsets based iterative transmission reconstruction techniques for 3D cone-beam acquisition (Months 4-6)
d. Using simple acquisition geometries, optimize image gain, offset, and line correction algorithms to maximize projection image quality and noise reduction (Months 5-7)
e. Design and evaluate offset half cone-beam using 360 degree acquisition as well as horizontal versus vertical positioning of detector for maximizing range of uncompressed breasts accommodated (Months 8-12)

Task 2 Design and evaluate unique acquisition geometries (Months 13-26)

a. Investigate unique 3D cone-beam orientations and tilt angles for optimal orientation relative to the longitudinally oriented patient chest wall (Months 13-18)
b. Evaluate feasibility of utilization of patient bed motion versus camera system motion to provide vertical displacements *during* a scan at specific azimuthal and polar acquisition angles, to circumvent the physical limitations of the patient's torso by exploiting the unhindered spaces along the sides of the patient (Months 19-23)
c. Modify patient bed materials and breast opening size as well as bed contour to maximize curvature (and comfort) of patient chest for full volumetric sampling, including chest wall (Months 23-26)

Task 3 Evaluate various breast sizes, compositions, lesion sizes, microcalcifications (Months 27-36)

a. Evaluate different breast sizes, compositions, lesion sizes, microcalcifications to determine upper and lower detection limits as well as effect on breast volume sampling (Months 27-31)
b. Evaluate system and acquisition methodologies for effects on image quality including signal to noise ratio, dose efficiency, contrast sensitivity, resolution metrics (2D and 3D MTF, NPS, DQE), artifacts, and attenuation coefficient (quantitation) accuracy (Months 32-36)
c. Determine normalized glandular dose coefficients for CmT acquisitions for dose determination in preparation for clinical trials (Months 32-36)

Appendix B

SPIE 2005 Medical Imaging Conference – presented San Diego, February, 2005.

Design and Development of a Fully-3D Dedicated X-ray Computed Mammotomography System

Martin P. Tornai[1,2] , Randolph L. McKinley[1,2], Caryl N. Brzymialkiewicz[1,2], Priti Madhav[1,2], Spencer J. Cutler[1,2], Dominic J. Crotty[1,2], James E. Bowsher[1], Ehsan Samei[1,2,3], Carey E. Floyd, Jr.[1,2]

[1] Department of Radiology, Duke University Medical Center, Durham, NC
[2] Department of Biomedical Engineering, Duke University, Durham, NC
[3] Department of Physics, Duke University, Durham, NC

ABSTRACT

Our effort to implement a volumetric x-ray computed mammotomography (CmT) system dedicated to imaging breast disease comprises: demonstrated development of a quasi-monochromatic x-ray beam providing minimal dose and other optimal imaging figures of merit; new development of a compact, variable field-of-view, fully-3D acquisition gantry with a digital flat-panel detector facilitating more nearly complete sampling of frequency space and the physical breast volume; development of a comfortable patient support and positioning structure providing imaging of a pendant breast; incorporation of iterative ordered-subsets transmission (OSTR) image reconstruction allowing modeling of the system matrix. Here, we describe the prototype 3D gantry and demonstrate initial system performance. Data collected on the prototype gantry demonstrate the feasibility of using OSTR with realistic reconstruction times. The gantry consists of a rotating W-anode x-ray tube using ultra-thick K-edge filtration, and an ~20x25cm^2 digital flat-panel detector located at <60cm SID. This source/detector combination can be shifted laterally changing the location of the central ray relative to the system center-of-rotation, hence changing the effective imaging field-of-view, and is mounted on a goniometric cradle allowing <50˚ polar tilt, then on a 360˚ azimuthal rotation stage. Combined, these stages provide for positioning flexibility in a banded region about a sphere, facilitating simple circle-plus-arc-like trajectories, as well as considerably more complex 3D trajectories. Complex orbits are necessary to avoid physical hindrances from the patient while acquiring the largest imaging volume of the breast. The system capabilities are demonstrated with fully-3D reconstructed images of geometric sampling and resolution phantoms, a fabricated breast phantom containing internal features of interest, and a cadaveric breast specimen. This compact prototype provides flexibility in dedicated, fully-3D CmT imaging of healthy and diseased breasts.

Keywords: X-ray computed mammotomography, quasi-monochromatic, orbits, iterative reconstruction, uncompressed breast imaging, 3D.

1. INTRODUCTION

There are various groups, that we are aware of, investigating dedicated computed mammotomography (CmT) imaging with hardware approaches [1,2] for both screening and diagnosis, and there are others performing simulations in order to arrive at suitable geometries [3]. Our overall endeavor includes development of a dual-modality, structural and functional (molecular) imaging device [4,5], based on a 3-dimensional gantry, initially developed for dedicated single photon emission computed tomography (SPECT) breast imaging [6]. The CmT development could also be used independently of the combined molecular imaging approach for either screening or diagnosis.

We have made extensive simulations and initial measurements considering development of the quasi-monochromatic x-ray beam with commercially available components [7-13], and have begun to incorporate

the tested projection beam measurement geometries into the fully-3D positioning gantry hardware (Fig. 1). Our studies on complex 3D trajectories for emission imaging [14,15] can be suitably applied to the transmission imaging case as well [16], and exploit the flexibility of the gantry system. In this study, we describe the unique capabilities and features of the dedicated breast imaging system, and provide data indicating some of the key benefits of this approach.

METHODOLOGY

System Components

The dedicated CmT system is composed of a tungsten-target X-ray tube (model Rad-94, 0.4 mm focal size, 14º anode angle, *Varian Medical Systems*, Salt Lake City, UT) and CsI(Tl)-TFT digital flat panel x-ray detector (model Paxscan 2520, 1920x1536 pixels, 127 μm pixel size, *Varian Medical Systems*, Salt Lake City, UT) mounted on a 1.27 cm thick Al plate. This plate is then mounted on a goniometer (model BGM200PE, *Newport Corp*., Irvine, CA) which allows a practical polar tilting capability and angular range of 50º (30º in one direction and 20º in the other, due to physical limitations of the tube, goniometer, and motor location). This whole assembly is then placed on a rotation stage (model RV350CC, *Newport Corp*., Irvine, CA) which allows a full 360º azimuthal rotation. The source-to-image distance (SID) used in our setup was 55 cm, with a source to object center distance of 35 cm.

The azimuthal and polar motions of the system (Fig. 1) are controlled by the ESP6000 controller (*Newport Corp*., Irvine, CA) which is further connected to the main system computer (2.5 GHz, 500M RAM, Windows XP, *Pogo Linux Inc*., Redmond, WA). The system computer is also the coordinator of all system activities during an acquisition, including gantry motion control as described previously, Paxscan frame acquisition, x-ray generator control, and synchronization. Projection acquisition is done via a framegrabber card (model PIXCI D2X, *Epix Inc.*, Buffalo Grove, IL) connected to the video port of the Paxscan controller. The high-frequency x-ray generator (model CPX160, *Electromed Inc.,* Montreal, PQ) is controlled via relays on a multifunction card (model PCI-1761, *Advantech Inc*., Sunnyvale, CA) mounted in the system computer. The same multifunction card contains digital I/O ports which are connected to the Paxscan controller to provide synchronization, ensuring the projections are not acquired during the frame readout period.

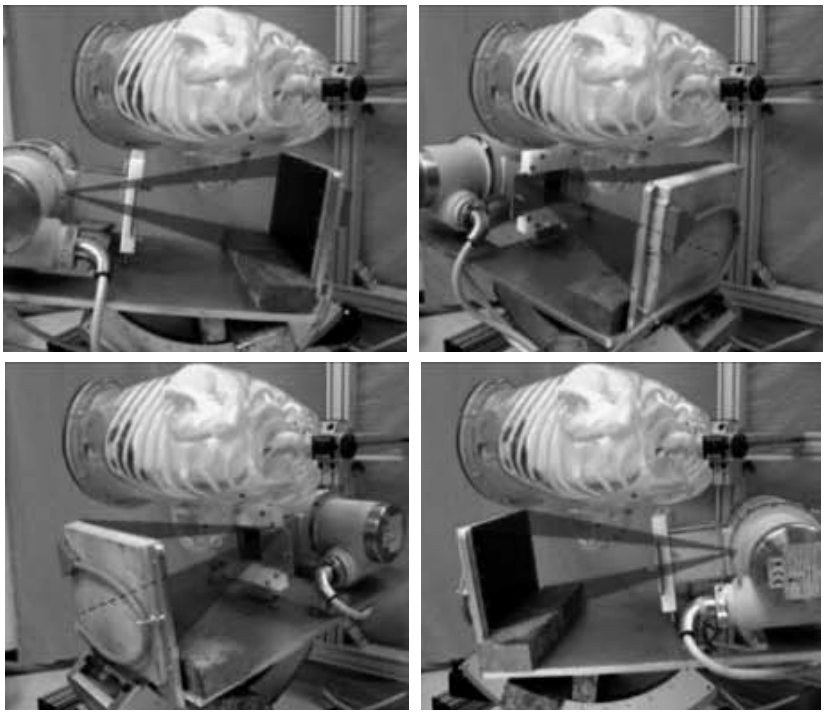

Figure. 1. (Top Left to Bottom Right) System setup illustrates x-ray tube and digital x-ray detector with 55cm SID, mounted on a laterally shiftable plate, all on a goniometer, then on an rotation stage for fully 3D CmT. The goniometer provides polar tilt in a 50˚ range from a horizontally level central ray, while the rotation stage provides full 360˚ azimuthal rotation. Dark borders represent upper and lower cone-beam boundaries, seen in an early CmT implementation.

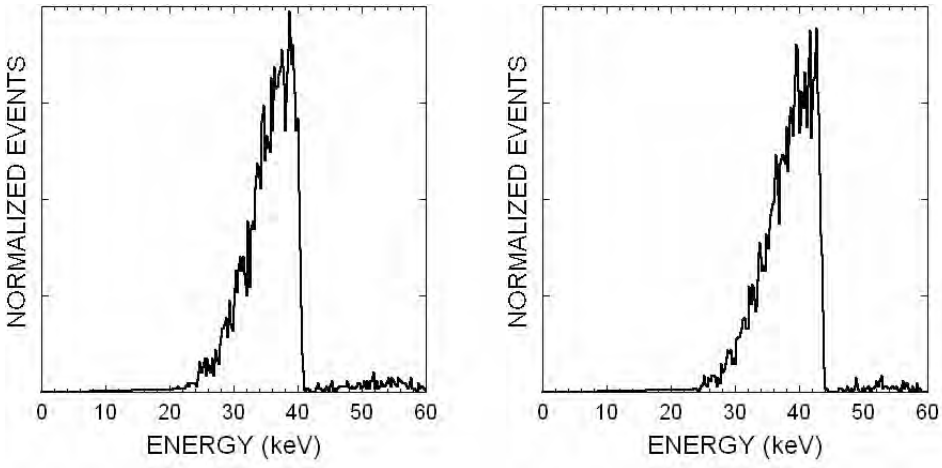

Figure 2. Measured pre-breast spectra for 100th value attenuating layers of (Left) Ce and (Right) Nd.

The system is currently run at 1-2 fps in fluoroscopic mode with onboard 2x2 binning, providing an acquisition time of 2-4 minutes per scan, but has the capability of running at 30 fps, potentially reducing acquisition time to less than 30 seconds. Each acquisition is preceded by gain and offset calibrations using 32 calibration frames.

Tube potential for these studies ranges from 60 to 65 kVp, with exposures varying depending on the object being studied. We have shown that full CmT acquisitions can be performed at or below the exposure (dose) of dual view mammography [8-13].

We have also shown previously [8-11] that a quasi-monochromatic beam can be produced by using thick K-edge filters which can improve exposure and dose efficiency by a factor of 3X. This has been confirmed through both simulations and experiments. The energy range that provides optimal dose efficiency for a clinical range of uncompressed breast sizes (13-19 cm, from [17]) is approximately 30-40 keV. We have acquired unique K-edge filter materials which allow us to generate quasi-monochromatic beams with mean energies within this range (Fig. 2). For example, Ce (Z=58, ρ=6.657 g/cm^3, K-edge=40.443 keV) provides a mean energy of 34.6 keV, suitable for low to mid-sized breasts, and Nd (Z=60, ρ=6.90 g/cm^3, K-edge=43.569 keV) can be used for larger breasts, with a mean energy of 38.6 keV. These filter materials have been rolled to precise thicknesses for our specifications (*Santoku America, Inc.*, Tolleson, AZ). The data shown here have been acquired using both Ce (t=0.0508 cm, t=0.0708 cm) at 100th and 250th value attenuating layer and Nd (t=0.057 cm) at 100th value attenuating layer. The filters are housed in a custom built collimator attached to the x-ray tube. With such precise control of the energy spectrum, and since there is very little beam hardening or other change in the post-breast energy spectrum, dual energy imaging is potentially an easily implemented approach to enhanced breast tomography.

Offset Geometry

Uncompressed breast sizes range from 13 to 19 cm [17] and we have developed a set of pendant breast phantoms which spans this range [18]. With our system magnification of 1.57, this causes the breast dimension to exceed the active area at the detector. In order to prevent truncation artifacts, and to increase the effective range of breast sizes that can be fully imaged within the detector active area, we have developed an offset geometry [5,16] where the detector and focal spot are offset laterally from the center of rotation (Fig. 3). With the offset geometry and a 360º acquisition, we can image a much wider range of breast sizes without moving to a larger detector [19]. Moreover, the offset geometry may also provide modest scatter reduction, by exploiting the self-absorptive nature of the breast half with no incident x-rays during the scan.

The offset geometry is examined with a 935 mL water-filled breast phantom (*Radiology Support Devices*, Newport Beach, CA) containing an 8 mm inner diameter, acrylic walled, "air" lesion (*Data Spectrum*, Hillsborough, NC) suspended on an acrylic rod with an ~1 mm diameter "air" neck abutted to an ~2 mm diameter "air" neck. The breast phantom dimensions were 15 cm medial-to-lateral, 20 cm superior-to-inferior, and 7.4 cm nipple-to-chest [18].

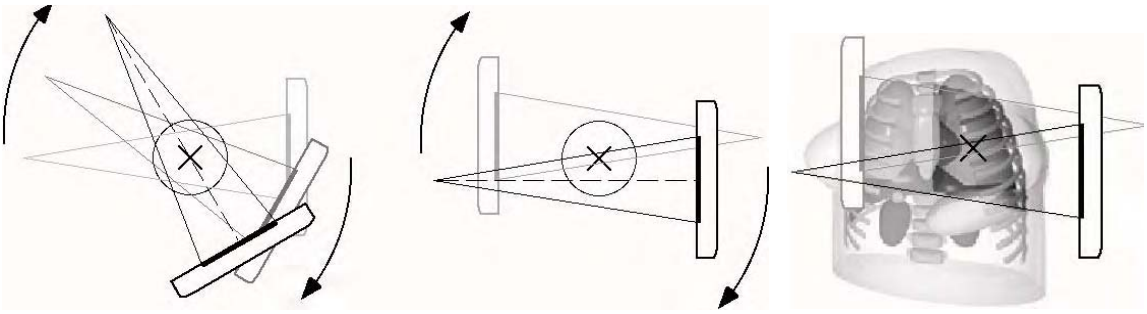

Figure 3. (Left) Graphic illustrating truncation occurring in large breast for 3 projection views. (Middle) Offset geometry and 360º acquisition to collect conjugate views allows just over half the breast volume in each projection, thereby increasing the range of breast sizes that can be fully imaged without truncation artifacts. (Right) Anterior view including 3D rendition of torso illustrating conjugate views about a pendant breast.

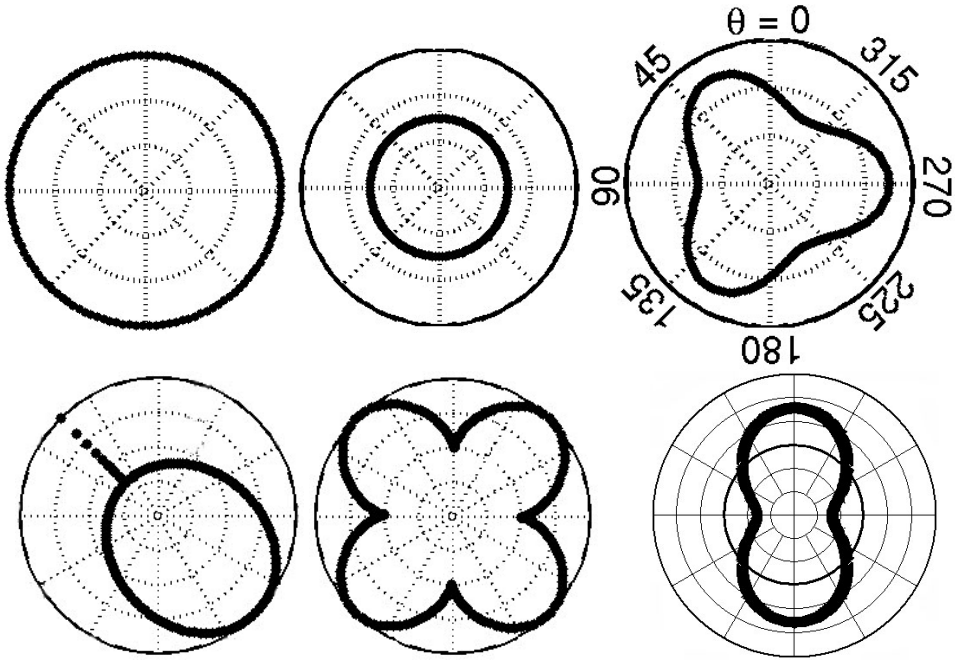

Figure 4. Several polar plots showing implemented trajectories traversed by the CmT system. Azimuthal angles are indicated around the circumference, and polar tilt by the radius from the center; the trajectory is the thick, dark line bounded by the largest circle. (From Top-Left to Lower-Right) Orbits are: VAOR, simple tilted circle, 3-lobed projected sinusoid, circle-plus-arc, cloverleaf, and Saddle. (Lower Right) The Saddle orbit has both +/- polar tilt (-30º at center, +30º at edge of circle), and 0º tilt is illustrated as the broader line at the 3rd ring. VAOR has a fixed 0º polar tilt and tilted circle has a 15º fixed polar tilt for all azimuthal angles. All other orbits vary polar and azimuthal angles simultaneously.

Complex Orbits

With the azimuthal and polar motions made possible by the rotation stage and goniometer, the dedicated CmT system can perform a nearly infinite number of acquisition trajectories or orbits (Fig. 4). These acquisition orbits could be simple, such as a circular Vertical-Axis-Of-Rotation (VAOR), or a simple Circle-Plus-Arc, or considerably more complex, such as Projected-Sinusoid, and others (Fig. 4) [15].

Here, we summarize results from the VAOR and Saddle orbits evaluated in detail in [20]. These orbits are significant for two reasons: (1) polar tilts enable the ability to meet Tuy's data sufficiency condition [21], thereby reducing or eliminating cone-beam distortion artifacts, especially at the peripheral cone-beam planes; and (2) these types of flexible 3D orbits allow the system the ability to contour the patient and palette, in order to avoid physical limitations (e.g. patients' head or shoulders) and physical aggravation (i.e. many patients cannot comfortably arch their backs, and thus extend their breasts into the field of view) and thereby image closer to the chest wall. Note that by utilizing our integrated rotation stage and goniometer, any arbitrary orbit is made possible with this gantry system. So, in principle, orbits can be

symmetric for patients or objects presenting very little physical hindrance, or they can be completely arbitrary. In either case, the orbits require only that there be a 360º azimuthal rotation, and that the polar tilt approaches or exceeds the anode angle during the scan.

Geometric and Realistic Phantoms

Measurement results are shown using a 7.7 cm diameter disc phantom ("Defrise") for cone-beam distortion (model ECT/MI-DEF/P, 5.0 mm acrylic disk thickness, 5.0 mm disk spacing, 5 cm extent, *Data Spectrum Corp.*, Hillsborough, NC), and a 7.5 cm diameter low scatter acrylic resolution phantom (rods-in-air) (model ECT/DLX-MP, 1.1, 1.5, 2.3, 3.1, 3.9, and 4.7 mm rod sizes, *Data Spectrum Corp.*) for resolution. The outer length of the cylindrical container is 12 cm in height. Preclinical imaging is performed with a 700 mL compressible breast phantom with chest plate (*Radiology Support Devices*, Newport Beach, CA) containing oil, and with some inserted objects like a shaped sponge to provide simulated structure [18]. A cadaveric breast tissue sample from a 48 year-old is also imaged, supported in a plastic breast shaped bowl.

Reconstructions

Data reconstructions use a modified ray-tracing iterative ordered subsets transmission (OSTR) algorithm [22] that accounts for the unique trajectories of the x-ray source-detector pair. Projection images are currently binned either to 8x8 or 4x4 pixels to reduce the dataset size for faster reconstruction times. It is anticipated, with future system enhancements that 2x2 and 1x1 data sets could be reconstructed. We currently use 8 subsets, and up to 15 iterations, with reconstructed voxel sizes of 0.125 mm^3 and 1 mm^3. Reconstruction with the OSTR algorithm allows us to develop and evaluate any arbitrary 3D trajectory without having to consider 3D filtering in the frequency domain; some orbits may not have closed form filter solutions, especially those designed *ad hoc* for specific patients. There may be simple and elegant means to reconstruct some symmetric data with linear reconstruction algorithms, but still the use of OSTR allows modeling of the system matrix. Indeed, our long term goal is for combined emission and transmission functional and structural) tomography, and the using iterative algorithms will also allow joint reconstructions of the data.

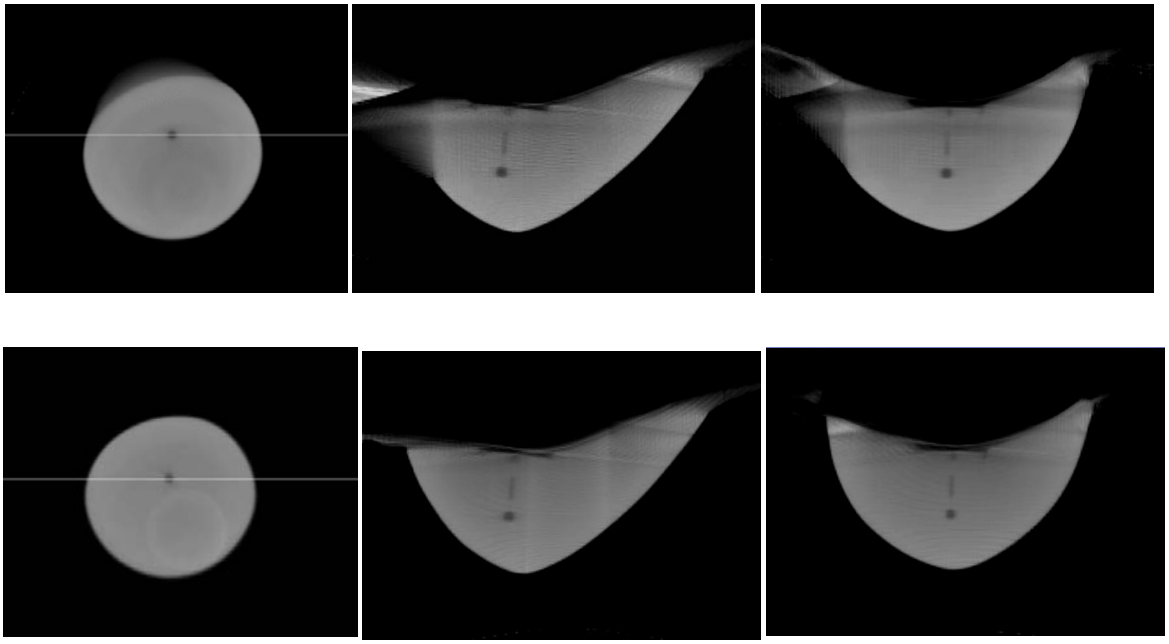

Figure 5. Reconstructed, water filled large breast (0.94 L) phantom for (Top Row) centered geometry and (Bottom Row) offset geometry with (Left Column) axial slice (3 summed slices), at the level of the lesion, (Middle Column) sagittal slice, and (Right Column) coronal slice.

Table 1. Attenuation coefficient results for large breast in the centered and offset geometries.

	Measured μ edge	Theoretical μ	Coefficient Error
Central Large Breast	0.1043-0.2590	0.2789	7.2-62.6%
Offset Large Breast	0.2663	0.2789	4.6%

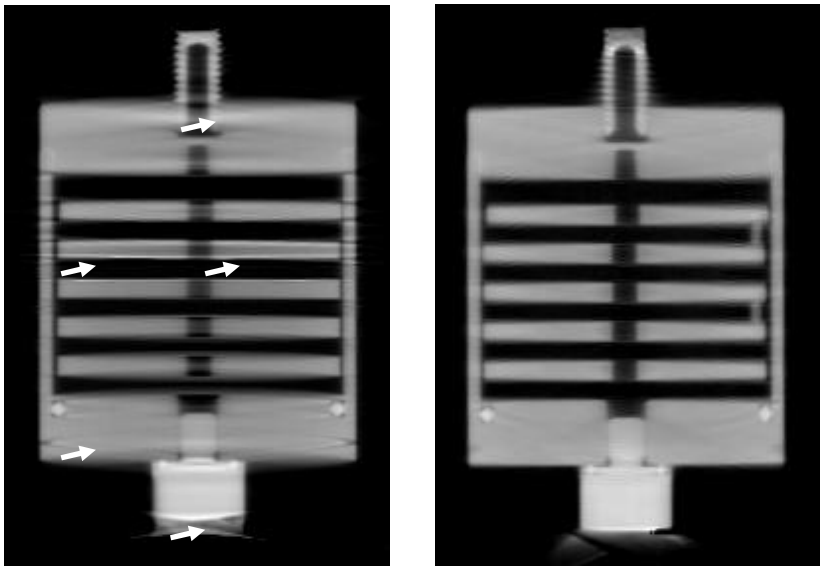

Figure 6. Sagittal slices of 10th iteration of reconstructed Defrise phantom for (Left) VAOR, and (Right) Saddle orbits. Arrows in left (VAOR) slice indicate regions of artifacts that are not readily apparent in the Saddle data. Several of these regions occur at interfaces of materials in the phantom.

SELECTED RESULTS AND DISCUSSION

Offset Geometry

For the 935 mL breast phantom, truncation effects are clearly visible in all views with the centered beam (Fig. 5). With a 5 cm offset central ray geometry, these truncation artifacts have been effectively eliminated, and the range of manageable breast sizes has been significantly increased, even with this small shift.

The magnitude of the error induced by truncation artifacts is evident when examining the attenuation coefficient for the centered geometry (Table 1) [19]. A wide range of coefficients are measured in and around the region of truncation distortion, resulting in an error range of 7.2-62.6% versus the theoretical coefficient value. For the offset geometry, the attenuation coefficient results from the reconstructed transaxial slices shows a <5% error.

Complex Orbits - Sampling

The reconstructed sagittal slices of the Defrise phantom (Fig. 6) indicate that the Saddle orbit provides significant (qualitative) improvement in the reduction of streaking and distortion artifacts due to the

otherwise insufficient sampling with simple circular cone-beam geometries. The Saddle orbit reconstruction shows very consistent shape and density for all 5 discs and edges of the cylindrical holder (height = 12 cm), whereas the VAOR orbit shows significant distortions away from the central slice. This indicates that cone beam distortions at the outer planes can be reduced using our unique complex orbit capability.

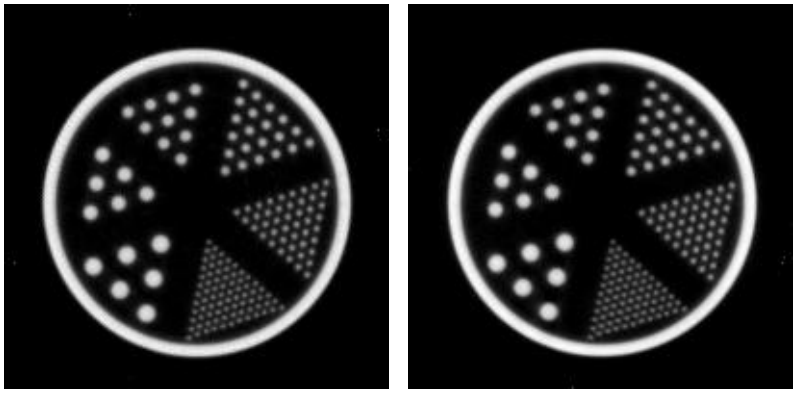

Figure 7. Reconstructed transaxial slices through low scatter rods in air for (Left) VAOR and (Right) Saddle orbits. Rod sizes are indicated in the ***Methods***, and are spaced on twice their diameters.

Complex Orbits - Resolution

Initial OSTR reconstruction of a rod phantom (in air) demonstrate the ability to resolve <1.1 mm objects. A preliminary investigation of the effect of the orbits on resolution (Fig. 7) indicates that there is no degradation of resolution for the Saddle orbit versus the simple circular (VAOR) orbit. Degradations are not evident with other complex orbits as well [19]. The smallest rods (1.1 mm) were readily visible for both orbits shown here, and there were no noticeable differences between the Saddle and the VAOR orbits. The transverse slices used for this comparison are near the central plane. Plans to evaluate the full 3D MTF of the mammotomography system are underway.

Complex Orbits – Breast Phantom and Cadaveric Breast Tissue

The complex orbit capability of the system allows physical limitations of the contours of the patient (and bed, or other support) to be overcome. An example of this ability is illustrated with a 700 mL compressible breast phantom and artificial chest plate (Fig. 8) [18]; the chest plate necessitated that a complex (i.e. non-circular) orbit be used. Reconstructed transaxial, sagittal and coronal slices through the oil/sponge filled breast phantom demonstrate the full 3D nature of breast visualization, with a calcification seen in all three views, surrounded by turbid media. Much of the structural noise is removed due to the tomographic nature of the dataset, and features like the dramatically improved contrast of embedded objects (e.g. the air sphere) are readily apparent.

An initial CmT scan was performed on room temperature breast tissue from a (fresh frozen) 48-year old cadaver. Breast tissue results (Fig. 9) indicate that a complex orbit can be used to acquire biological data, and can potentially produce quality images where overlapping tissue is removed and distortion is reduced. As for the breast phantom images, objects can be followed 3-dimensionally, which may allow isolated objects to be more easily distinguished from those connected to internal connective tissue, ductile systems, etc.

Conclusions

This dedicated CmT implementation is a departure from “traditional,” static cone beam x-ray transmission imaging approaches and opens up a new class of acquisition geometries with a nearly infinite number of possible acquisition trajectories in the hemispherical (pendant breast) imaging domain. Since breasts are not isolated objects in space, adequately imaging them with simple circular trajectories and cone beam x-ray geometries may have some limitations on (1) adequate sampling due to insufficient cone beam sampling, as well as (2) reduced sampling due to physical limitations of the patient, (3) reduced proximity to the chest wall on patients unable to arch their backs, (4) scatter-to-primary ratios, etc. The novel imaging system summarized in this work may help overcome some of these limitations due to the flexible, 3D positioning platform for the x-ray source-detector system. Additional features include the ability to have an

offset (half cone beam) sampling strategy, which may reduce scatter in the projections and potentially reduce breast dose further than those reductions due to the quasi-monochromatic x-ray beam.

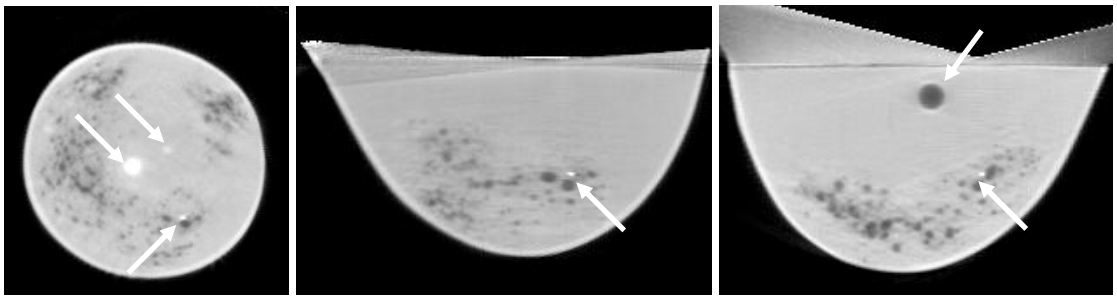

Figure 8. Reconstructed oil/sponge breast phantom acquired with Saddle orbit, shown for (Left) transaxial, (Middle) sagittal, and (Right) coronal slices. White arrows (from below) indicate oyster shell calcification seen in all views. Arrows (from above) indicate (Left) Delrin and nylon rods, and (Right) 8 mm diameter air sphere in acrylic. Black porous holes are due to the fine sponge material inserted in the breast phantom (please see [18]).

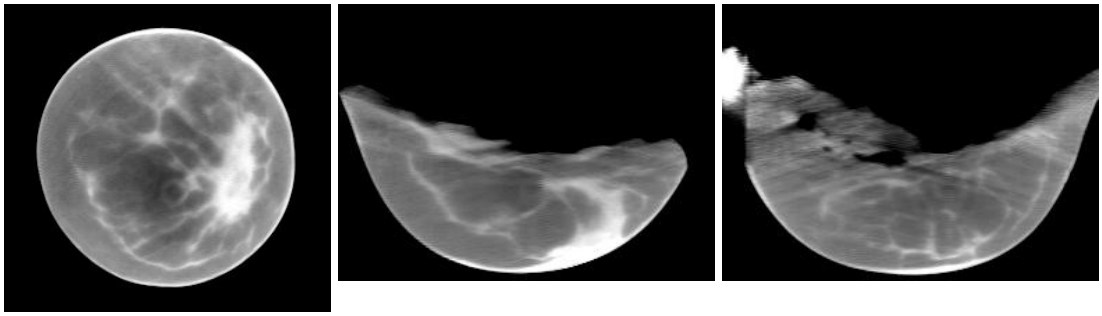

Figure 9. Reconstructed cadaveric breast tissue acquired with Saddle orbit, shown for (Left) transaxial, (Middle) sagittal, and (Right) coronal slices. Note high contrast of skin at boundary and connective tissue internal to the breast.

Applications may also apply to other types of x-ray CT and, indeed, small animal imaging with high resolution was demonstrated, and is being further investigated. With the versatile gantry configuration, physical obstacles in the more-nearly-complete data acquisition sequence can be more easily remedied. Combined with the iterative OSTR, quasi-monochromatic cone beam source and flat panel detector, this compact integrated system could play a significant role in fully-3D, quantitative structural imaging of breast disease, leading to *in vivo* lesion detection as well as characterization.

ACKNOWLEDGEMENT

This work is supported by NIH Grant R01-CA96821, with additional support from DOD DAMD17-03-1-0558.

REFERENCES

[1] J.M. Boone, T.R. Nelson, K.K. Lindfors, J.A. Siebert. "Dedicated breast CT: radiation dose and image quality evaluation," *Radiology*, **221**:657-667, 2001.

[2] B. Chen, R. Ning. "Cone-beam volume CT mammographic imaging: feasibility study," *Med. Phys.*, **29**(5):755-770, 2002.

[3] A.A. Vedula, S.J. Glick, X. Gong. "Computer simulation of CT mammography using a flat-panel imager," *Proc. of SPIE Med. Imag. 2003*, **5030**:349-360, 2003.
[4] M.P. Tornai, J.E. Bowsher, C.N. Archer, *et al*. "A compact dedicated device for dual modality radionuclide imaging of the breast with an Application Specific Emission and Transmission Tomograph (ASETT)," *Radiology*, **221P**:555, 2001.
[5] M.P. Tornai, J.E. Bowsher, C.N. Archer, R.J. Jaszczak. "Feasibility of Application Specific Emission and Transmission Tomography (ASETT) of the breast," *J. Nucl. Med.*, **43**(5):12P, 2002.
[6] M.P. Tornai, J.E. Bowsher, C.N. Archer, *et al*. "A 3D gantry single photon emission tomograph with hemispherical coverage for dedicated breast imaging," *Nucl. Instr. Meth.*, **A497**(1):157-167, 2003.
[7] M.L. Bradshaw, R.L. McKinley, E. Samei, C.N. Archer, M.P. Tornai. "Initial x-ray design considerations for Application Specific Emission and Transmission Tomography (ASETT) of the breast," *J. Nucl. Med.*, **44**(5):287P, 2003.
[8] R.L. McKinley, M.P. Tornai, E. Samei, M.L. Bradshaw. "Optimizing beam quality for x-ray computed mammotomography (CmT)," *Proc. SPIE: Physics of Medical Imaging*, **5030**(2):575-584, 2003.
[9] R.L. McKinley, M.P. Tornai, E. Samei, M.L. Bradshaw. "Simulation study of a quasi-monochromatic beam for x-ray computed mammotomography," *Med. Phys.*, **31**(4):800-813, 2004.
[10] R.L. McKinley, M.P. Tornai, E. Samei, M.L. Bradshaw. "Initial study of quasi-monochromatic beam performance for x-ray computed mammotomography," Presented at *IEEE Nucl. Sci. Symp. Med. Imag. Conf.*, Portland, Oregon, October 19-26, 2003, and submitted to *IEEE Trans. Nucl. Sci*.
[11] R.L. McKinley, E. Samei, M.P. Tornai, C.E. Floyd. "Measurements of a quasi-monochromatic beam for x-ray computed mammotomography," *Proc. of SPIE Med. Imag*,. **5368**:311-319, 2004.
[12] M.P. Tornai, R.L. McKinley, E. Samei, C.E. Floyd, M.L. Bradshaw. "Effects of uncompressed breast composition and thickness on image quality using a quasi-monochromatic beam for x-ray computed mammotomography," Presented at *7th IWDM*, Chapel Hill, NC,18-21 Jun. 2004.
[13] R.L. McKinley, M.P. Tornai, E. Samei, J.E. Bowsher. "Quasi-monochromatic beam measurements for dedicated cone-beam mammotomography of an uncompressed breast," Presented at *7th IWDM*, Chapel Hill, NC,18-21 Jun. 2004.
[14] C.N. Archer, M.P. Tornai, J.E. Bowsher, S.D. Metzler, B.C. Pieper, R.J. Jaszczak. "Implementation and initial characterization of acquisition orbits with a dedicated emission mammotomograph," *IEEE Trans. Nucl. Sci.* **NS-50**(3):413-420. 2003.
[15] C.N. Archer, M.P. Tornai, R.L. McKinley, J.E. Bowsher. "Evaluation of fully 3D emission mammotomography with a compact cadmium zinc telluride detector," *IEEE Trans. Med. Imag.* (Submitted) 2005.
[16] M.P. Tornai, C.N. Archer, J.E. Bowsher, R.L. McKinley, R.J. Jaszczak. "Transmission imaging with a compact gamma camera: initial results for mammotomography," *IEEE Nucl. Sci. Symp. and Med. Imag. Conf. Rec.*, **3**:1597-1601, 2002.
[17] J.M. Boone, N. Shah, T.R. Nelson, "A comprehensive analysis of DgN_{CT} coefficients for pendant-geometry cone-beam breast computed tomography," *Med. Phys.* **31(2)** 226-235, 2004.
[18] M.P. Tornai, R.L. McKinley, C.N. Brzymialkiewicz, S.J. Cutler, D.J. Crotty. "Anthropomorphic breast phantoms for preclinical imaging evaluation with emission or transmission imaging," Presented at 2005 *SPIE Medical Imaging Conference*, San Diego, CA, Jan. 12-18, 2005.
[19] R.L. McKinley, M.P. Tornai, C.N. Brzymialkiewicz, E. Samei, J.E. Bowsher. "Analysis of a novel offset cone-beam computed mammotomography imaging system for attenuation correction of SPECT in a proposed dual modality dedicated breast mammotomography system," Presented at *2004 Workshop on the Nuclear Radiology of Breast Cancer*, Rome Italy, Oct 22-23, 2004, and submitted to *Physica Medica*.
[20] R.L. McKinley, C.N. Brzymialkiewicz, P. Madhav, M.P. Tornai. "Investigation of cone-beam acquisitions implemented using a novel dedicated mammotomography system with unique arbitrary orbit capability," Presented at 2005 *SPIE Medical Imaging Conference*, San Diego, CA, Jan. 12-18, 2005.
[21] H.K. Tuy. "An inversion formula for cone-beam reconstruction," *SIAM J. Appl. Math.*, **43**:546-552, 1983.
[22] H. Erdogan, J.A. Fessler. "Ordered subsets algorithms for transmission tomography," *Phys. Med. Biol.*, **44**:2835-2851, 1999.

Appendix C

SPIE 2005 Medical Imaging Conference Record

Investigation of cone-beam acquisitions implemented using a novel dedicated mammotomography system with unique arbitrary orbit capability

Randolph L. McKinley[1,2], Caryl N. Brzymialkiewicz[1,2],
Priti Madhav[1,2], Martin P. Tornai[1,2]

[1] Department of Radiology, Duke University Medical Center, Durham, NC
[2] Department of Biomedical Engineering, Duke University, Durham, NC

ABSTRACT

We investigate cone-beam acquisitions implemented on a novel dedicated cone-beam transmission computed mammotomography (CmT) system with unique arbitrary orbit capability for pendant, uncompressed breasts. We use a previously reported optimized quasi-monochromatic beam technique together with orbits made possible with a novel CmT gantry system, to evaluate Vertical-Axis-Of-Rotation (VAOR), Circle-Plus-Two-Arcs (CP2A), and Saddle trajectories. Acquisition parameters include: W target, 60 kVp tube potential, 100th VL Nd filtration, 1.25 mAs, 55 cm SID, CsI(Tl) digital flat panel x-ray detector, and 7.7cm diameter uniform disc (Defrise) and resolution phantoms. Complex orbits were also performed for a realistic breast phantom. Reconstructions used an iterative ordered subsets transmission (OSTR) algorithm with 4x4 binned projections, 8 subsets, and 10 iterations, with 0.125 mm^3 voxels. We evaluate the results for image artifacts, distortion, and resolution. Reconstructed images of the disc coronal and sagittal slices show significant distortion of the discs and phantom interfaces away from the central plane of the cone-beam for VAOR, less distortion for CP2A, and minimal distortion for the complex 3D Saddle orbit. Resolution phantoms indicate no loss of resolution with the Saddle orbit, with the smallest 1.1mm diameter rods clearly resolved. Other image artifacts such as streaking were also significantly reduced in the Saddle orbit case. Results indicate that arbitrary orbits of pendant uncompressed breasts using cone-beam acquisitions and OSTR iterative reconstructions can be successfully implemented for dedicated CmT to improve angular sampling with significant reduction in distortion and other image artifacts. This capability has the potential to improve the performance of dedicated CmT by adequately sampling the breast and anterior chest volumes of prone patients with pendant, uncompressed breasts.

Keywords: X-ray computed mammotomography, quasi-monochromatic, orbits, iterative reconstruction uncompressed breast imaging.

INTRODUCTION

Current breast imaging techniques have high false-positive and false-negative rates for breast lesion malignancy. Various modalities have been applied in unique ways in an attempt to improve diagnosis. Some groups are investigating dedicated x-ray cone-beam tomography alone [1,2,3]. Our group has proposed dual-modality computed mammotomography (CmT) and emission imaging [4,5]. Our CmT system will ultimately be incorporated with emission imaging in an attempt to improve breast lesion detection over current dual view X-ray mammography (XRM), particularly in women with radiographically dense breasts [4-14]. The CmT system could also be used in a stand-alone mode for structural mammotomographic imaging, utilizing a unique offset geometry to image a wide range of breast sizes [15].

Dedicated breast mammotomography using cone-beam acquisitions presents several challenges, two of which are investigated in this study: (1) Simple circular acquisitions with a cone-beam geometry introduce artifacts that are most pronounced in the outer planes of the cone-beam due to a failure to meet Tuy's data sufficiency condition [16]. This condition, as restated by Wang [17], is that "each projection plane passing through the object should intersect the orbit of the focal spot". For our small, compact system with a relatively wide 28º cone angle, this could introduce significant distortion for objects away from the central

plane of the cone for simple circular acquisitions; (2) Inactive space between the top of the detector/tube and the active areas causes difficulty in getting the top plane of the cone-beam close enough to sample the patient chest wall, especially when the tube/detector are in line with the longitudinal axis of the patient (Figure 1). However, complex fully 3D orbits may help overcome this limitation.

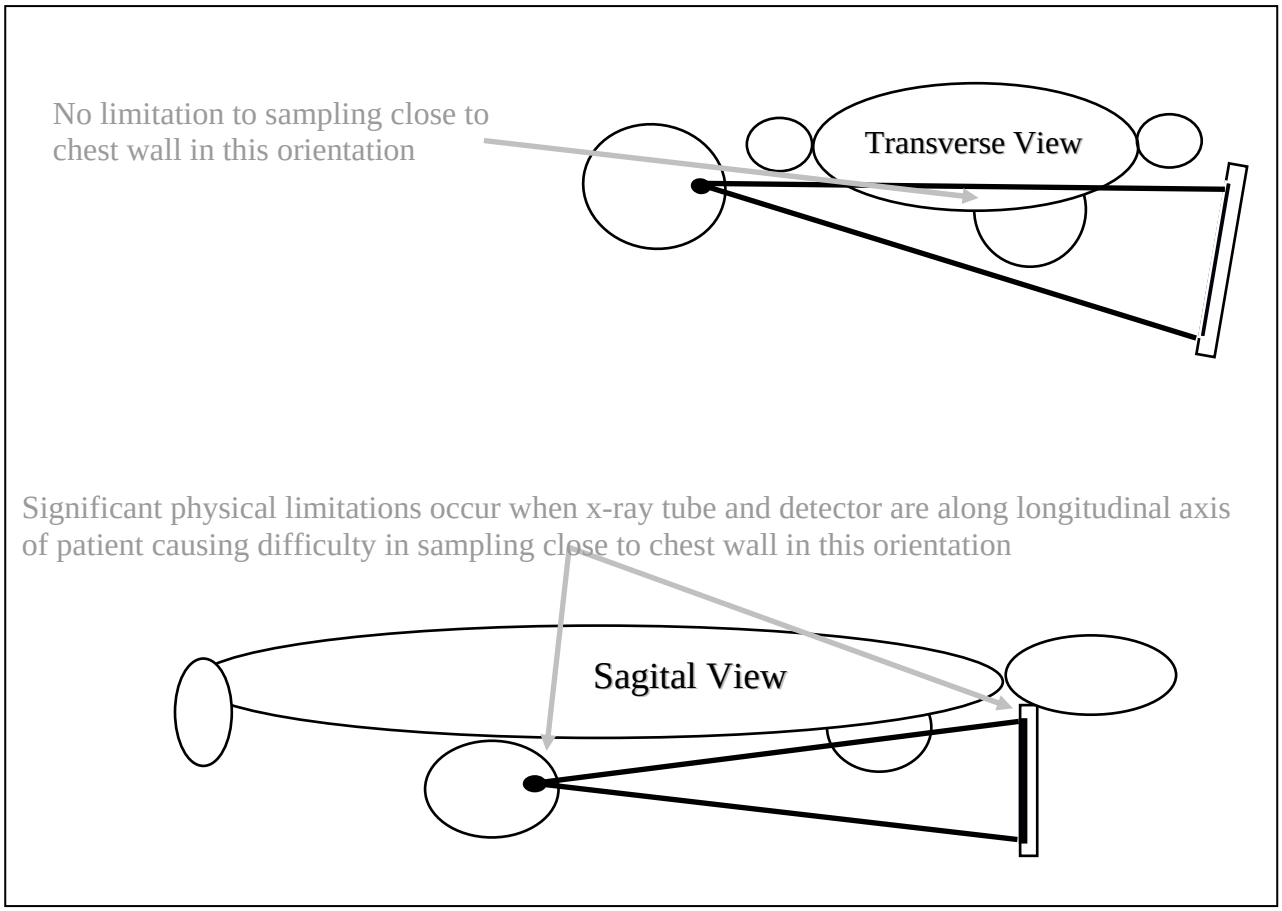

Fig.1. (top) When tube and detector are aligned in the transverse view of the patient, the "dead" zones of these devices do not, in our geometry, interfere with getting close to the chest wall. However, when they are aligned with the longitudinal axis of the patient (bottom), problems are encountered in getting the cone-beam in close proximity to the chest wall.

In this study, we investigate cone-beam acquisitions implemented on a novel dedicated cone-beam transmission computed mammotomography (CmT) system with unique arbitrary orbit capability for pendant, uncompressed breast imaging (Figure 2). We determine the necessity of complex orbits for improved sampling (as compared to simple circular acquisitions) to satisfy Tuy's data sufficiency condition, thereby reducing distortion in the outer planes. Although an infinite number of orbits are possible with our system, we evaluate the usefulness of three specific orbits, made possible by utilizing the polar tilt capability of our system, for their ability to reduce cone-beam distortion and sample closer to the chest wall.

MATERIALS AND METHODS

Experimental Parameters

We use a Nd (Z=60, ρ=6.90g/cm^3, K-edge=43.569keV) (*Santoku America, Inc.*, Tolleson, AZ) 100th value attenuating layer thick filter (t=0.057cm) to produce a quasi-monochromatic beam with mean energy (38.6 keV) within the peak exposure efficiency energy range for uncompressed breast imaging (30-40

keV)[9,11]. It was inserted into a custom built collimator attached to a tungsten-target X-ray tube (model Rad-94, 0.4mm focal size, 14º anode angle, *Varian Medical Systems*, Salt Lake City, UT). Tube potential was 60 kVp, with a 1.25 mAs exposure for the disc (sampling), high and low scatter rods (resolution), and breast phantom. The source-to-image distance (SID) used in our setup was 55cm, with a source to object center distance of 35cm. A high frequency generator provided the high voltage (model CPX160, *Electromed Inc.*, Montreal, PQ). Images were collected with a CsI(Tl) digital flat panel x-ray detector (model Paxscan 2520, 1920x1536 pixels, 127µm pixel size, *Varian Medical Systems*, Salt Lake City, UT).

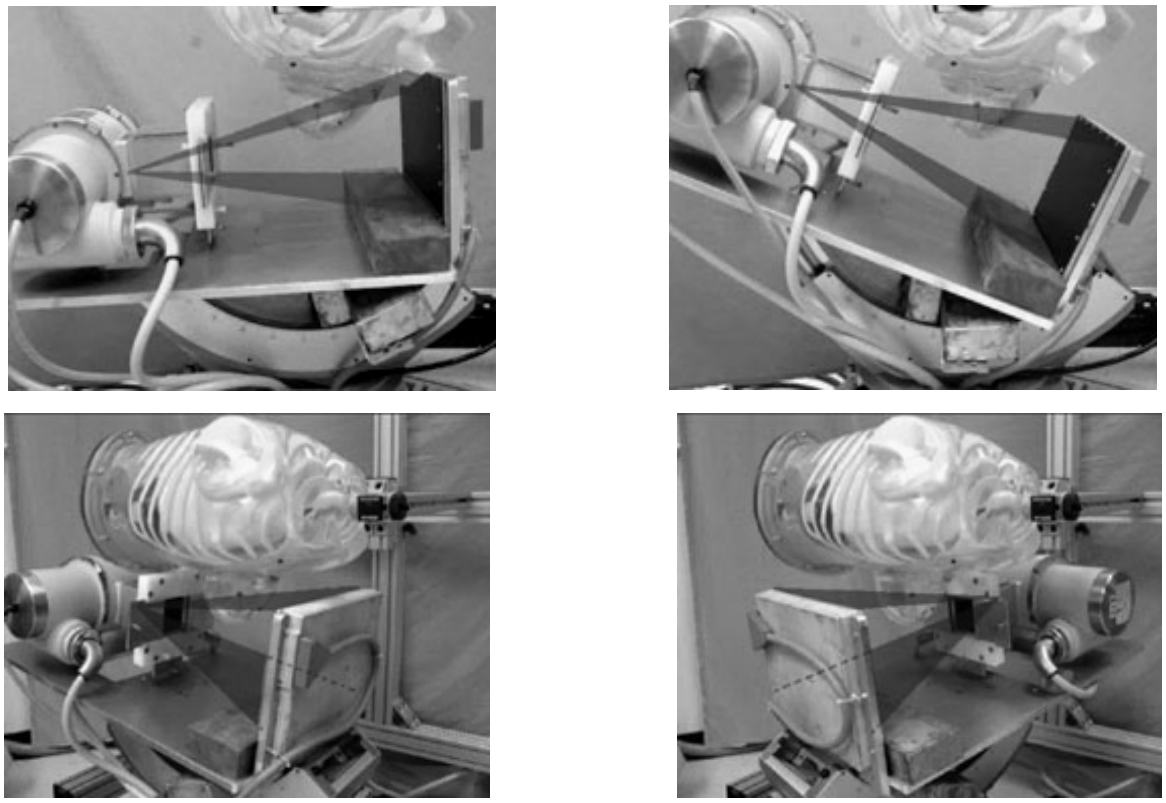

Fig. 2. Complex orbit capability of our CmT system showing (top row) tilt capability and (bottom row) azimuthal rotation about an anthromorphic torso with breast phantom(s).

Phantoms

Phantoms used included a 7.7cm diameter disc phantom ("Defrise") for cone-beam distortion measurements (model ECT/MI-DEF/P, 5mm disk thickness, 5mm disk spacing, 5cm depth, *Data Spectrum Corp.*, Hillsborough, NC), a 7.5cm diameter low scatter acrylic resolution phantom (rods-in-air) and high scatter air-rods-in-acrylic resolution phantom (model ECT/DLX-MP, 1.1, 1.5, 2.3, 3.1, 3.9, and 4.7 mm rod sizes, *Data Spectrum Corp.*, Hillsborough, NC), and a custom 700mL compressible breast phantom (*Radiology Support Devices*, Newport Beach, CA) containing a sponge and oil with some inserted objects to provide simulated structure [18].

Orbits

Our previously reported, optimized, quasi-monochromatic beam technique [8,9,11-14] together with simple and more complex orbits made possible with a novel CmT gantry [6,15], including Vertical-Axis-Of-Rotation (VAOR), Circle-Plus-Two-Arcs (CP2A), and Saddle (Figure 3) were used to acquire scans of several phantoms. Note that by utilizing our integrated rotation stage and goniometer (models RV350CC and BGM200PE, respectively, *Newport Corp.*, Irvine, CA), any arbitrary orbit is made possible with our gantry.

For all of the phantoms, the acquisitions covered a full 360º azimuthal range. Other details of the acquisitions are given in Table 1. Note that 0º polar angle is defined as the angle at which the central ray of the cone-beam is horizontal. Negative polar angles are defined as the direction in which the detector moves higher than horizontal.

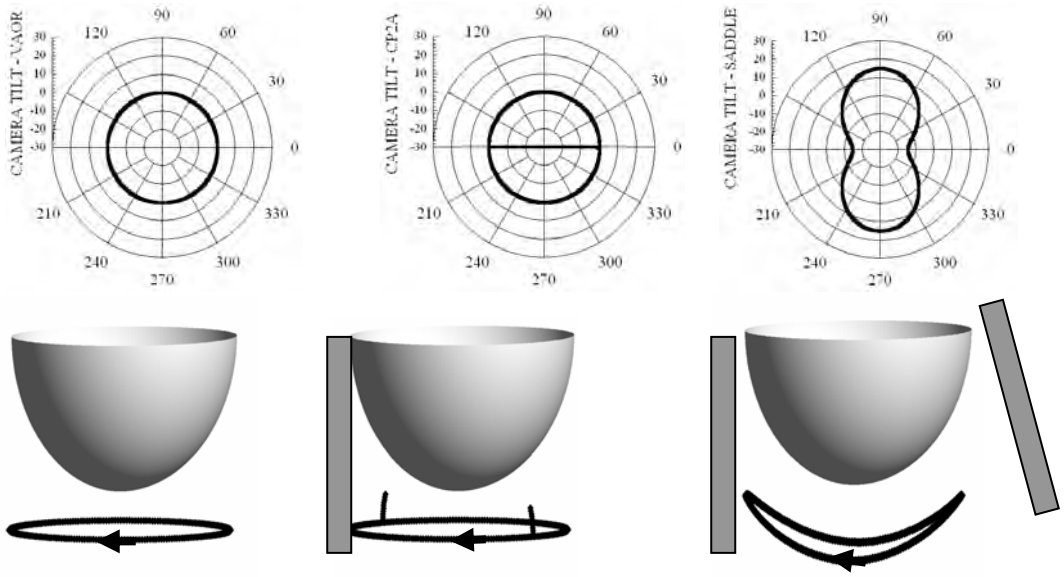

Fig. 3. (top row) Polar plots showing the trajectory traced by the CmT system for each of the three orbits including (left) VAOR, (middle) CP2A, and (right) Saddle. Azimuthal angles are indicated around the circumference of the circle and polar tilt by the radius of the circle. (bottom row) 3D descriptive renditions of the three orbits for (left) VAOR, (middle) CP2A, and (right) Saddle illustrating the movement of the detector during the acquisition.

For cone-beam distortion artifact investigations, profiles were drawn on the sagittal slices of the reconstructed Defrise phantom for all collected orbits and compared for differences in distortion and other artifacts. Profiles were also drawn on the reconstructed resolution phantom through the smallest rods (1.1mm). The breast and chest wall phantom was scanned with both VAOR and Saddle orbits, and evaluated for completeness of sampling close to the (artificial) chest plate.

Table 1. Summary of sampling details for orbits

Phantom	VAOR	CP2A	Saddle
Defrise disc phantom	240 projections, 0º polar angle	260 projections total, 240 projections and 0º polar angle for circular portion, 10 projections and 0º to -15º for each arc	240 projections, -15º to +15º polar angle
Rods-in-air and air-rods-in-acrylic resolution phantoms	240 projections, 0º polar angle	260 projections total, 240 projections and 0º polar angle for circular portion, 10 projections and 0º to -15º for each arc	240 projections, -15º to +15º polar angle
Compressible breast phantom with chest wall	240 projections, +8º polar angle	260 projections total, 240 projections and +8º polar angle for circular portion, 10 projections and +8º to -7º for each arc	240 projections, +8º to -25º polar angle

Reconstructions

Image reconstructions used a modified ray-tracing based iterative ordered subsets transmission (OSTR) algorithm [19], accounting for the 3D vantage of the source-detector pair. Gain and offset corrected projection images were binned to 4x4 pixels and reconstructed using 8 subsets, and 10 iterations, yielding a reconstructed voxel size of 0.125 mm^3.

RESULTS AND DISCUSSION

CONE BEAM DISTORTION

The reconstructed sagittal slices of the Defrise phantom (Figure 4) indicate that the Saddle orbit provides significant (qualitative) improvement in the reduction of streaking, disc shape distortion, and other artifacts due to the otherwise insufficient sampling with simple cone-beam geometries. The CP2A orbit provided some improvement over the simple circular VAOR orbit, but not to the degree that Saddle appears to improve image quality. The Saddle orbit reconstruction shows very consistent shape and density for all 5 discs (and the cylindrical container itself) whereas the VAOR orbit shows significant distortion away from the central slice. Despite the more complete sampling of the volume with the CP2A orbit, the similarity between VAOR and CP2A may be due to the fact that there is considerable overlap of the incomplete data (simple, circular orbit), and the OSTR algorithm thus biases the end result. A detailed comparison between OSTR and filtered back projection (FBP), similar to the one between OSEM and FBP for emission studies [20], may be worthwhile.

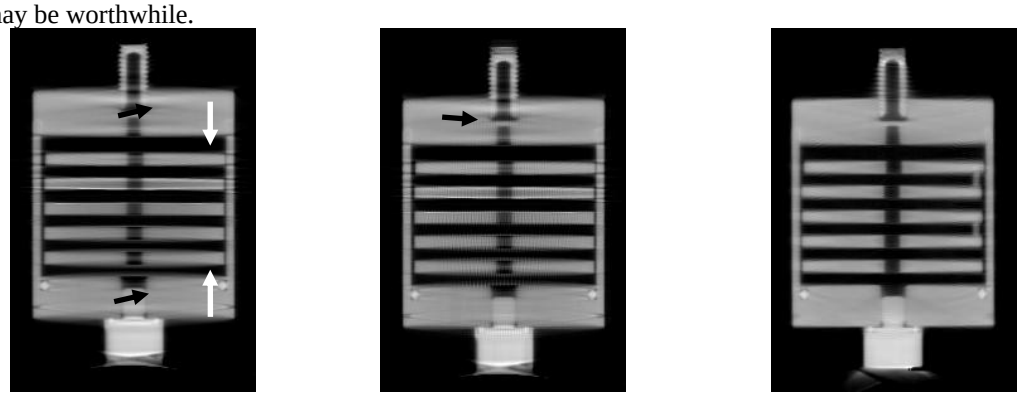

Fig. 4. 10th iteration of sagittal slice reconstruction of Defrise phantom for (left) VAOR, (middle) CP2A, and (right) Saddle orbits. (left) White arrows show position through which profiles were drawn, near the central vertical slice. Black arrows indicate some regions of streaking artifacts, with similar regions in other images showing reduced artifacts.

A review of the profiles through the discs (Figure 5) confirms the reduction in disc distortion artifacts in the saddle orbit where the profile shape for each disc is much more representative of the expected "step" shape, and the level through the disc material is more constant. This would indicate that, with our acquisition geometry (ie. short SID and wide cone angle), cone beam distortions at the outer planes of the cone are significant enough to warrant a more complex orbit to reduce these artifacts. Note that acrylic posts separating the discs are visible in the sagittal slice of the Saddle orbit, perhaps due to a slight object rotation between acquisitions. The complex geometry of a prone patient with pendant breast may warrant complex trajectories to both collect completely sampled data while avoiding physical features of the patient and support palette, and these data support the conclusion that our system is capable of acquiring and reconstructing the data.

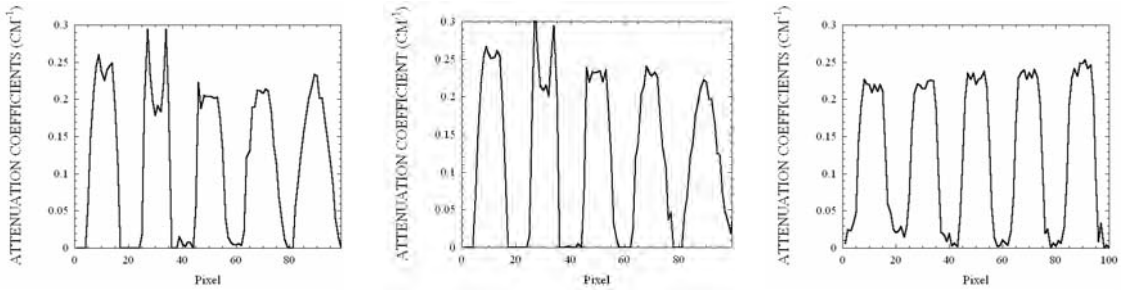

Fig. 5. Profiles through 10th iteration of sagittal slice reconstruction of Defrise phantom for (left) VAOR, (middle) CP2A, and (right) Saddle orbits. Figure 4 (left) indicates position of profile.

Resolution

A preliminary investigation of the effect of the orbits on resolution (Figure 6) indicates that there is no degradation of resolution for the Saddle orbit versus the other orbits. The smallest rods (1.1mm) were readily visible for all orbits, and there were no noticeable differences between the Saddle orbit and the other orbits for the slices used in this comparison. Profiles through the smallest rods (Figure 6, right column) indicate that resolution is unaffected by the complex orbits. A detailed 3D MTF analysis is underway.

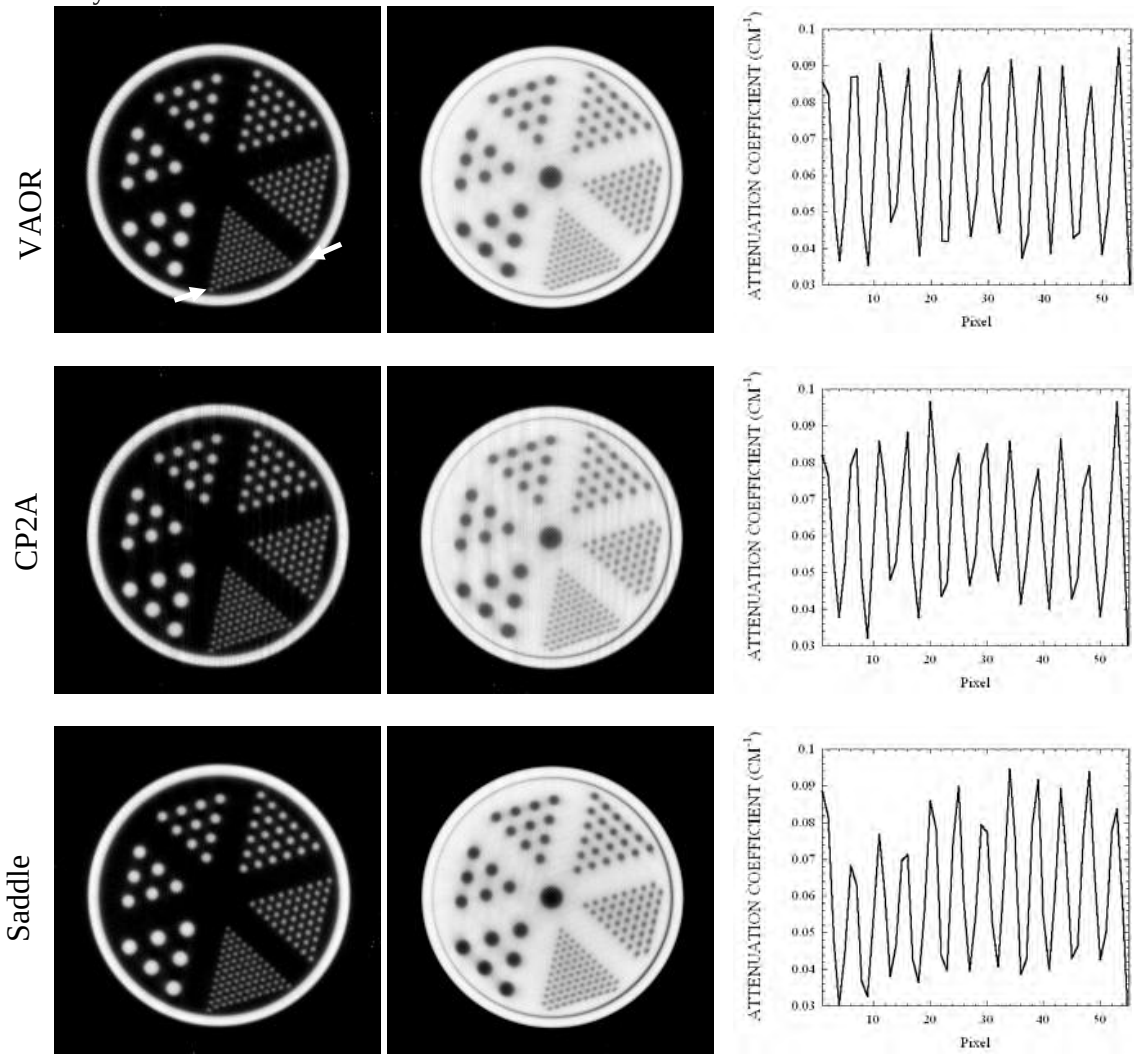

Fig. 6. Reconstructed transaxial slices through (left column) low scatter rods in air and (middle column) high scatter air columns in plastic resolution phantoms for (top) VAOR, (middle) CP2A, and (bottom) Saddle orbits. (right column) Profiles through smallest (1.1mm) rods-in-air (white arrows in upper left image) indicate position through which profiles were drawn for all orbits.

Chest Wall Proximity Imaging

Reconstructed transaxial slices through the oil/sponge filled breast phantom (Figure 7) indicate similar results for both VAOR and Saddle, although the Saddle slice qualitatively appears slightly more crisp and detailed. However, in the sagittal slices, the Saddle orbit captures significantly more volume closer to the chest wall than the VAOR orbit. It remains to be seen whether there is enough sampling for useful image information in this region, but at this point the Saddle orbit shows promise in being able to get closer to the chest wall (white arrows, Figure 8).

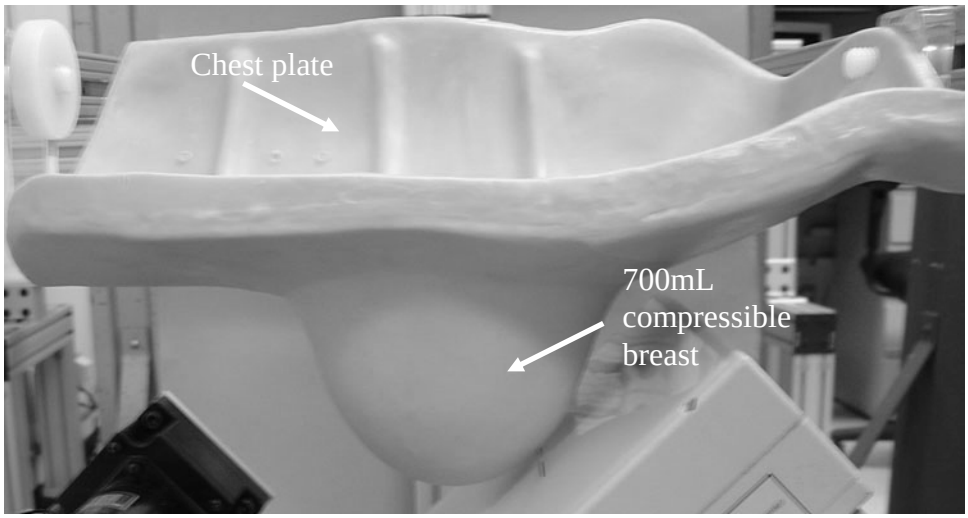

Fig. 7. Fillable 700mL compressible breast phantom filled with sponge and oil to give simulated breast structure. Note the chest plate that is used for testing chest wall proximity imaging capability as well as providing a realistic hindrance when imaging the breast pendant beneath it.

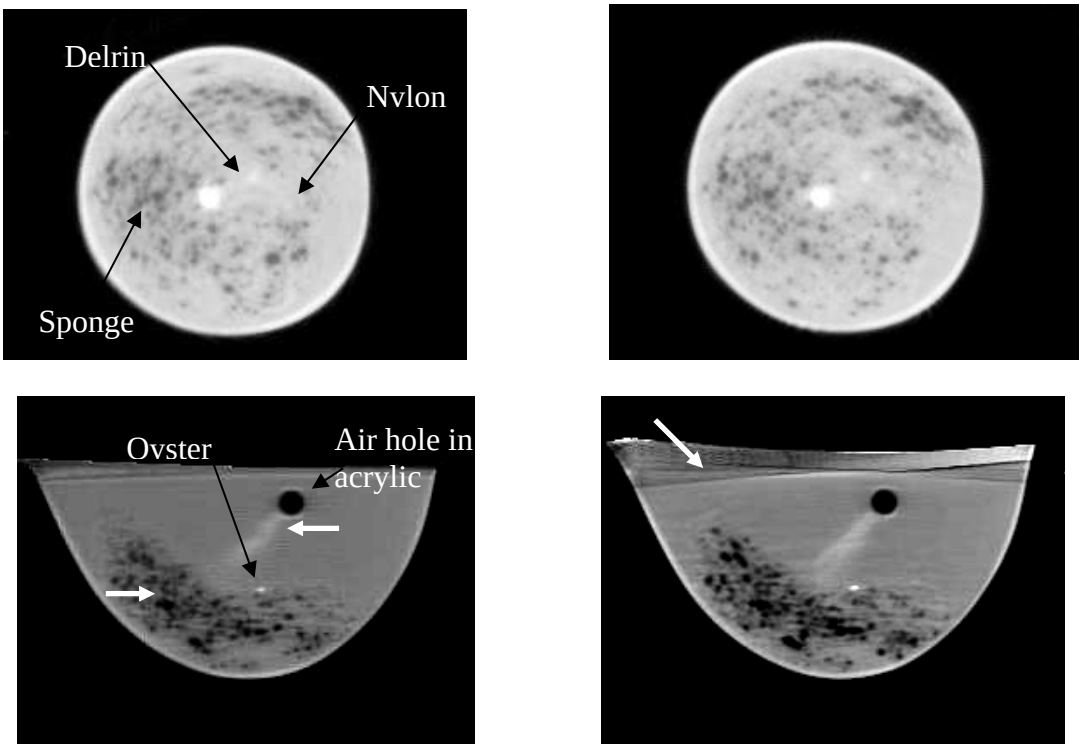

Fig. 8. Reconstructed oil/sponge breast phantom transaxial (top) and sagittal (bottom) slices for (left) VAOR, and (right) Saddle orbits. White arrows (bottom left) indicate level of transaxial slice. White arrows (bottom right) indicate area of additional sampling closer to chest plate.

Conclusions

Complex 3D cone-beam orbit acquisitions can be effectively implemented on a novel dedicated transmission computed mammotomography (CmT) system to image pendant, uncompressed breasts. Simple circular acquisitions fail to meet Tuy's data sufficiency condition, thus resulting in (severe) object distortion and image artifacts. One complex orbit investigated in this work (Saddle) effectively overcomes that distortion and significantly reduces artifacts. Results from rods-in-air and air-rods-in-acrylic indicate that resolution is not negatively affected by use of complex acquisitions. Therefore, our developed system appears to be able to perform complex acquisitions within an infinite number of possible orbits in a banded region about the sampling sphere that will aid in satisfying Tuy's sampling condition without degradation of resolution.

Breast phantom results indicate that the 3D tilt capability of our system can produce complex orbits that can be used to image closer to the chest wall in dedicated breast imaging, thereby reducing limitations encountered by patient contours and tube/detector "dead" zones.

Future work will include detailed 3D MTF measurements to confirm resolution effects, design of a patient bed to reduce geometrical limitations of the patient in acquiring complete samples close to the chest wall, optimization of complex orbits to fit the patient bed specially designed for dedicated breast mammotomography, and measurement of figures of merit including SNR and dose efficiency for various configurations to develop optimal scanning techniques for use in planned patient scans.

ACKNOWLEDGEMENTS

This work is supported by NIH Grant R01-CA96821. The authors thank Dr. James Bowsher for use of the OSTR reconstruction code used in this work.

REFERENCES

[1] J.M. Boone, T.R. Nelson, K.K. Lindfors, J.A. Siebert, "Dedicated breast CT: radiation dose and image quality evaluation," *Radiology*, **221**:657-667, 2001.

[2] B. Chen, R. Ning, "Cone-beam volume CT mammographic imaging: feasibility study," *Med. Phys.*, **29**(5):755-770, 2002.

[3] A.A. Vedula, S.J. Glick, X. Gong, "Computer simulation of CT mammography using a flat-panel imager," *Proc. of SPIE Med. Imag. 2003*, **5030**:349-360, 2003.

[4] M.P. Tornai, J.E. Bowsher, C.N. Archer, *et al*., "A compact dedicated device for dual modality radionuclide imaging of the breast with an Application Specific Emission and Transmission Tomograph (ASETT)," *Radiology*, **221P**:555, 2001.

[5] M.P. Tornai, J.E. Bowsher, C.N. Archer, R.J. Jaszczak, "Feasibility of Application Specific Emission and Transmission Tomography (ASETT) of the breast," *J. Nucl. Med.*, **43**(5):12P, 2002.

[6] M.P. Tornai, J.E. Bowsher, C.N. Archer, *et al*., "A 3D gantry single photon emission tomograph with hemispherical coverage for dedicated breast imaging," *Nucl. Instr. Meth.*, **A497**(1):157-167, 2003.

[7] M.L. Bradshaw, R.L. McKinley, E. Samei, C.N. Archer, M.P. Tornai, "Initial x-ray design considerations for Application Specific Emission and Transmission Tomography (ASETT) of the breast," *J. Nucl. Med.*, **44**(5):287P, 2003.

[8] R.L. McKinley, M.P. Tornai, E. Samei, M.L. Bradshaw, "Optimizing beam quality for x-ray computed mammotomography (CmT)," *Proc. SPIE: Physics of Medical Imaging*, **5030**(2):575-584, 2003.

[9] R.L. McKinley, M.P. Tornai, E. Samei, M.L. Bradshaw, "Simulation study of a quasi-monochromatic beam for x-ray computed mammotomography," *Med. Phys.*, **31**(4):800-813, 2004.

[10] M.P. Tornai, C.N. Archer, J.E. Bowsher, R.L. McKinley, R.J. Jaszczak, "Transmission imaging with a compact gamma camera: initial results for mammotomography," *IEEE Nucl. Sci. Symp. and Med. Imag. Conf. Rec.*, **3**:1597-1601, 2002.

[11] R.L. McKinley, M.P. Tornai, E. Samei, M.L. Bradshaw, “Initial study of quasi-monochromatic beam performance for x-ray computed mammotomography,” Presented at *IEEE Nucl. Sci. Symp. And Med. Imag. Conf.*, Portland, Oregon, October 19-26, 2003 and submitted to *Trans. Nucl. Sci.*
[12] RL McKinley, E Samei, MP Tornai, C Floyd, “Measurements of a quasi-monochromatic beam for x-ray computed mammotomography,” *Proc. of SPIE Medical Imaging 2004:Physics of Medical Imaging (In Press)* 2004.
[13] MP Tornai, RL McKinley, E Samei, C Floyd, ML Bradshaw, “Measured image quality using a quasi monochromatic for mammotomography given various uncompressed breast and lesion configurations,” Presented at *IWDM*, Chapel Hill, NC,18-21 Jun. 2004.
[14] RL McKinley, MP Tornai, E Samei, JE Bowsher, “Quasi-monochromatic beam measurements for dedicated cone-beam mammotomography of an uncompressed breast,” Presented at *IWDM*, Chapel Hill, NC,18-21 Jun. 2004.
[15] R.L. McKinley, M.P. Tornai, C.N. Brzymialkiewicz, E. Samei, J.E. Bowsher, “Analysis of a novel offset cone-beam computed mammotomography imaging system for attenuation correction of SPECT in a proposed dual modality dedicated breast mammotomography system,” Presented at *2004 Workshop on the Nuclear Radiology of the Breast*, Rome Italy, Oct 22-23, 2004 and submitted to *Physica Medica*.
[16] H.K. Tuy, “An inversion formula for cone-beam reconstruction,” *SIAM J. Appl. Math.*, **43**:546-552, 1983.
[17] X. Wang, R. Ning, “A cone-beam reconstruction algorithm for circle-plus-arc data-acquisition geometry,” *IEEE Trans. Med. Imag.*, **18(9)**: 815-824, 1999.
[18] M.P. Tornai, S.J. Cutler, D.J. Crotty, C.N. Brzymialkiewicz, R.L. McKinley, “Anthropomorphic breast phantoms for preclinical imaging evaluation with emission or transmission imaging,” Presented at 2005 *SPIE Medical Imaging Conference*, San Diego, CA, Feb. 12-18, 2005.
[19] H. Erdogan, J.A. Fessler, “Ordered subsets algorithms for transmission tomography,” *Phys. Med. Biol.*, **44**:2835-2851, 1999.
[20] B.C. Pieper, J.E. Bowsher, M.P. Tornai, C.N. Archer, R.J. Jaszczak, "Parallel-beam tilted-head analytic SPECT reconstruction: derivation and comparison with OSEM," *IEEE Trans. Nucl. Sci.* **NS-49(5)**:2394-2400, 2002.

Appendix D

IEEE 2004 Medical Imaging Symposium Workshop on the Nuclear Radiology of the Breast – presented Rome, Italy October, 2004 and In Press, Medica Physica.

Analysis of a novel offset cone-beam computed mammotomography imaging system geometry for accommodating various breast sizes

Randolph L. McKinley[1,2], Martin P. Tornai[1,2], Caryl Brzymialkiewicz[1,2], Priti Madhav[1,2], Ehsan Samei[1,2,3], James E. Bowsher[1]

[1] *Department of Radiology, Duke University Medical Center, Durham, NC 27710*
[2] *Department of Biomedical Engineering, Duke University, Durham, NC 27710*
[3] *Department of Physics, Duke University, Durham, NC 27710*

Abstract

We evaluate a newly developed dedicated cone-beam transmission computed mammotomography (CmT) system configuration using an optimized quasi-monochromatic cone beam technique for attenuation correction of SPECT in a planned dual-modality emission and transmission system for pendant, uncompressed breasts. In this study, we perform initial CmT acquisitions using various sized breast phantoms to evaluate an offset cone-beam geometry. This offset geometry provides conjugate projections through a full 360 degree gantry rotation, and thus yields a greatly increased effective field of view, allowing a much wider range of breast sizes to be imaged without truncation in reconstructed images. Using a tungsten x-ray tube and digital flat-panel X-ray detector in a compact geometry, we obtained initial CmT scans without shift and with the offset geometry, using geometrical frequency/resolution phantoms and two different sizes of breast phantoms. Acquired data were reconstructed using an ordered subsets transmission iterative algorithm. Projection images indicate that the larger, 20 cm wide, breast requires use of a half-cone-beam offset scan to eliminate truncation artifacts. Reconstructed image results illustrate elimination of truncation artifacts, and that the novel quasi-monochromatic beam yields reduced beam hardening. The offset geometry CmT system can indeed potentially be used for structural imaging and accurate attenuation correction for the functional dedicated breast SPECT system.

Introduction

We evaluate a newly developed, dedicated cone-beam transmission computed mammotomography (CmT) system configuration for attenuation correction of dedicated single photon emission computed tomography (SPECT) in a planned dual-modality system for pendant, uncompressed breast imaging. Our previous work has shown that a quasi-monochromatic beam can be produced using heavy K-edge filtration to provide optimal dose efficiency for fully three-dimensional imaging of the pendant uncompressed breast [1-4]. The hybrid Application Specific Emission and Transmission Tomography (ASETT) system [5-8] will ultimately incorporate a SPECT emission system for functional imaging along with the CmT system for structural imaging, as well as for attenuation correction of SPECT data. Therefore, it is desired to have accurately reconstructed attenuation coefficients using the previously described optimized beam technique [4].

The requirement of our compact system design indicates potential limitations in imaging uncompressed breasts with diameters larger than ~15 cm (considering the air gap and magnification needed for scatter reduction) (Figure 1). In this study, we perform initial CmT acquisitions using relatively small and large breast phantoms to evaluate the requirement for an offset or half-cone beam geometry. This geometry could allow the cone beam to be offset such that it images just over half the pendant breast at each projection, with conjugate projections acquired through a full 360 degree rotation of the gantry (Figure 2). This is a well tested technique for fan beam transmission imaging [9] that could allow a variable field of view (FOV) scanner and offer a much wider range of breast sizes to be imaged without truncation in the reconstructions. There will ultimately

be no scan time penalty because, in the dual mode system using SPECT, scans will already be performed for a full 360 degrees to optimize uniform emission spatial resolution and sampling throughout the breast. There may also be added benefits to using this half-cone beam approach including overall scatter reduction. The specific objectives of this study are to: (1) overcome the maximum uncompressed breast size limitation by implementing an offset central ray design; (2) determine the impact on the elimination of truncation artifacts for very large breasts which are intentionally only partially in the field of view of a centered geometry; (3) determine the impact on the accuracy of attenuation coefficient reconstruction; and (4) determine the impact on beam hardening while utilizing a nearly optimized quasi-monochromatic beam.

Materials and Methods

The prototype CmT system consists of a tungsten X-ray tube (Rad-94, *Varian Medical Systems*, Salt Lake City, UT) and flat-panel digital X-ray detector (Paxscan 2520, *Varian Medical Systems*, Salt Lake City, UT) mounted on a rotation stage for azimuthal motion and goniometer (RV350CC and BGM200PE, respectively, *Newport Corp*., Irvine, CA) for polar motion (Figure 1). The detector contains 1920x1536 pixels with 127 micron pixel pitch. With a source-to-image distance (SID) of 55 cm, a source-to-center-of-object or source-to-center-of-rotation distance of 35 cm, and center-of-rotation to detector distance of 20 cm, we obtain CmT scans at a tube potential of 60 kVp using 0.05 cm Ce filtration; this yields a X-ray beam with a mean energy of 36.4 keV and ~20% full width at tenth maximum.

Two geometric mini-rod phantoms (*Data Spectrum Corp*., Hillsborough, NC) and two anthropomorphic breast phantoms (*Radiology Support Devices*, Newport Beach, CA) were initially scanned. The rod phantoms were each 7 cm diameter cylinders: the first

contained multiple sectors of acrylic rods suspended in air, each 1.1, 1.5, 2.3, 3.1, 3.9, and 4.7 mm in diameter spaced on twice their diameters; the second was a large cylinder of acrylic with tubes (i.e. drilled holes) positioned, grouped and sized exactly like the described rods in air. The smaller breast phantom's dimensions were 11.8 cm medial-to-lateral, 12 cm superior-to-inferior, and 3.8 cm nipple-to-chest with a fillable volume of 240 mL. The large breast phantom's dimensions were 15 cm medial-to-lateral, 20 cm superior-to-inferior, and 7.4 cm nipple-to-chest with a 935 mL fillable breast volume. The breasts contained a machined 8 mm inner diameter, acrylic walled, "air" lesion (*Data Spectrum*) suspended on an acrylic rod with an ~1 mm diameter "air" neck abutted to an ~2 mm diameter "air" neck; this is normally used as a liquid fillable lesion for nuclear emission imaging. An exposure of 4 mAs was used for the rods and small breast phantom, and 10 mAs for the large breast phantom in order to maintain nearly equal detector pixel values for the different breast sizes.

Two scans were performed for each set of phantoms: one with the central ray of the cone beam intersecting the axis of rotation (Figure 2a), and one with the central ray offset 5 cm laterally from the axis of rotation (Figure 2b). Data were acquired over 360º in 1.5º increments using a vertical axis of rotation and using the full, intrinsic detector resolution (i.e. no binning). Acquired data were reconstructed using an ordered subsets transmission iterative algorithm [10]. Reconstructions were performed on 8x8 pixel binned image data (totaling a 1.016 mm voxel size) using 8 subsets, 15 iterations, and images are displayed with additional smoothing performed by summing 3 axial slices, having 1-2-1 weighting.

Quantitative comparisons were also made. Beam hardening was calculated from:

$$Beam\ Hardening = \frac{\mu_{edgeROI} - \mu_{centerROI}}{\mu_{centerROI}} * 100\%$$

where $\mu_{edgeROI}$ and $\mu_{centerROI}$ are the mean attenuation coefficients for regions-of-interest (ROIs) located at the edge and center of the reconstructed axial slice. This figure of merit for tomography was determined to be a good surrogate predictor of beam hardening from previous projection measurements and simulations [1,2]. Note that scatter can have a significant impact in the evaluation of attenuation coefficients; indeed, scatter can be expected to decrease the measured coefficient values, and hence, we expect that this beam hardening metric represents an upper bound on the expected amount of beam hardening. Incomplete sampling and truncation of the reconstruction data can also degrade the measured attenuation coefficient values, causing the center and edge values to further diverge. Attenuation coefficient error was calculated as:

$$Coefficient\ Error = \frac{\mu_{edgeROI} - \mu_{theoretical}}{\mu_{theoretical}} * 100\%$$

where $\mu_{edgeROI}$ is as described above and $\mu_{theoretical}$ is the theoretical, narrow beam attenuation coefficient for water at the mean energy of the quasi-monochromatic beam determined from previous simulations (36.4 keV pre-breast) [1-4]. The value of $\mu_{theoretical}$ was determined using NIST tables and cubic spline interpolation.

Results and Discussion

Reconstructed axial slices of the low scatter resolution phantom, for both the centered and offset geometries (Figure 3), illustrate that reconstructions appear artifact free; no truncation was expected of this small diameter object with either orbit. More quantitatively, the profile obtained from the offset acquired data closely matches that of the centered profile. No noticeable distortions are observed using either geometry. In both cases, the smallest rods (1.1 mm) are discernable, even using the ~1 mm voxel binning.

Similarly, for the high scatter resolution phantom (Figure 4), both centered and offset geometries provide axial reconstructions with no truncation artifacts, and similar profiles. However, the smallest (1.1 mm) tubes are not easily resolvable. This limited resolution may be due to the increased effect of scatter in this more solid tube phantom.

Breast projection images indicate that, while the smaller breast is fully within the field of view, the larger breast is truncated to some degree (Figure 5). Projection images are also shown for the offset geometry data collection, where there is intentional truncation of larger objects.

Reconstructed results for the smaller breast phantom (Figures 6 and 7) demonstrate several points:(1) no truncation artifacts appear in the centered phantom (Figure 6) since the phantom is fully within the FOV; (2) axially oriented breast shapes are nearly identical for both centered and offset geometries; and (3) profiles through the lesions are nearly indistinguishable for both geometries. Reconstructed results for the larger breast phantom (Figures 8 and 9) demonstrate other points: (1) severe truncation artifacts occur with the centered phantom (Figure 8), since the uncompressed phantom is partially outside the FOV in the acquired projections; (2) the centered geometry breast has a severely distorted profile through the peripheral breast and centered lesion as compared with the profile from the offset geometry; (3) truncation artifacts are eliminated and more accurate breast shape obtained for the offset reconstruction (Figure 9); and (4) there is a complete removal of the truncation effect in the profile for the offset geometry. The truncation is not as apparent in the illustrated axial view (Figure 8) since the slice is taken at the level of the lesion; for axial slices closer to the chest wall, the truncation related distortion is much more clear. There is a large circular artifact appearing in the

offset reconstruction (Figure 9). This is likely due to the use of not-well-behaved pixel rows near and at the edge of the detector for the offset geometry, causing uniformity artifacts in the reconstruction (there were no in/extrinsic uniformity corrections applied to the projections prior to reconstruction). In subsequent studies, pixel row corrections and additional uniformity corrections will also be applied prior to reconstruction.

Attenuation coefficient results for the smaller breast (Table 1) indicate a beam hardening of 8.1% and 5.3%, for the centered and offset phantom, respectively. Beam hardening for the larger breast in the offset geometry was 16.9%. Beam hardening for the centered geometry was not calculated since the truncation artifacts caused a wide range of edge attenuation coefficients that a meaningful result could not be obtained. Beam hardening for a beam without our unique filtering approach has been shown to be 30-40% [3].

In terms of accuracy of absolute value of the attenuation coefficients determined at the phantom edge (where they are closest to their expected value for an unhardened beam), reconstructed coefficients were within 1.9% and 3.0% for the smaller breast with centered and offset geometries, respectively. The larger breast with offset geometry had 4.6% coefficient accuracy. For the centered geometry, the error was 7.2% at its best (i.e. farthest away from an area with truncation artifacts) and up to 62.6% within the area with large truncation artifacts. Images made using attenuation coefficients having this accuracy allow the possibility for absolute differentiation of tissues *in vivo*, based on their intrinsic attenuation values, rather than merely a gray scale difference generally used to distinguish tissues; this could lead to direct *in vivo* tissue characterization with X-ray computed tomography. Having a better than 5% accuracy of measured attenuation

coefficients will also facilitate scaling attenuation values to the higher energies (140 keV) required for attenuation correction of reconstructed SPECT images.

Conclusions

Computed mammotomography results from phantom measurements and reconstructed images indicate that an offset cone beam geometry can be useful in allowing a much wider range of breast sizes to be imaged without truncation artifacts and other distortions due to the offset geometry, while maintaining accurate determination of attenuation coefficients. The largest breast size accommodated by our compact system can be nearly doubled with the offset cone beam geometry. As such, this geometry could be used to provide fine structural imaging and accurate attenuation correction for image analysis alone, and also for use with our functional dedicated breast SPECT system.

ACKNOWLEDGEMENTS

This work is supported by NIH Grant R01-CA96821.

REFERENCES

[1] R.L. McKinley, M.P. Tornai, E. Samei, M.L. Bradshaw, "Initial study of quasi-monochromatic beam performance for x-ray computed mammotomography," *2003 IEEE Conference Record NSS/MIC*, **4**:2999-3003, and submitted to *IEEE Trans. Nucl. Sci*. (In Revision).

[2] R.L. McKinley, M.P. Tornai, E. Samei, M.L. Bradshaw, "Optimizing Beam Quality for X-ray Computed Mammotomography (CmT)," *Proc. SPIE: Physics of Medical Imaging*, **5030**(2):575-584. 2003.

[3] R.L. McKinley, M.P. Tornai, E. Samei, M.L. Bradshaw, "Simulation study of a quasi-monochromatic beam for x-ray computed mammotomography," *Med. Phys.*, **31**(4):800-813, 2004.

[4] R.L. McKinley, E. Samei, C.N. Brzymialkiewicz, M.P. Tornai, C.E. Floyd, "Measurements of an Optimized Beam for X-ray Computed Mammotomography," *Proc. SPIE: Physics of Medical Imaging*, **5368**(1): 311-319, 2004.

[5] M.P. Tornai, J.E. Bowsher, C.N. Archer, *et al*, " A Compact Dedicated Device for Dual Modality Radionuclide Imaging of the Breast with an Application Specific Emission and Transmission Tomograph (ASETT)," *Radiology*, **221P**:555. 2001.

[6] M.P. Tornai, J.E. Bowsher, C.N. Archer, R.J. Jaszczak, "Feasibility of Application Specific Emission and Transmission Tomography (ASETT) of the Breast," *J. Nucl. Med.* **43**(5):12P. 2002.

[7] M.P. Tornai, J.E. Bowsher, C.N. Archer, *et al*., "A 3D Gantry Single Photon Emission Tomograph with Hemispherical Coverage for Dedicated Breast Imaging," *Nucl. Instr. Meth.* **A497**(1):157-167. 2003.

[8] M.L. Bradshaw, R.L. McKinley, E. Samei, C.N. Archer, M.P. Tornai, "Initial X-ray Design Considerations for Application Specific Emission and Transmission Tomography (ASETT) of the Breast." *J. Nucl. Med.* **44**(5):287P. 2003.

[9] M.P. Tornai, R.J. Jaszczak, *D.R.* Gilland, R.E. Coleman, Y. Ooie, M. Taguchi, G. Enos, "Investigation of large field-of-view transmission imaging for SPECT attenuation compensation with Gd-153, Tc-99m and Ce-139 sources," *IEEE Trans. Nucl. Sci.*, 47(3): 1182 - 1191 , 2000.

[10] H. Erdogan, J.Aa Fessler. "Ordered subsets algorithms for transmission tomography." *Phys. Med. Biol*., **44**(11):2835-51, 1999.

TABLE 1. Attenuation coefficient results for small and large breasts, centered and offset geometries. Theoretical water attenuation coefficient was determined from mean energy (36.4 keV) of simulated spectra, using cubic spline interpolated NIST data.

	Measured μ center	Measured μ edge	Theoretical μ	Beam Hardening	Coefficient Error
Central Small Breast	0.2515	0.2737	0.2789	8.1%	1.9%
Offset Small Breast	0.2561	0.2706	0.2789	5.3%	3.0%
Central Large Breast	0.2042	0.1043-0.2590	0.2789	NA	7.2-62.6%
Offset Large Breast	0.2214	0.2663	0.2789	16.9%	4.6%

FIGURE CAPTIONS:

FIGURE 1. Experimental setup with (from L to R), W-target X-ray source, custom 4-jaw collimator, prone suspended torso phantom containing realistic radiographic features and “pendant” breast, and digital X-ray detector mounted on a goniometer providing polar tilt. This system is further mounted on an azimuthal rotation stage.

FIGURE 2. (a) Schematic illustrating truncation with 55 cm SID for views about a 17 cm diameter breast at 20 cm object-center-to-image distance. Imaging width shown is 20cm with digital detector in “portrait” format; “landscape” format would give only a few extra cm increase in width, but then would have small depth along nipple-to-chest axis. Actual breast phantoms have 3D asymmetries instead of the regular shape illustrated here. (b) Schematic illustrating advantage of offset half-cone beam for large breasts. SID=source-to-image distance, SOD = source-to-object center distance, COR = center-of-rotation.

FIGURE 3. Low scatter resolution phantom reconstruction for (a) Centered geometry and (c) Offset geometry. Axial slices (3 summed slices) are shown along with associated profiles (b,d, respectively) through 2.3 and 3.9 mm rods.

FIGURE 4. High scatter resolution phantom reconstruction for (a) Centered geometry and (c) Offset geometry. Axial slices (3 summed slices) are shown along with associated profiles (b,d, respectively) through 2.3 and 3.9 mm rods.

FIGURE 5. (a) Projection image of smallest breast phantom (0.24 L) fully within field of view and (b) Larger breast phantom (0.94 L) partially outside the field of view. (c) Smallest breast phantom (0.24 L) projection with offset geometry, and (d) Larger breast phantom (0.94 L) projection with offset geometry.

FIGURE 6. (a) Small breast (0.24 L) phantom axial slice (3 summed slices), at the level of the lesion, with centered geometry, and (b) associated profile through 0.8 mm air-filled lesion in axial slice for centered geometry. (c) Sagittal slice and (d) Coronal slice through small breast phantom.

FIGURE 7. (a) Small breast phantom axial slice, at the level of the lesion, with offset geometry, and (b) associated profile through the lesion for offset geometry. (c) Sagittal slice and (d) Coronal slice through small breast phantom.

FIGURE 8. (a) Large breast (0.94 L) phantom axial slice (3 summed slices), at the level of the lesion, with centered geometry, and (b) associated profile through 0.8 mm air-filled lesion in axial slice for centered geometry. (c) Sagittal slice and (d) Coronal slice through large breast phantom.

FIGURE 9. (a) Large breast phantom axial slice, at the level of the lesion, with offset geometry, and (b) associated profile through lesion for offset geometry. (c) Sagittal slice and (d) Coronal slice through large breast phantom.

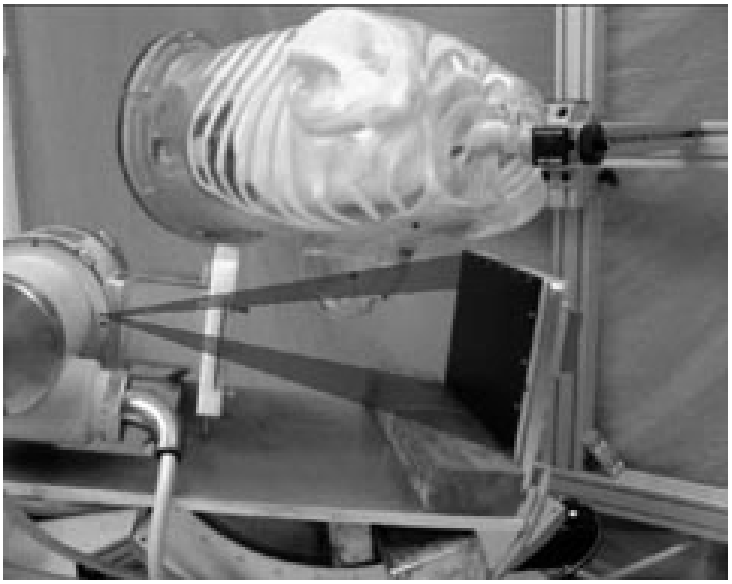

FIG. 1.

Figure 1. McKinley, et al.

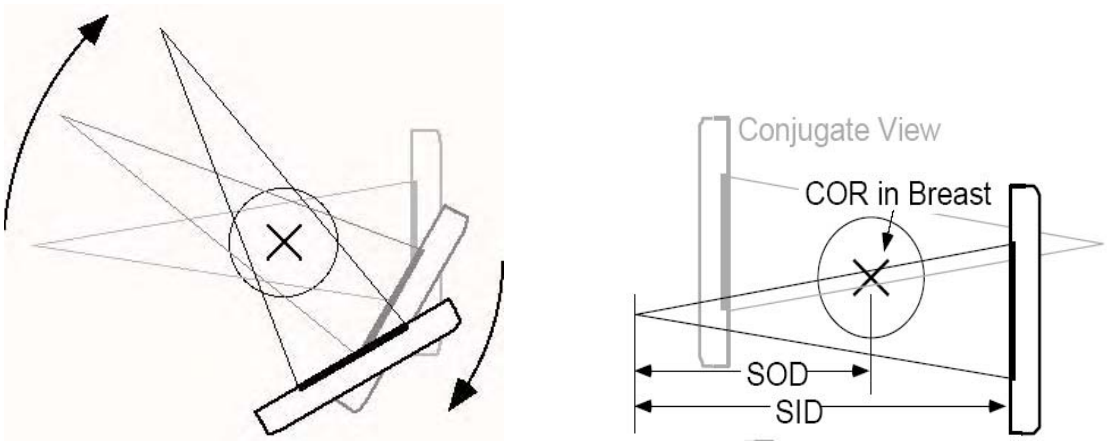

(a) (b)

FIG. 2.

Figure 2, McKinley, et al.

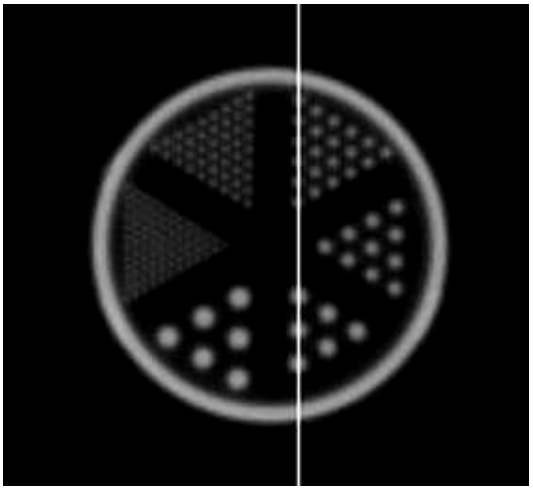

(a)

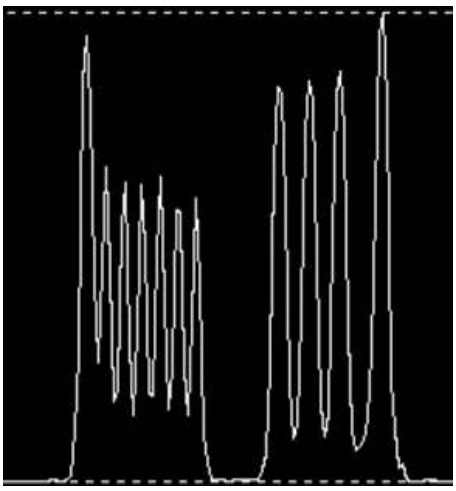

(b)

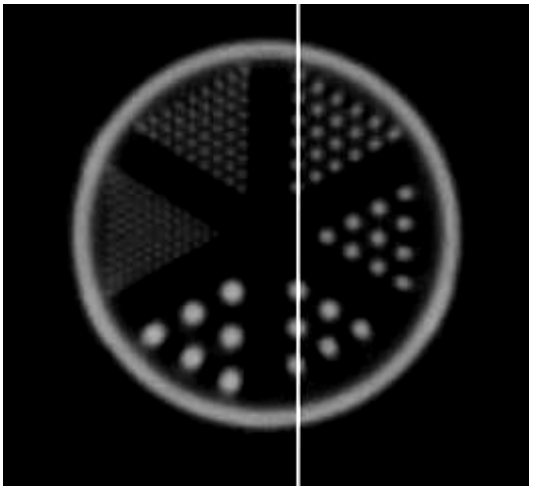

(c)

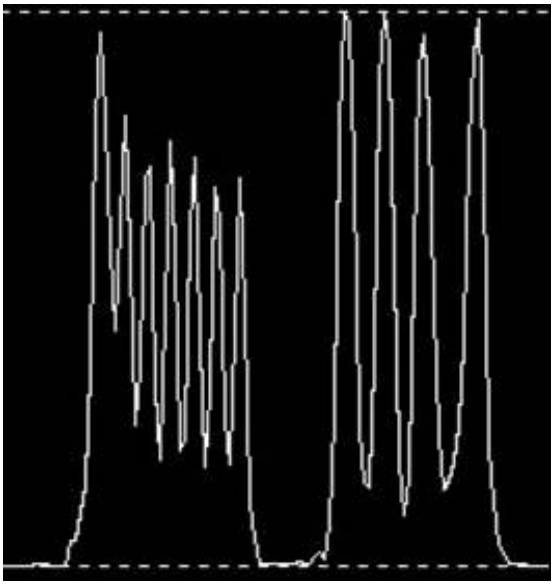

(d)

FIG. 3.

Figure 3, McKinley, et al.

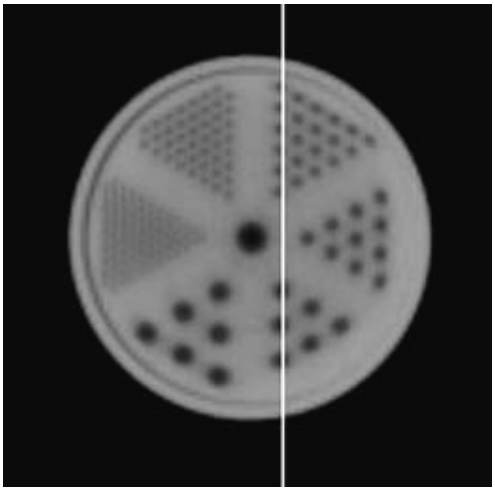

(a)

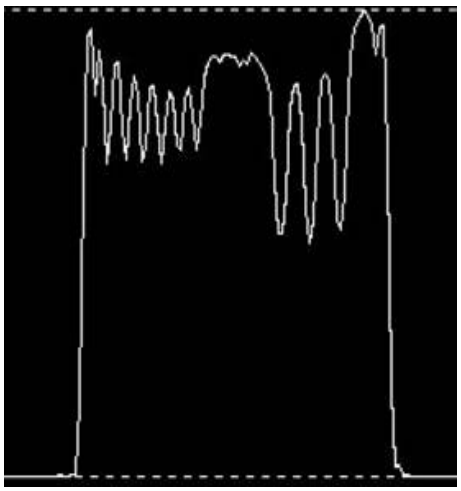

(b)

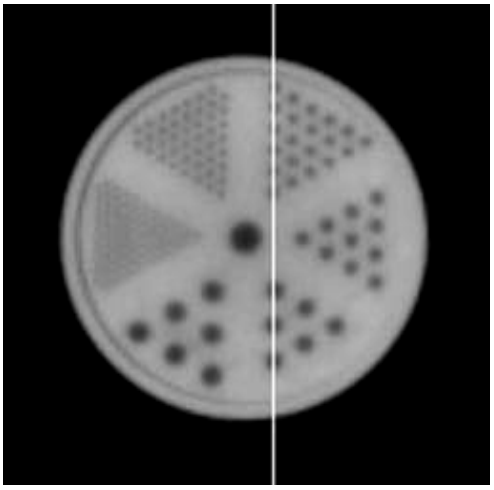

(c)

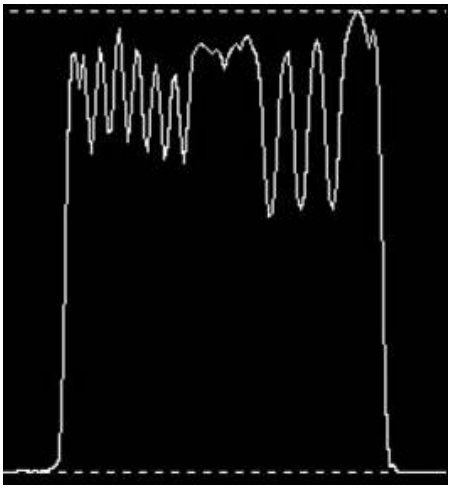

(d)

FIG. 4.

Figure 4, McKinley, et al.

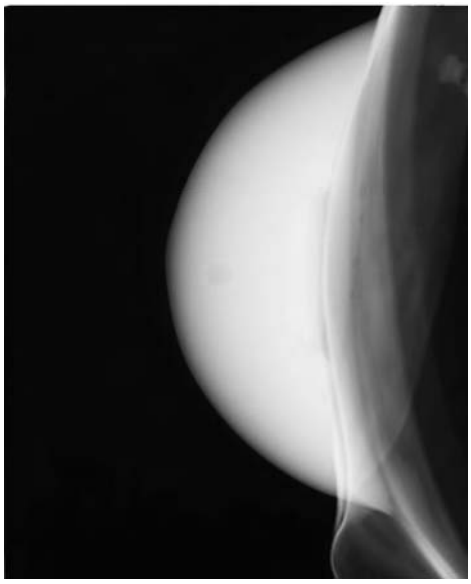

(a)

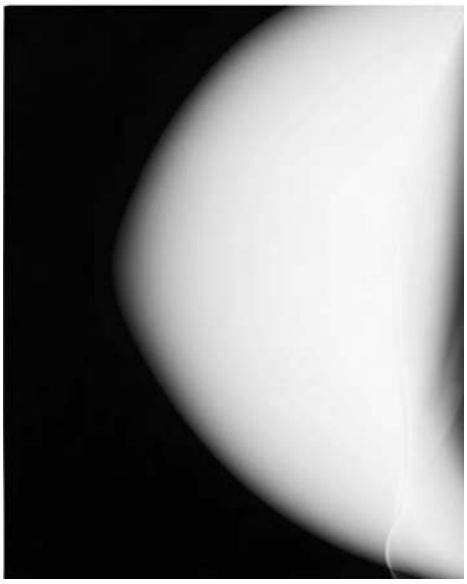

(b)

(c)

(d)

FIG. 5.

Figure 5, McKinley, et al.

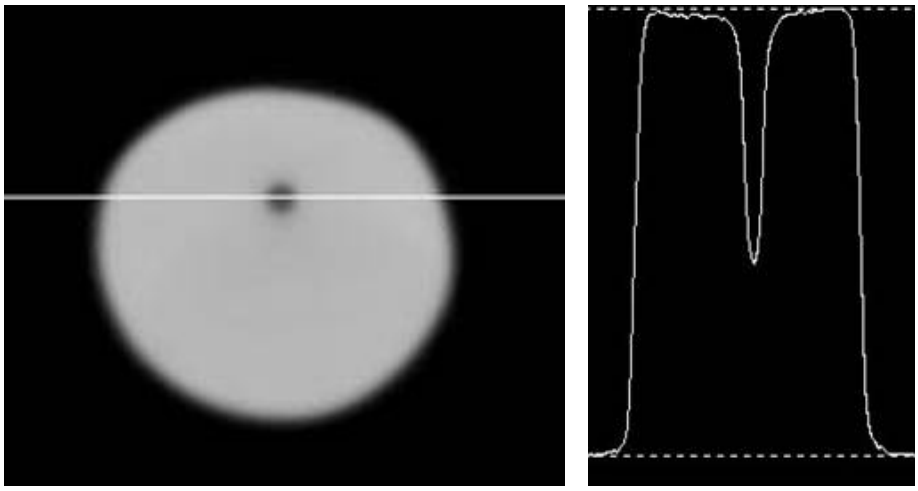

(a) (b)

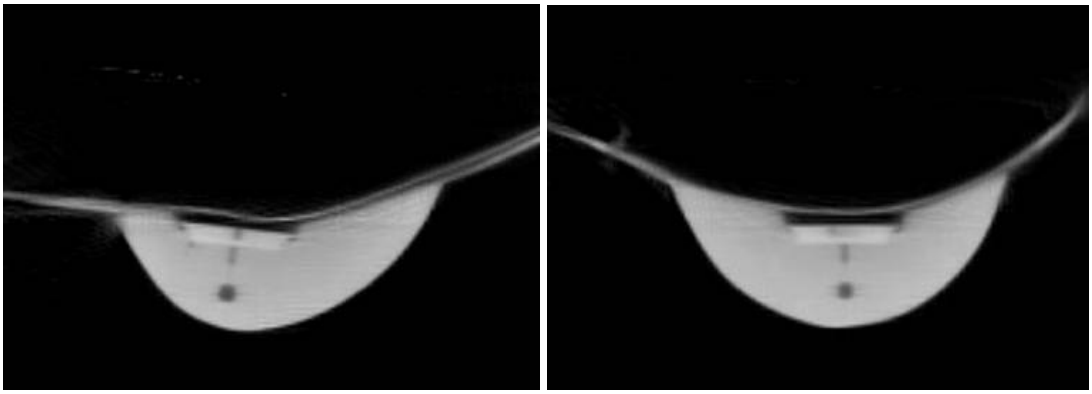

(c) (d)

FIG. 6.

Figure 6, McKinley, et al.

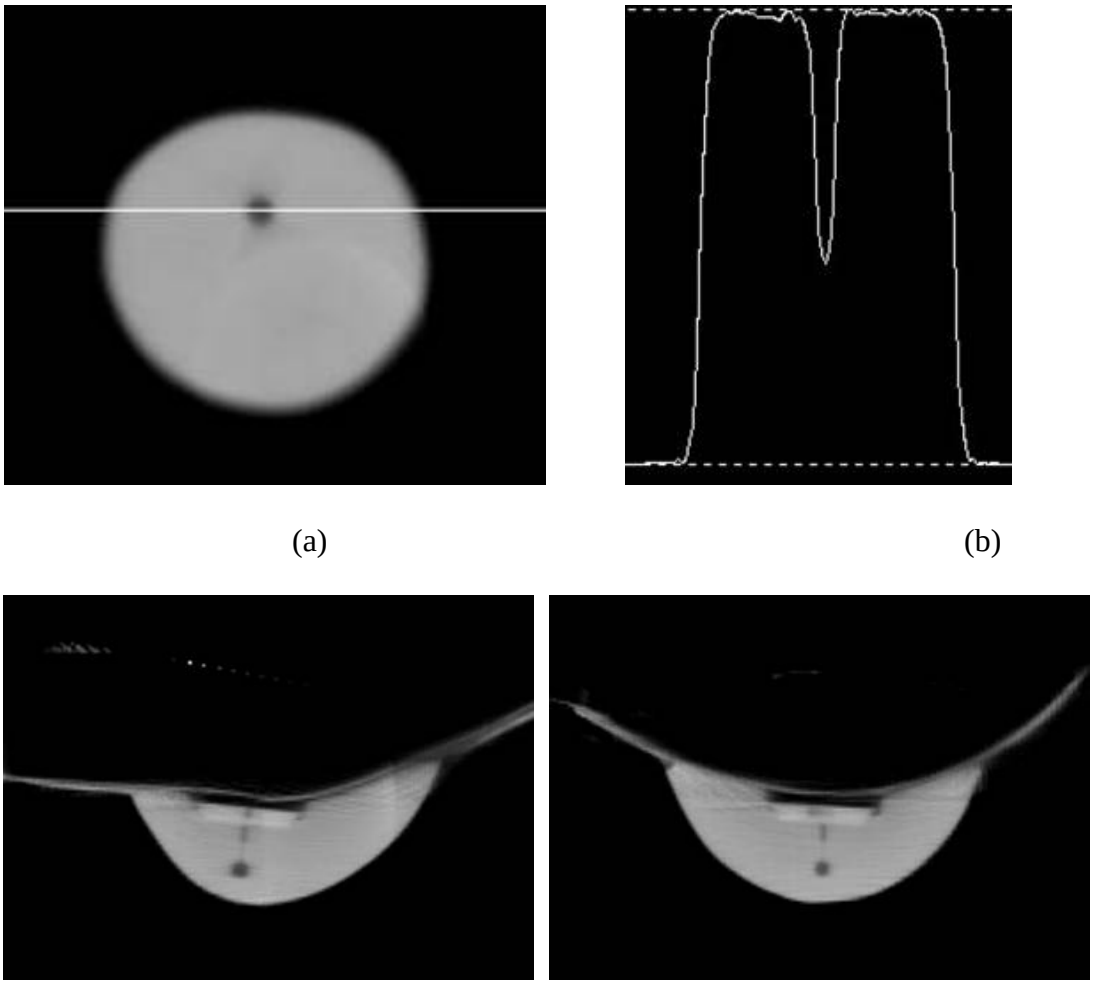

FIG. 7.

Figure 7, McKinley, et al.

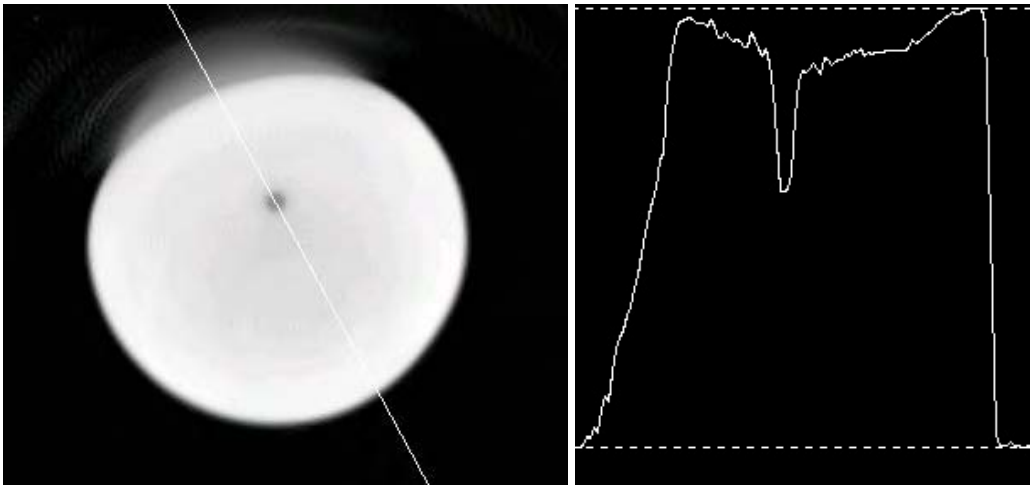

(a) (b)

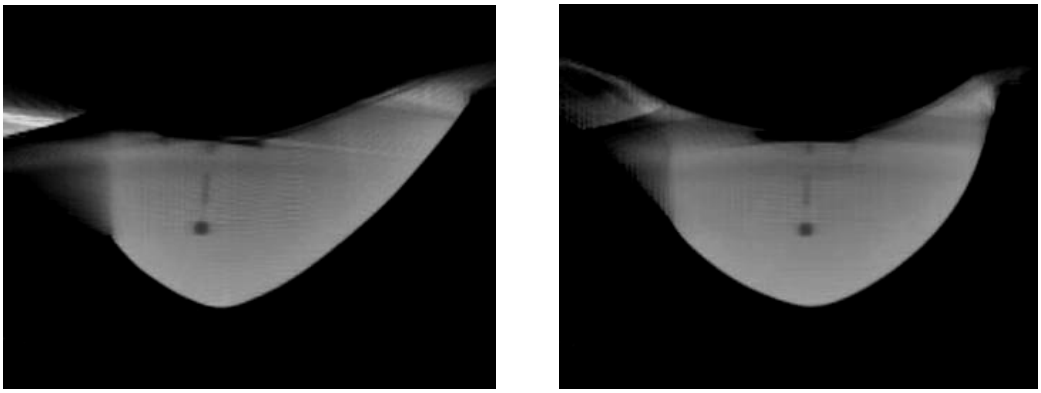

(c) (d)

FIG. 8.

Figure 8, McKinley, et al.

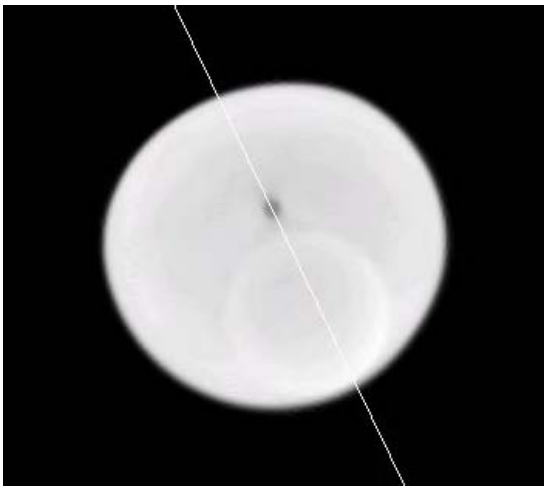

(a)

(b)

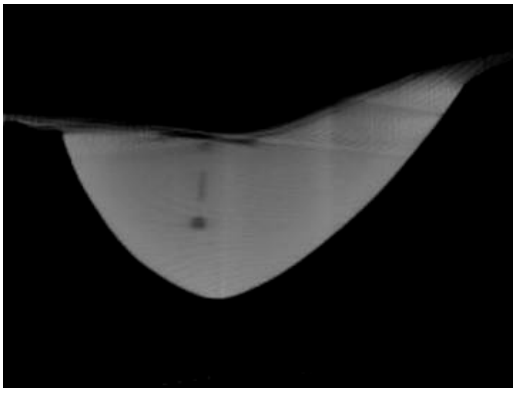

(c)

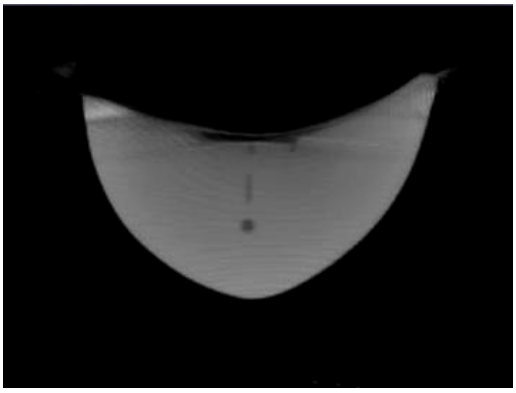

(d)

FIG. 9.

Figure 9, McKinley, et al.

Appendix E

SPIE 2006 Medical Imaging Conference Record

Preliminary Investigation of Dose for a Dedicated Mammotomography System

Randolph L. McKinley[1,2], Martin P. Tornai[1,2]

[1] Department of Radiology, Duke University Medical Center, Durham, NC
[2] Department of Biomedical Engineering, Duke University, Durham, NC

ABSTRACT

We use a previously reported, optimized quasi-monochromatic beam technique together with unique complex acquisition trajectories made possible with a novel, dedicated cone-beam transmission computed mammotomography (CmT) system to investigate effects of low dose imaging of pendant, uncompressed breasts. Investigators have used a guideline of dose for CmT type applications as that used for dual-view mammography (4-6 mGy for average breast size). This dose is somewhat arbitrary, and it may be possible to reduce this significantly without sacrificing image quality using our quasi-monochromatic x-ray beam, 3D complex acquisition orbits, and iterative reconstruction techniques. A low-scatter acrylic resolution phantom in various media, a breast phantom with sponge and oil-filled lesions, and a cadaver breast are used to evaluate the effect of lowered dose on resolution and image artifacts. Complex saddle acquisition trajectories (necessary to overcome cone-beam distortion) are carried out for total exposures of 96, 300, and 600 mAs over 240 projections. These exposures relate approximately to 1/10th, 1/3rd, and 2/3rd of the standard dual view mammography dose for an average sized 50% adipose/glandular breast. Iterative reconstruction uses an OSTR algorithm with 0.125 mm^3 voxels. Image artifacts increased as dose was reduced but did not appear to greatly degrade image quality except at the lowest contrast tested (1% absolute contrast). As expected, noise increased as dose was reduced. However, this did not appear to affect resolution for rods in air (high contrast), nor rods in oil (20% absolute contrast). Resolution was reduced for rods in water (1% absolute contrast) due to increased prevalence of image artifacts as well as increased noise. Breast phantom imaging of soft lesions in a highly glandular breast (6% absolute contrast) clearly yielded the 60uL and all larger volume lesions. Preliminary biological breast tissue results illustrate excellent subjective image quality at all dose levels tested. Results indicate that our quasi-monochromatic beam together with complex orbit capability and iterative reconstruction has the potential to provide sufficient image quality for practical 3D mammotomography of uncompressed breasts at significantly lower dose than dual view mammography. This is nominally a 2-fold improvement over other approaches using circular orbits and broader spectral x-ray beams. While simple image filtering (post-reconstruction smoothing) could improve noise quality, improvements in image artifact correction and scatter correction are required to more accurately determine the lower limits on dose. A contrast-detail study is also warranted with a greater variety of lesion sizes and contrasts.

Keywords: X-ray computed mammotomography, quasi-monochromatic, orbits, trajectory, iterative reconstruction uncompressed breast imaging, cone-beam, CT, dose.

INTRODUCTION

Current breast imaging techniques have high false-positive and false-negative rates for breast lesion malignancy. Various modalities have been applied in unique ways in an attempt to improve diagnosis. Some groups are investigating dedicated x-ray cone-beam tomography alone.[1-3] Our group has proposed dual-modality computed mammotomography (CmT) along with tomographic emission imaging.[4,5] Our CmT system (Figure 9) will ultimately be incorporated with emission imaging in an attempt to improve breast lesion detection over current dual view X-ray mammography (XRM), particularly in women with radiographically dense breasts.[4-14] The CmT system could also be used in a stand-alone mode for structural mammotomographic imaging, utilizing the unique offset cone beam geometry to image a wide range of breast sizes.[15]

CmT is a non-standardized technique and, as such, no guidelines have been established for appropriate technique and dose to patients. Given that this is a tomographic technique taking hundreds of exposures for an acquisition, dose is of primary concern. Various investigators have used a guideline of dose for CmT at that used for dual-view mammography (4-6 mGy for average-sized 50/50 adipose/glandular breast).[16,17] Though the rationale may be that a new ionizing radiation imaging modality should not in principle have greater dose than is currently allowed for screening, this dose limit is somewhat arbitrary, and it may be possible to reduce this significantly without sacrificing image quality. It may particularly be possible using our previously reported quasi-monochromatic beam technique,[8-11,18,19] coupled with complex acquisition orbits which more completely sample the breast volume of interest,[15,20] and iterative reconstruction techniques which model the statistics of the data acquisition process. This dose minimization potential needs to be investigated prior to initiating patient studies to ensure full optimization of our unique components.

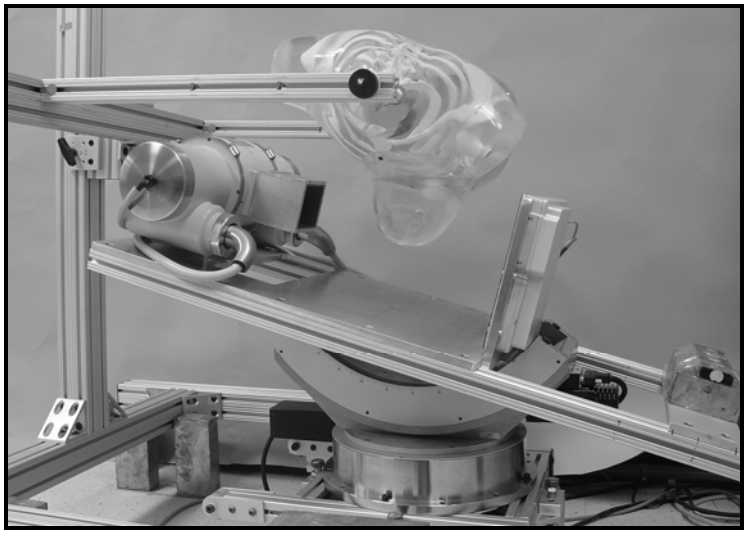

Figure 9. Photograph of prototype computed mammotomography system composed of (left) *Varian* Rad-94 x-ray tube, (right) *Varian* Paxscan 2520 digital detector, (bottom) *Newport* goniometer and rotation stages for azimuthal and polar motion, facilitating the ability to perform arbitrary and complex 3D system orbits. Setup is also shown with a suspended torso and attached 1060mL breast phantom.

MATERIALS AND METHODS

CmT Apparatus Description and Experimental Techniques

We use a Ce (Z=58, ρ=6.89g/cm^3, K-edge=40.44keV) (*Santoku America, Inc.*, Tolleson, AZ) 100th value attenuating layer thick filter (t=0.057cm) to produce a quasi-monochromatic beam with mean energy (36.4 keV) within the peak dose efficiency energy range for uncompressed breast imaging (30-40 keV).[10,13,19] It is inserted into a custom built collimator attached to a tungsten-target X-ray tube (model Rad-94, 0.4mm focal size, 14º anode angle, *Varian Medical Systems*, Salt Lake City, UT). Tube potential for all acquisitions was 60 kVp. Three exposure levels were used to acquire CmT reconstructions at three different dose levels. These total exposure levels were 96, 300, and 600 mAs evenly divided over 240 projections acquired over a 360 degree scan. The source-to-image distance (SID) used in our setup was 55cm, with a source to object center distance of 35cm. A high frequency generator provided the high voltage (model CPX160, *Electromed Inc.*, Montreal, PQ). Images were collected with a CsI(Tl) digital flat panel x-ray detector (model Paxscan 2520, 1920x1536 pixels, 600 m thick, 127 m pixel size, *Varian Medical Systems*, Salt Lake City, UT). The CmT system is mounted on a BGM200PE goniometer for polar motion and RV350CC rotation stage (*Newport Corp.*, Newport Beach, CA) for azimuthal motion (Figure 9).

Orbit

Our previously reported, optimized, quasi-monochromatic beam technique[8-11,14,19] together with a complex, 3-dimensional (3D) saddle shaped orbit (Figure 10) made possible with the novel CmT gantry[5,15] was used to acquire all cone beam scans. Note that by utilizing our integrated rotation stage and goniometer, any arbitrary orbit is made possible with the gantry. Also note that 0º polar angle is defined as the angle at which the central ray of the cone-beam is horizontal. Negative polar angles are defined as the direction in which the detector moves higher than horizontal.

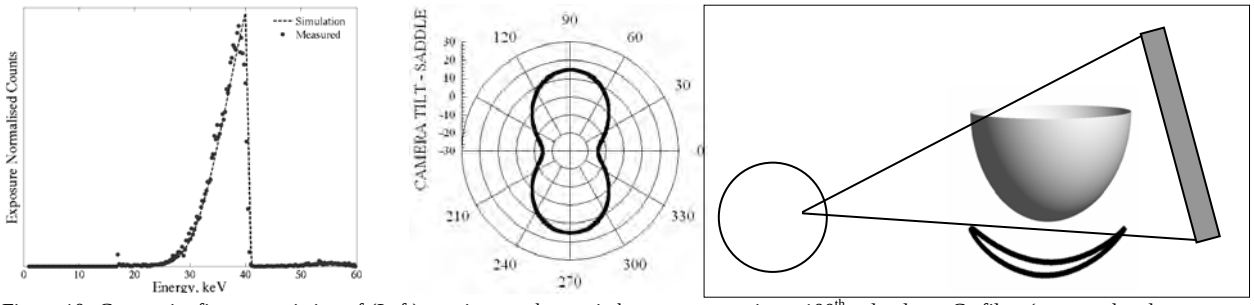

Figure 10. Composite figure consisting of (Left) quasi-monochromatic beam spectra using a 100th value layer Ce filter (measured and simulated) utilized in CmT system to optimize dose efficiency. (Middle) Polar plot of the 3D trajectory traced by the CmT system for a Saddle orbit. Azimuthal angles are indicated around the circumference of the circle, and ± polar tilt by the radius of the circle. (Right) 3D rendition of the Saddle orbit (dark curve at bottom) about an isolated, suspended breast with x-ray tube, x-ray cone beam boundary and detector indicated.

Phantoms

A 7.5cm diameter low scatter acrylic resolution phantom (model ECT/DLX-MP, with 1.1, 1.5, 2.3, 3.1, 3.9, and 4.7mm rods in air spaced on twice their diameter, *Data Spectrum Corp.*, Hillsborough, NC), was used to evaluate the effect of dose on resolution and image artifacts. The low scatter rod phantom was immersed separately in oil and water in an 8 cm diameter acrylic cylinder (Figure 11, far left), as well as within 750 mL and 975 mL breast phantoms. Data were collected at three dose levels approximately equal to 1/10th, 1/3rd, and 2/3rd that of dual view mammography. These experiments were repeated with a different 975 mL breast phantom containing: (1) ellipsoidally shaped, oil-filled balloon "lesions" within a structured background generated with a sponge[21] (Figure 11, middle left). Figure 11 (right) illustrates sizes and placement of the lesions within the phantom/sponge); and (2) a cadaver breast from a 48 year-old woman. Dose was determined using DgN_{CT} coefficients[22] and simulated spectra. A summary of experiments, dose levels, and contrasts is provided in

Table 1.

Volume (uL)	Short Axis	Long Axis

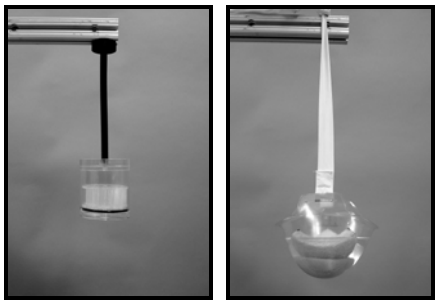

	(mm)	(mm)
500	9.6	13.4
140	5.9	11.1
60	4.2	7.9
30	3.9	6.0

Figure 11. Photos illustrating (far left) acrylic rod phantom in the acrylic cylinder, (middle left) 975 mL breast cup containing sponge material and fluid, (middle right) schematic of ellipsoidal oil-filled balloon and their (coronal) locations within the sponge material, and (far right) table of lesion dimensions. Phantoms are suspended within the central field of view of CmT system.

Table 1. Experimental summary indicating dose levels, contrasts used and their relationship to breast contrasts.

Experiment	Dose Levels (mGy)	Contrast (%)	Grossly Approximating
Acrylic rods in air	0.8, 2.4, 4.7	1227	N/A
Acrylic rods in 8cm cylinder with oil	0.8, 2.4, 4.7	~20	Lesion in fatty to 50/50 breast
Acrylic rods in 8cm cylinder with water	0.8, 2.4, 4.7	~1	Difference between benign and malignant
Acrylic rods in 975 mL breast with oil	0.6, 1.8, 3.7	~20	Lesion in fatty to 50/50 breast
Acrylic rods in 975 mL breast with water	0.6, 1.8, 3.7	~1	Difference between benign and malignant
Acrylic rods in 750 mL breast with water	0.6, 1.9, 3.9	~1	Difference between benign and malignant
Oil-filled balloons in sponge-containing breast phantom with water	0.6, 1.8, 3.7	~6	Lesion in dense breast
Cadaver breast in 950 mL breast cup	0.6, 1.8, 3.7	N/A	Biological breast tissue

Reconstructions

Image reconstructions used a modified ray-tracing based iterative ordered subsets transmission (OSTR) algorithm,[23] accounting for the 3D vantage of the source-detector pair. Gain and offset corrected projection images were binned to 4x4 pixels and reconstructed using 8 subsets, and 10 iterations, yielding a reconstructed voxel size of 0.125 mm^3. Figure 12 illustrates the rationale for stopping at the 10^{th} iteration. A plot of signal difference to noise ratio (SNR) versus contrast (signal difference to background ratio) for the 500 and 140 uL oil-filled lesions in water-sponge background for the 300 mAs technique indicate that SNR is maximized at the 10^{th} iteration. Incremental gains for contrast decrease thereafter, and as is characteristic with iterative techniques, the noise characteristics degrade with further iterations.

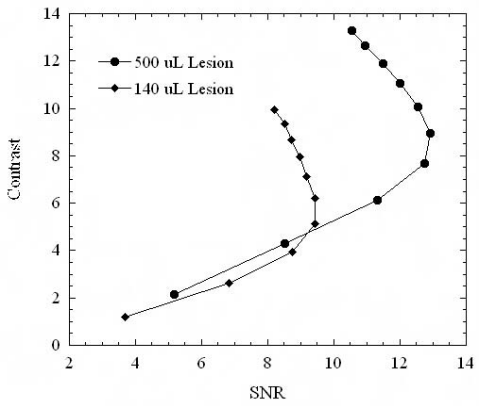

Figure 12. Plot of measured contrast versus SNR for 20 iterations (with every second iteration result plotted, starting in lower left). SNR is maximized at 10th iteration for both the 500 uL and 140 uL oil-filled balloon lesions located in the structured sponge breast phantom for the 300 mAs exposure.

RESULTS AND DISCUSSION

Geometric rods in cylinder

Reconstructed coronal slices for rods in the cylinder for each of the three exposure levels, along with profiles, are shown for rods in air (Figure 13), rods in oil (Figure 14), and rods in water (Figure 15). Calculated dose levels for the rods in the cylinder are 4.7, 2.4, and 0.8 mGy, respectively

For the rods in air as well as the rods in oil, resolution appears unaffected and artifact differences are unapparent for the three dose levels. Subjectively, the rods in oil appear to be noisier for the lower dose cases, as expected. Profiles for the above cases indicate high degree of similarity. For the low contrast case of rods in water, lower dose has a subjective affect on visibility of the rods due to increased noise and image artifact visibility. The profile also indicates a noisier image.

Table 2 summarizes SNR and contrast measurements for the rods in oil and rods in water. SNR is calculated as signal difference (between 4.4mm post and background) divided by noise in background ROI. Contrast is measured as signal difference divided by mean signal in background ROI. As expected for the rods in oil, SNR decreases as dose decreases (from 22 down to 15) while contrast remains fairly constant. For rods in water, SNR and contrast behave somewhat erratically. This is likely due to high sensitivity of results to image artifacts. Note the cupping artifact which is greatly exaggerated both in the slices and the profile (due to tight windowing in the slice pictures and tight attenuation coefficient axis in the profiles). Because our quasi-monochromatic beam is expected to result in minimal beam hardening, this cupping is likely due almost entirely to scatter.

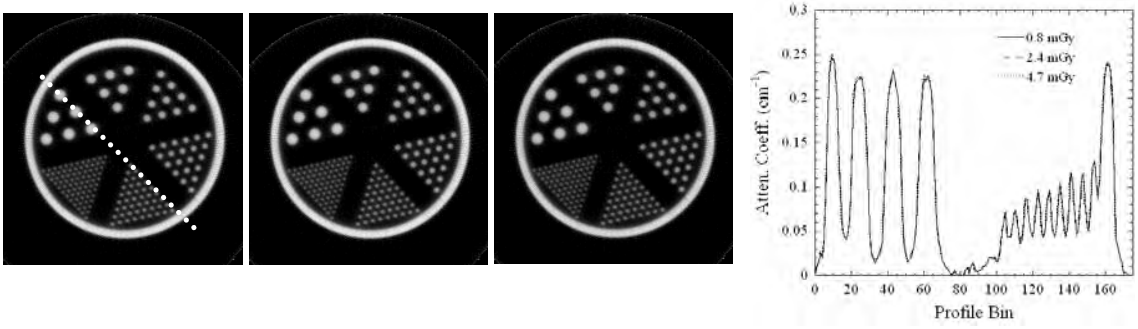

Figure 13. Reconstructed coronal slices through rods in air in the cylinder for (left) 4.7 mGy, (middle) 2.4 mGy, and (right) 0.8 mGy. Plot at far right contains profiles drawn through indicated line (at far left) for all three dose levels.

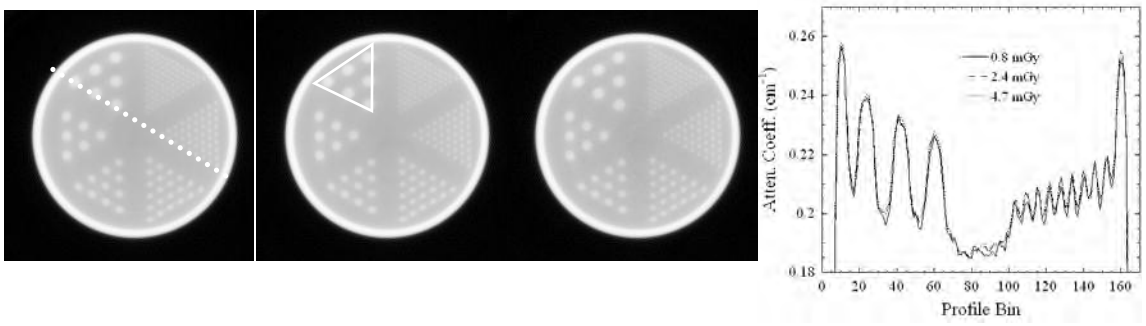

Figure 14. Reconstructed coronal slices through acrylic rods in oil in the cylinder for (left) 4.7 mGy, (middle) 2.4 mGy, and (right) 0.8 mGy. Plot at far right contains profiles drawn through indicated line (at far left) for all three dose levels. Triangle in center coronal slice indicates region where SNR and contrast were measured over the largest rods (see Table 2).

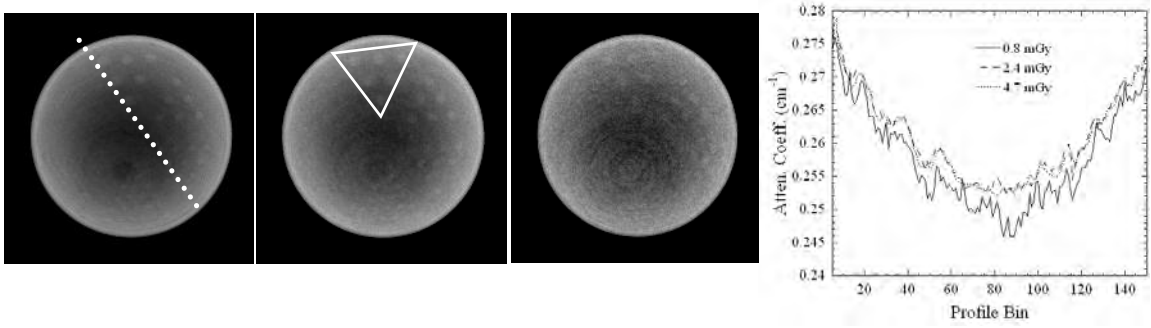

Figure 15. Reconstructed (and heavily windowed) coronal slices through acrylic rods in water in the cylinder for (left) 4.7 mGy, (middle) 2.4 mGy, and (right) 0.8 mGy. Plot at far right contains profiles drawn through indicated line (at far left) for all three dose levels. Triangle in center coronal slice indicates region where SNR and contrast were measured over the largest rods (see Table 2). Note that border of acrylic cylinder is also visible in the images, and that the shown profiles are a subsection of the entire cylinder width in order to highlight the valleys due to the rods.

Table 2. SNR and contrast for 4.7mm acrylic post in (left) oil and (right) water.

Dose (mGy)	Acrylic in Oil		Acrylic in Water	
	SNR	Contrast (%)	SNR	Contrast (%)
4.7	22	16.9	1.4	0.7
2.4	19	16.7	2.4	0.9
0.8	15	16.3	0.1	0.1

Geometric rods in breast phantoms

Reconstructed coronal slices for rods in the 975 mL breast phantom for each of the three exposure levels along with profiles are provided for rods in oil (Figure 16), and rods in water (Figure 17). Calculated dose levels for the rods in the 975 mL breast phantom are 3.7, 1.8, and 0.6 mGy. Reconstructed coronal slices for rods in water in the 750 mL breast phantom (Figure 18) are at calculated dose levels of 3.9, 1.9, and 0.6 mGy.

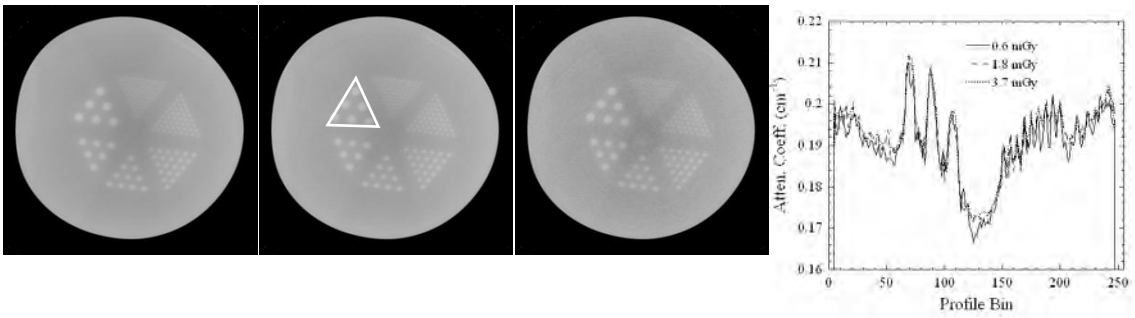

Figure 16. Reconstructed coronal slices through acrylic rods in oil in the 975 mL breast phantom for (left) 3.7 mGy, (middle) 1.8 mGy, and (right) 0.6 mGy. Plot at far right contains profiles drawn through indicated line (at far left) for all three dose levels. Triangle in center coronal slice indicates region where SNR and contrast were measured over the largest rods (see Table 3).

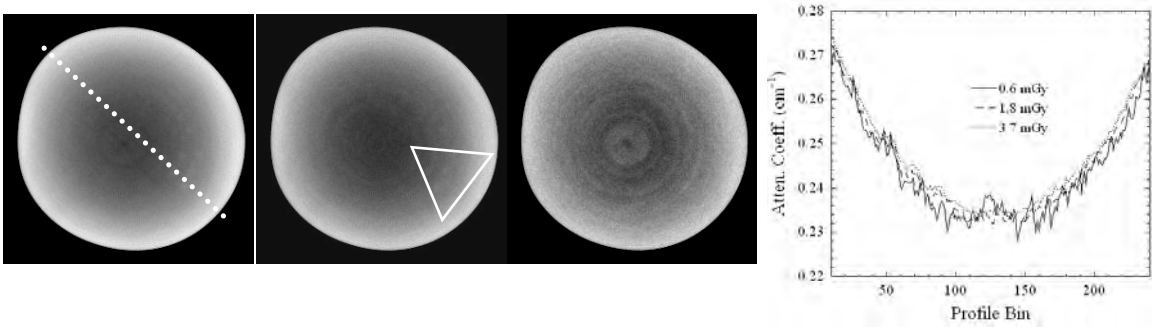

Figure 17. Reconstructed coronal slices through acrylic rods in water in the 975 mL breast phantom for (left) 3.7 mGy, (middle) 1.8 mGy, and (right) 0.6 mGy. Plot at far right contains profiles drawn through indicated line (at far left) for all three dose levels. Triangle in center coronal slice indicates region where SNR and contrast were measured over the largest rods (see Table 3).

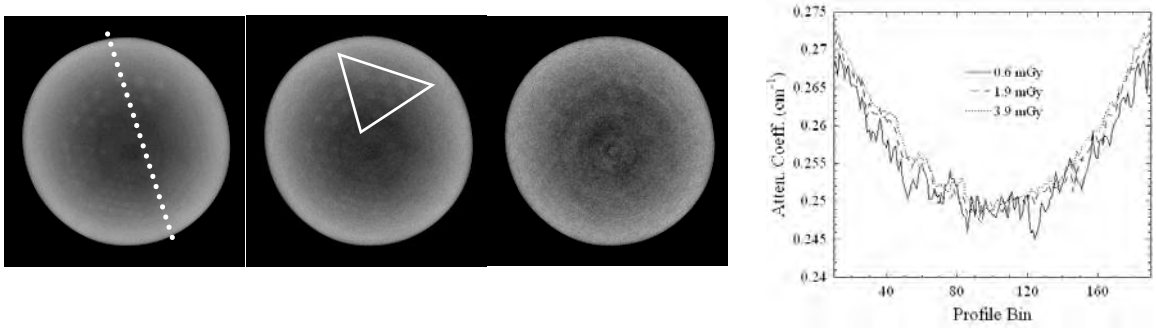

Figure 18. Reconstructed coronal slices through acrylic rods in water in the 750 mL breast phantom for (left) 3.9 mGy, (middle) 1.9 mGy, and (right) 0.6 mGy. Plot at far right contains profiles drawn through indicated line (at far left) for all three dose levels. Triangle in center coronal slice indicates region where SNR and contrast were measured over the largest rods (see Table 3).

For the rods in oil, the resolution again appears unaffected with the 1.5mm rods clearly discernible, and artifact differences are unapparent for the three dose levels. For the low contrast case of rods in water, lower dose again has a subjective affect on visibility of the rods due to increased noise and image artifact visibility. The profile also indicates a noisier image. Visibility of rods is reduced compared to the rods in water in cylinder case. This is likely due to increased scatter in the larger breast volume compared to the cylinder. (Note that the cupping artifact is most likely due to scatter alone, since the quasi-monochromatic beam virtually eliminates cupping due to beam hardening.) The rods in water in the smaller 750 mL breast phantom confirm this degradation due to scatter, in that rods appear to have higher visibility at each dose level compared to the 975 mL breast phantom case. This would be expected due to lower scatter in the smaller phantom volume. Table 3 summarizes SNR and contrast measurements for the rods in oil and rods in water. SNR decreases as dose decreases (from 9.7 down to 5.8) while contrast remains fairly constant for rods in oil. For rods in water, SNR decreases with dose, however, contrast behaves somewhat

erratically. This is again partly due to high sensitivity of the results to image artifacts including increased noise. As we have experienced with considerably more noisy nuclear emission mammotomography, post-reconstruction smoothing should reduce the decrease in SNR while holding contrast more constant.[24]

Table 3. SNR and contrast for acrylic rods in oil for the 975 mL breast and in water for the 975 and 750 mL breast phantoms.

Dose (mGy)	Acrylic in Oil 975 mL breast		Acrylic in Water 975 mL breast		Acrylic in Water 750mL breast	
	SNR	Contrast (%)	SNR	Contrast (%)	SNR	Contrast (%)
3.7	9.7	10.0	6.7	2.2	7.8	2.4
1.8	8.3	10.2	1.9	1.2	5.0	1.9
0.6	5.8	10.2	0.4	0.4	4.2	2.7

Oil lesions in water filled, structured breast phantom

Reconstructed coronal slices for oil-filled lesions in a water-sponge background in the 975 mL breast phantom for each of the three exposure levels, along with profiles for the 500 and 60 uL lesion (Figure 19), as well as the 140 uL lesion are provided (Figure 20). Reconstructed sagittal slices are also provided for the 60 uL lesion (Figure 21). Calculated dose levels are 3.7, 1.8, and 0.6 mGy.

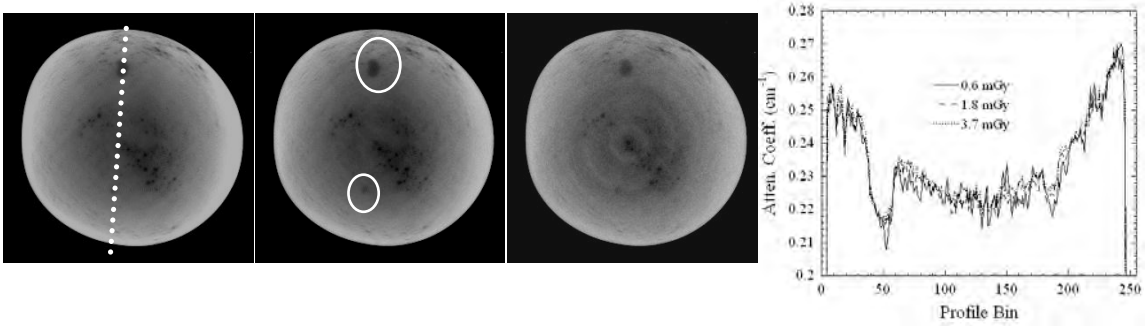

Figure 19. Reconstructed coronal slices through the 500 and 60 uL oil-filled lesions (encircled in middle image) embedded in the sponge in the 975 mL water-filled breast phantom for (left) 3.7 mGy, (middle) 1.8 mGy, and (right) 0.6 mGy. Plot at far right contains profiles drawn through indicated line (at far left) for all three dose levels. Circles in center coronal slice indicate regions where SNR and contrast were measured over the lesions (see Table 4).

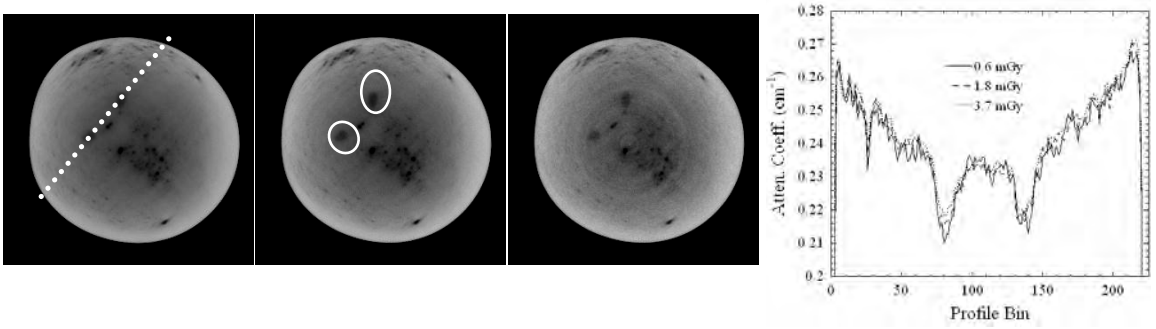

Figure 20. Reconstructed coronal slices through two 140 uL oil-filled lesions (encircled in middle image) embedded in the sponge in the 975 mL water-filled breast phantom for (left) 3.7 mGy, (middle) 1.8 mGy, and (right) 0.6 mGy. Plot at far right contains profiles drawn through indicated line (at far left) for all three dose levels. Circles in center coronal slice indicate regions where SNR and contrast were measured over the lesions (see Table 4).

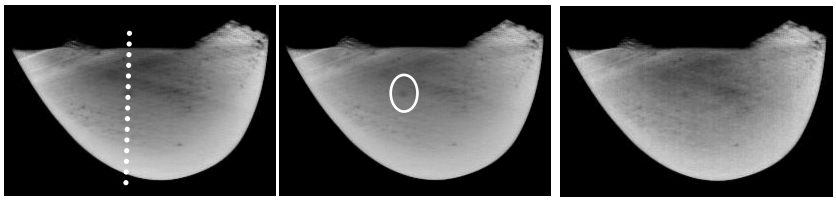

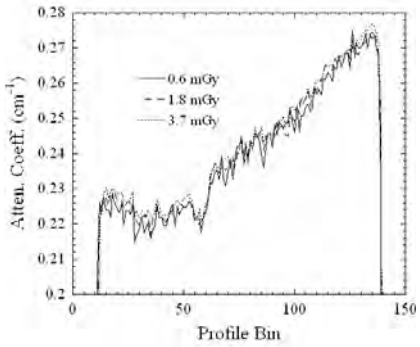

Figure 21. Reconstructed sagittal slices through the 60 uL oil-filled lesion (encircled in middle image) embedded in the sponge in the 975 mL water-filled breast phantom for (left) 3.7 mGy, (middle) 1.8 mGy, and (right) 0.6 mGy. Plot at far right contains profiles drawn through indicated line (at far left) for all three dose levels. Circle in center coronal slice indicate regions where SNR and contrast were measured over the lesion (see Table 4).

The 500 and 140 uL lesions are easily detectable for all dose levels, although noise increases with reduced dose. The 60 uL lesion was more difficult to find for all dose levels, however, its appearance is similar for all three cases. The 30 uL lesion was not found for any dose level, most likely as it is difficult to discern from the spongy structural background (note that the 30 uL lesion size (Table 1) is comparable to the hole sizes throughout the sponge). Table 4 summarizes the SNR and contrast measurements for the 500, 140, and 60 uL oil-filled lesions. For all lesion sizes, SNR decreases as dose decreases. For the 500 and 140 uL lesions, contrast remains fairly constant. However, for the 60 uL lesion, contrast behaves somewhat erratically potentially due to the shape of the scatter-uncorrected background. Toroidal background regions of interest may perhaps yield a more reasonable estimate of the mean background values rather than the simple circular regions used to evaluate the mean pixel values about the lesion regions of interest. Depending on the background location chosen with our approach here, the background value could be dramatically affected (see profile in Figure 13 which changes in magnitude by ~20% from the chest wall towards the nipple).

Table 4. SNR and contrast for 500, 140, amd 60 uL lesion in coronal view as well as 60 uL lesion in sagittal view.

Dose (mGy)	500 uL lesion Coronal		140 uL lesion Coronal		60 uL lesion Coronal		60 uL lesion Sagittal	
	SNR	Contrast (%)	SNR	Contrast (%)	SNR	Contrast (%)	SNR	Contrast (%)
3.7	6.7	6.2	7.3	5.6	3.3	2.5	5.1	7.9
1.8	4.1	6.2	6.3	5.9	3.2	2.7	3.6	6.5
0.6	4.2	6.7	4.1	6.6	2.3	3.4	2.2	2.4

Cadaver breast

Reconstructed coronal and sagittal slices for the cadaver breast in 975 mL breast cup for each of the three exposure levels, along with coronal profiles, are provided (Figure 22). Calculated dose levels are 3.7, 1.8, and 0.6 mGy. The cadaver breast was obtained from a 48 year old woman, and in the sagittal views, a clip from a previous biopsy (bright dot in upper left) can be seen along with muscle, glandular and skin tissues.

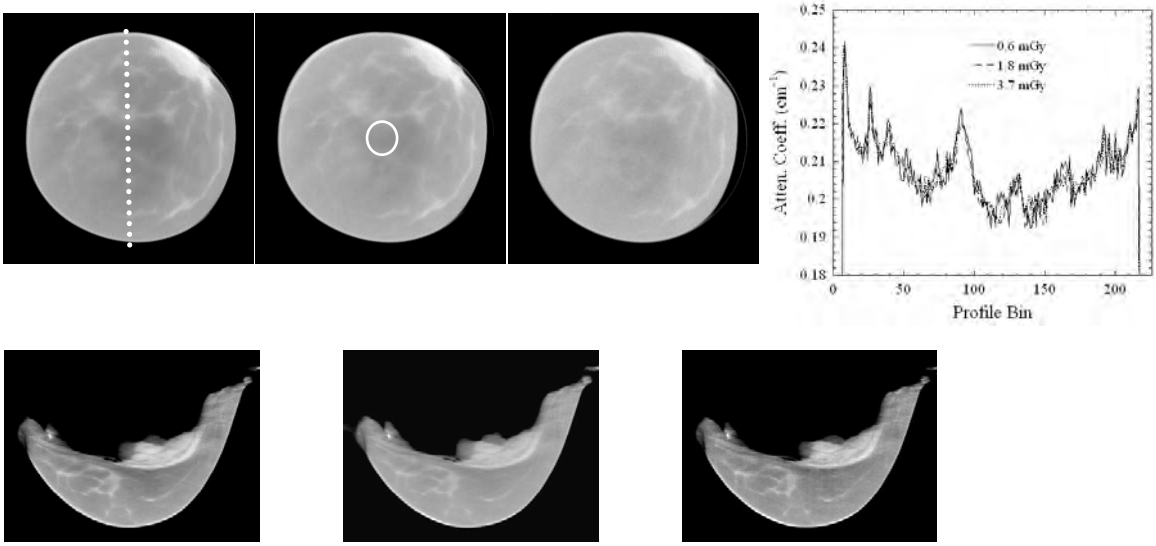

Figure 22. Reconstructed (top row) coronal and (bottom row) sagittal slices through cadaver breast held in the 975 mL breast cup for (left) 3.7 mGy, (middle) 1.8 mGy, and (right) 0.6 mGy. Plot at top row, far right contains profiles drawn through indicated line (at top, far left) for all three dose levels. Circle in center coronal slice indicates region where SNR and contrast were measured.

Breast SNRs (signal-to-noise ratio, not a signal difference ratio) of 103, 93, and 75 were observed for a uniform region near the center of the breast for for the various doses. Subjectively, the breast tissue images appear similar between dose levels though, once again, higher noise and slightly increased image artifacts are apparent for the lower doses. Note that this cadaver breast sample has been thawed and refrozen several times over a few months, and the degradation due to compromised adipose tissue boundaries as well as other physical breast features are becoming apparent.

CONCLUSIONS

These early studies indicate that it may well be possible to perform CmT studies at up to 10X lower dose than that of dual view mammography. The target spatial resolution is unclear, however, though here we have clearly made out 1.5mm sized medium contrast objects (20% contrast, geometric rods), and 4mm sized lower contrast objects (6% contrast, 60 uL lesions) simulating soft tissue lesions in a highly glandular breast. In the case of very low contrast, currently such extreme windowing is required that image artifacts become apparent. Improvements in uniformity artifact correction and implementation of scatter correction should allow us to image sub-4mm, very low contrast lesions at 10X lower dose than for dual view mammography.

One next planned step in anticipation of patient studies includes contrast detail studies, and will require construction of a custom phantom utilizing a finer range of contrasts. Specific contrast detail studies between our CmT approach and standard x-ray mammography are also warranted, as the soft tissue detectability of mammography is greatly compromised at the outset by not having a monochromatic x-ray beam and having only line integral projection images. In addition to overcoming both those deficits with our approach of computed mammotomography, our narrow spectral beam approach lends itself to the possibility of quantitation of absolute attenuation coefficients, hence the ability to identify and characterize tissue *in vivo*, even with low overall dose to a patient's breast. Importantly, we have shown that this may be achievable with a high degree of patient comfort since we are optimizing the approach for uncompressed breast imaging.

ACKNOWLEDGEMENTS

This work is supported by NIH Grant R01-CA96821 and DAMD Grant W81XWH-05-1-0280. The authors thank Dr. James Bowsher for use of the OSTR reconstruction code, and Dr. John Boone for the dose tables used in this work.

REFERENCES

[1] J.M. Boone, T.R. Nelson, K.K. Lindfors et al., "Dedicated Breast CT: Radiation Dose and Image Quality Evaluation," *Radiology* **221**, 657-667 (2001).
[2] B. Chen and R. Ning, "Cone-beam volume CT mammographic imaging: feasibility study," *Med. Phys.* **29**, 755-770 (2002).
[3] A.A. Vedula and S.J. Glick, "Computer simulations of CT mammography using a flat panel imager," *Proc. SPIE* **5030**, 349-360 (2003).
[4] M.P. Tornai, J.E. Bowsher, C.N. Archer et al., "A Compact Dedicated Device for Dual Modality Radionuclide Imaging of the Breast with an Application Specific Emission and Transmission Tomograph (ASETT)," *Radiology* **221P**, 555 (2001).
[5] M.P. Tornai, J.E. Bowsher, C.N. Archer et al., "A 3D Gantry Single Photon Emission Tomograph with Hemispherical Coverage for Dedicated Breast Imaging," *Nucl. Instr. Meth. Phys. Res. A* **497**, 157-167 (2003).
[6] M.L. Bradshaw, R.L. McKinley, E. Samei et al., "Initial x-ray design considerations for application specific emission and transmission tomography (ASETT) of the breast," *J. Nucl. Med.* **44** (**5**), 287P (2003).
[7] M.P. Tornai, J.E. Bowsher, C.N. Archer et al., "Feasibility of Application Specific Emission and Transmission Tomography (ASETT) of the breast," *J. Nucl. Med.* **43** (5), 12 (2002).
[8] R.L. McKinley, E. Samei, C.N. Brzymialkiewicz et al., "Measurements of an Optimized Beam for X-ray Computed Mammotomography," *Proc. SPIE: Phys. of Med. Imag.* **5368**, 311-319 (2004).
[9] R.L. McKinley, M.P. Tornai, C.N. Archer et al., "Quasi-monochromatic beam measurements for dedicated cone-beam mammotomography of an uncompressed breast," presented at the *7th International Workshop on Digital Mammography*, Durham, NC, 2004 (unpublished).
[10] R.L. McKinley, M.P. Tornai, E. Samei et al., "Simulation Study of a Quasi-Monochromatic Beam for x-ray Computed Mammotomography," *Med. Phys.* **31** (4), 800-813 (2004).
[11] R.L. McKinley, M.P. Tornai, E. Samei et al., "Optimizing Beam Quality for x-ray Computed Mammotomography (CmT)," *Proc. SPIE* **5030**, 575-584 (2003).
[12] R.L. McKinley, M.P. Tornai, E. Samei et al., "Initial study of quasi-monochromatic beam performance for x-ray computed mammotomography," *IEEE MIC* **4**, 2999-3003 (2003).
[13] M.P. Tornai, C.N. Archer, J.E. Bowsher et al., "Transmission imaging with a compact gamma camera: initial results for mammotomography," *IEEE Nucl. Sci. Symp. and Med. Imag. Conf. Rec.* **3**, 1597-1601 (2002).
[14] M.P. Tornai, R.L. McKinley, M.L. Bradshaw et al., "Effects of uncompressed breast composition and thickness on image quality using a quasi-monochromatic beam for computed mammotomography," presented at the *7th Int. Workshop on Digital Mammography*, Durham, NC, 2004 (unpublished).

[15] R.L. McKinley, M.P. Tornai, C.N. Brzymialkiewicz et al., "Analysis of a novel offset cone-beam computed mammotomography imaging system for attenuation correction of SPECT in a proposed dual modality dedicated breast mammotomography system," *Presented at the 2004 Workshop on the Nuclear Radiology of the Breast, Rome, Italy and submitted to Physics Medica* **(In Press)** (2004).
[16] R. Ning, B. Chen, D. Conover et al., "Flat panel detector-based cone beam volume CT mammography imaging: preliminary phantom study," *Proc. SPIE* **4320**, 601-610 (2001).
[17] J.M. Boone, A.L.C. Kwan, J.A. Seibert et al., "Technique factors and their relationship to radiation dose in pendant geometry breast CT," *Med. Phys.* **32** (12), 3767-3776 (2005).
[18] R.L. McKinley, M.P. Tornai, E. Samei et al., "Development of an optimal x-ray beam for dual-mode emission and transmission mammotomography," *Nucl. Instr. Meth. Phys. Res. A* **527**, 102-109 (2003).
[19] R.L. McKinley, M.P. Tornai, E. Samei et al., "Initial study of quasi-monochromatic beam performance for x-ray computed mammotomography," *IEEE Trans. Nucl. Sci.* **(In Press)** (2005).
[20] R.L. McKinley, C.N. Brzymialkiewicz, P. Madhav et al., "Investigation of cone-beam acquisitions implemented using a novel dedicated mammotomography system with unique arbitrary orbit capability," *Proc. SPIE: Phys. of Med. Imag.* **5745**, 609-617 (2005).